FABRICATION AND NANOROUGHNESS CHARACTERIZATION OF SPECIFIC NANOSTRUCTURES AND NANODEVICE

by

ZHUANGDE JIANG

A thesis submitted to
The University of Birmingham
for the degree of
DOCTOR OF PHILOSOPHY

Mechanical Engineering Department
School of Engineering
The University of Birmingham
August 2011

UNIVERSITY OF
BIRMINGHAM

University of Birmingham Research Archive

e-theses repository

This unpublished thesis/dissertation is copyright of the author and/or third parties. The intellectual property rights of the author or third parties in respect of this work are as defined by The Copyright Designs and Patents Act 1988 or as modified by any successor legislation.

Any use made of information contained in this thesis/dissertation must be in accordance with that legislation and must be properly acknowledged. Further distribution or reproduction in any format is prohibited without the permission of the copyright holder.

ABSTRACT

Nanoroughness is becoming a very important specification for many nanostructures and nanodevices, and its metrology impacts not only the nanodevice properties of interest, but also its material selection and process development. This Ph.D. thesis presents an investigation into fabrication and nanoroughness characterization of nanoscale specimens and MIS (metal-insulator-semiconductor) capacitors with HfO_2 as a high k dielectric.

Self-affine curves and Gaussian, non-Gaussian, self-affine as well as complicated rough surfaces were characterized and simulated. The effects of characteristic parameters on the CD (critical dimension) variation and the properties of these rough surfaces were visualized. Compared with experimental investigations, these simulations are flexible, low cost and highly efficient. Relevant conclusions were frequently employed in subsequent investigations.

A proposal regarding the thicknesses of the deposited films represented by nominal linewidths and pitch was put forward. The MBE (Molecular Beam Epitaxy) process was introduced and $AlGaAs$ and $GaAs$ were selected to fabricate nanolinewidth and nanopitch specimens on $GaAs$ substrate with nominal linewidths of 2nm, 4nm, 6nm and 8nm, and a nominal pitch of 5nm. HRTEM (High Resolution Transmission Electron Microscopy) image-based characterization of LER/LWR (Line Edge Roughness/Line Width Roughness) in real space and frequency domains

demonstrated that the MBE-based process was capable of fabricating the desired nanolinewidth and nanopitch specimens and could be regulated accordingly.

MIS capacitors with HfO_2 film as high k dielectric were fabricated, and SEM (Scanning Electron Microscope) image-based nanoroughness characterization, along with measurement of the MIS capacitor electrical properties were performed. It was concluded that the annealing temperature of the deposited HfO_2 film was an important process parameter and 700℃ was an optimal temperature to improve the properties of the MIS capacitor. Also, by quantitative characterization of the relevant nanoroughness, the fabrication process can be further regulated.

The uncertainty propagation model of SEM-based nanoroughness measurement was presented according to specific requirements of the relevant standards, ISO GPS (Geometric Product Specifications and Verification) and GUM (Guide to the Expression of Uncertainty in Measurement), and the method for implementating uncertainties was evaluated. The case study demonstrated that the total standard uncertainty of the nanoroughness measurement was 0.13nm, while its expanded uncertainty with the coverage factor k as 3 was 0.39nm. They are indispensable parts of LER/LWR measurement results.

ACKNOWLEDGEMENTS

My heartiest gratitude goes to my supervisors Prof. P.D. Prewett and Prof. K.C. Jiang who provided me with their utmost guidance throughout the duration of my Ph.D research project. Especially I would like to thank Prof. K.C. Jiang for his detailed advice on research reviews, publication of journal and conference papers and thesis writing. His kind attention to my research project, his valuable comments and suggestions on the thesis, and his arrangements for my life in the University of Birmingham helped me significantly in the progress of my research.

My special thanks go to Prof. David Hukins for his time and work in reading the drafts of my thesis. He gave me a lot of constructive feedback, and I was always grateful when I got his valuable corrections and comments. His warmhearted help is highly appreciated.

Last but not least, I would like to thank my family, especially my wife, for their supporting me not only in this research project, but also in all aspects of my life.

TABLE OF CONTENTS

Acknowledgements
Table of Contents
List of Figures
List of Tables
List of Publications

1. Introduction

1.1. Introduction to the Research Project 1
1.2. Aims and Objectives 3
1.3. Thesis Structure 5
1.4. Summary 8

2. A Review on Fabrication and Nanoroughness Characterization of Specific Nanostructures and Nanodevices

2.1. Introduction 9
2.2. Challenges in Nanoroughness Metrology 10
2.3. Fabrication of Nanolinewidth and Nanopitch Specimens 12
2.4. Modeling and Visualization of Nanoroughness Metrology 17
2.5. Effects of Nanoroughness Metrology on the Properties of Nanostructures/ Nanodevices 23
2.5.1. Capacitance of Thin Insulating Films 24
2.5.2. Electrical Properties of Sub-50nm MOS Transistors 28
2.5.3. Light Scattering in Optoelectronic Device 29
2.5.4. Adsorption of Proteins on Surfaces 30
2.5.5. Wettability of Surfaces 31
2.6. Uncertainty Evaluation of SEM-based Metrology 33
2.6.1. Implementation Uncertainty of SEM-based Metrology 34
2.6.2. Method Uncertainty of SEM-based Metrology 37
2.7. Summary 38

3. Characterization and Simulation of Self-affine Curves and 3-D Rough Surfaces

3.1. Introduction 40
3.2. Characterization and Simulation of Random Rough Curves 41
3.2.1. Fractal Model of a Random Rough Surface 41
3.2.2. Descriptors of 2-D Random Rough Curves 43
3.2.2.1. Root Mean Square σ 43
3.2.2.2. Height-height Correlation Function (HHCF) 44
3.2.2.3. PSD 46
3.2.3. Simulation of Self-affine Fractal Curves 47
3.2.3.1. Simulation of Self-affine Curves 47
3.2.3.2. Simulation of the Effect of Parameters on *CD* Variation 49
3.3. Characterization and Simulation of 3-D Rough Surfaces 51
3.3.1. Characterization of 3-D Rough Surfaces 51
3.3.1.1. Root Mean Square Sq 52
3.3.1.2. Skewness Ssk 52
3.3.1.3. Kurtosis Sku 52
3.3.1.4. Autocovariance Function and Autocorrelation Function 53
3.3.1.5. PSD 53
3.3.1.6. HHCF 54
3.3.2. Simulation of 3-D Rough Surfaces 54
3.3.2.1. Simulation of a Gaussian Random Rough Surface 54
3.3.2.2. Complicated Rough Surface 60
3.3.2.3. Simulation of Non-Gaussian Random Rough Surface 61
3.3.2.4. Simulation of a Self-affine Rough Surface 66
3.4. Summary 68

4. Fabrication and Nanoroughness Characterization of Nanolinewidth and Nanopitch Specimens

4.1. Introduction 70
4.2. A Brief Introduction to Fabrication of Nanolinewidth and Nanopitch Specimens 71
4.3. MBE-based Fabrication of Nanolinewidth and Nanopitch Specimens 72
4.3.1. Background on the MBE process 73
4.3.2. MBE-based Design of Nanolinewidth and Nanopitch 75

Specimens
4.3.3. Material Selection for MBE-based Fabrication of Nanolinewidth and Nanopitch Specimens 76
4.3.4. MBE System and Fabrication of Nanolinewidth and Nanopitch Specimens 77
4.4. HRTEM-based Measurement of Nanolinewidth and Nanopitch Specimens 79
4.4.1. Samples Thinned and Processed Before HRTEM Measurement 79
4.4.2. HRTEM Images of Fabricated Nanolinewidth and Nanopitch Specimens 81
4.5. Nanoroughness Metrology and Its effect on the Precision of Nanolinewidth and Nanopitch Specimens 82
4.5.1. Main Steps for HRTEM Images Preprocessing 82
4.5.2. Filtration of HRTEM Images 83
4.5.2.1. Introduction to Image Noises 83
4.5.2.2. Frequently-used Filters for Image Noises Smoothing 85
4.5.2.3. Selection of the Filter for the Filtration of HRTEM Images 87
4.5.3. Extraction of Line Edge Profiles from HRTEM Images 88
4.5.3.1. Traditional Line Edge Detect Operators 88
4.5.3.2. Wavelet Transform-based Multi-scale Line Edge Detection 90
4.5.3.3. Lipschitz Power Discrimination of a Noise Singular Point 92
4.5.3.4. Wavelet Transform-based Multiscale Line Edge Detection 93
4.5.4. Fitting of the Detected Line Edges 94
4.5.5. Characterization of Line Edge Profiles 95
4.5.5.1. RMS σ 96
4.5.5.2. Height-height Correlation Function(HHCF) 97
4.5.5.3. Power Spectral Density(PSD) 98
4.6. Nanoroughness-based Process Regulation for Nanolinewidth and Nanopitch Specimens 99
4.7. Summary 101

5. Fabrication and Nanoroughness Characterization of a Capacitor with HfO_2 as a High k Dielectric

5.1. Introduction 102

5.2. Design of the MIS Capacitor With HfO_2 as High *k* Dielectric 103
5.2.1. Background on a MIS capacitor 103
5.2.2. Selection of HfO_2 as High *k* Dielectric for the MIS capacitor 104
5.2.3. Design of the MIS Capacitor with HfO_2 as high *k* dielectric 106
5.3. Fabrication of the MIS Capacitor with HfO_2 as the High *k* Dielectric 106
5.3.1. Deposition on a Si Substrate 107
5.3.2. Annealing Process of the Deposited HfO_2 108
5.3.3. Fabricating the MIS Capacitor With HfO_2 as the Dielectric 108
5.4. Measurement and Characterization of the MIS Capacitor 110
5.4.1. The Thickness Measurement of the HfO_2 High *k* 110
5.4.2. X-ray Diffraction (XRD) Analysis of the Annealed HfO_2 High *k* Dielectric 111
5.4.3. The Leakage Current of the MIS Capacitor 112
5.4.4. The C-V Property of the MIS Capacitor 114
5.5. Nanoroughness Metrology and Characterization of the MIS Capacitor 115
5.5.1. Surface Roughness of the Deposited HfO_2 Dielectric Films 116
5.5.2. Interface Roughness at the Mo/HfO_2 and HfO_2/Si Interfaces 117
5.5.2.1. Filtering of the SEM Images 118
5.5.2.2. Extraction of the Line Edge Profiles 118
5.5.2.3. Fitting of the Datum Lines 118
5.5.2.4. Characterization of Interface Roughness 121
5.6. Relationships Between the Performance of the MIS Capacitor, the Surface/Interface Roughness and the Parameters of the Fabrication Process 129
5.7. Summary 132

6. Uncertainty Evaluation of Nanoroughness Measurements

6.1. Introduction 133
6.2. Theoretical Fundamentals of Measurement Uncertainty 134
6.2.1. Definition of Measurement Uncertainty 134
6.2.2. Evaluation of Standard Uncertainty 135
6.2.2.1. Type A-Evaluation of Standard Uncertainty 135
6.2.2.2. Type B-Evaluation of Standard Uncertainty 136
6.2.3. Combination of Measurement Uncertainties 138
6.2.3.1. Combined Standard Uncertainty 138
6.2.3.2. Expanded Uncertainty 139
6.3. Uncertainty Propagation Model of SEM-based Nanoroughness Measurement 139
6.3.1. SEM-based Nanoroughness Measurement Process 140
6.3.2. Preprocessing of SEM Aerial Image 140
6.3.2.1. Noise-smoothing 140
6.3.2.2. Extraction Operation 141

6.3.2.3. Fit Operation 142
6.3.3. Uncertainty Propagation Model of Nanoroughness Measurement 143
6.4. Evaluation of Uncertainties Produced by SEM Instrument 144
6.4.1. Identification of SEM-based Uncertainty Sources 144
6.4.2. Analysis of SEM-based Uncertainty Sources 145
6.4.2.1. Uncertainty Produced by SEM Resolution 145
6.4.2.2. Uncertainty Introduced by SEM Enlarged Image Measurement 145
6.4.2.3. Uncertainty arising from Stability of SEM Magnification 146
6.4.2.4. Uncertainty arising from Aberration of the SEM image 146
6.4.2.5. Uncertainty caused by Secondary Electron Formation 147
6.4.2.6. Uncertainty caused by the Variation of SEM Working Distance 147
6.4.2.7. Uncertainty caused by the Calibrator 147
6.4.2.8. Uncertainty caused by Sample Surface Tilt 147
6.4.2.9. Uncertainty caused by Sample Deformation 148
6.4.3. Evaluation of SEM-based Uncertainties 148
6.4.3.1. Evaluation of Δh 148
6.4.3.2. Evaluation of ΔA 149
6.4.3.3. Evaluation of ΔB 149
6.4.3.4. Calculation for the value of A 149
6.4.3.5. Calculation for the value of B 150
6.4.3.6. Combined Standard Uncertainty of the Measurement Result 150
6.5 Uncertainty Estimation for SEM Image Processing 151
6.5.1. Estimation of the Uncertainty caused by Sampling Length 151
6.5.2. Estimation of the Uncertainty caused by SEM Image Noise 153
6.5.3. Estimation of the Uncertainty Produced by a Median Line of Least-Squares Fit 155
6.6. Case Study 157
6.6.1. Fabrication of a Nanoscale Grating Structure 157
6.6.2. Evaluation of Uncertainties Produced by SEM 158
6.6.2.1. Measurement Condition 158
6.6.2.2. Evaluation of Uncertainty Produced by SEM 158
6.6.3. Evaluation of Uncertainty Caused by SEM Image Preprocessing 159
6.6.3.1. Measurement Uncertainty u_w Produced by a Sampling Length 159
6.6.3.2. Measurement Uncertainty u_w Produced by SEM Image Noise 160

6.6.3.3. Measurement Uncertainty u_w Produced by the Least-Squares Fitted Median Line 160
6.6.4. Evaluation of Total Uncertainty for LER Measurement 161
6.7. Summary 161

7. Summary and Conclusions

7.1. Summary 163
7.2. Conclusions 167
7.3. Future Work 169

List of References 172

LIST OF FIGURES

Figure 1.1	Nanoroughness study framework	2
Figure 1.2	Study flow of nanoroughness metrology	4
Figure 2.1	(a) Schematic diagram of LER, LWR and SWR. (b) Definitions of LER and LWR	10
Figure 2.2	Schematic diagram of frequently-used specimens	12
Figure 2.3	Schematic diagram of laser-focused atomic deposition process	13
Figure 2.4	AFM image of the fabricated specimen	13
Figure 2.5	AFM image of the fabricated grating lines. (a) Oxide lines produced on Si (100) substrate. (b) Grating line patterns scratched on Al substrate	14
Figure 2.6	SEM images of the respective trench and line. (a) Trench width 50nm. (b) Line width 25nm	15
Figure 2.7	SEM diagrams of THE fabricated nanoscale specimen. (a) Linewidths of the specimen. (b) Si_3N_4 layers were etched off by RIE process for 100 seconds	16
Figure 2.8	Diagram of LPD process for patterns with linewidth less than 100nm	17
Figure 2.9	The generated surface with given spectral density and sampling interval 0.01μm. (a) The 3-D rough surface. (b) Height distribution of the generated surface	19
Figure 2.10	The generated surface with given spectral density and sampling interval 0.01μm. (a) Height distribution. (b) Spectral density	20
Figure 2.11	Surfaces simulated with M–W equation for different fractal dimension D: (a) D =1.3, (b) D=1.5 and (c) D=1.8	20
Figure 2.12	Network topology with process parameters as input layer and roughness parameters as output layer	21
Figure 2.13	Relationship between resistance, capacitance, 1/f noise spectral density and fractal dimension D	21
Figure 2.14	The simulation of a complicated rough surface. (a) A cosine surface. (b) A Gaussian surface. (c) A complicated rough surface. (d) The ACF comparison of the three rough surfaces	22
Figure 2.15	Simulation of LER effect of Cu interconnect on its performance. (a) Discrete random sequences as roughness amplitudes. (b) LWR effects on resistance R and capacitance C. (c) Other approximations of the measured auto-covariance function	25
Figure 2.16	Estimated impact of different LWRs on Cu interconnects for future technology nodes	26
Figure 2.17	Interface roughness effect on the performance of the MIS capacitor with HfO_2 as high k dielectric. (a) C-V curves. (b) Electric fields vs leakage	27

currents
Figure 2.18 Nanoroughness of pure and composite thin films of the high k dielectrics 28
Figure 2.19 Three modes of LER influence on sub-50nm transistor performance. (a) The degradation of one MOSFET device. (b) The variation of several MOSFET devices along the gate length direction. (c) The variation of several MOSFET devices along the gate width direction 29
Figure 2.20 Nanoroughness effect on the light scattering in optoelectronic devices. (a) Light emission intensity versus the oxide roughness. (b) Relationship between the oxide roughness and light emission efficiency 30
Figure 2.21 Evolution of the contact diameter on nanorough surfaces with time scales. (a) Linear time scale. (b) Logarithmic time scale 30
Figure 2.22 Relationship between the number of cells released from the samples and surface roughness. (a) Roughness described by Ra (squares) and Rq (circles). (b) Roughness described by r (triangles) and D_f (diamonds). 32
Figure 2.23 Relationships between various uncertainties of a geometric product 33
Figure 2.24 Threshold-based determination of the linewidth 34
Figure 2.25 The Edge assignment errors caused by the threshold edge criterion 34
Figure 2.26 Schematic of the model-based library (a), and the comparison of the width bias obtained by four methods(b) 36
Figure 2.27 (a) Simulation of the secondary electron diffusion at a silicon line. (b) the corresponding secondary electron image 37
Figure 2.28 The topography of the structure and its corresponding model profile 37
Figure 3.1 Diagram of the self similarity of a self-affine profile 41
Figure 3.2 HHCF curve of a line edge profile 45
Figure 3.3 PSD curve of a line edge profile 45
Figure 3.4 Simulation of a self-affine curve 48
Figure 3.5 Simulation of self-affine curves with different σ, ξ and α values 48
Figure 3.6 Histogram of the *CD* variations with *CD* values of (a) 10nm, (b) 50nm and (c) 500nm 49
Figure 3.7 Effect of RMS σ on *CD* variation 50
Figure 3.8 Effect of correlation length ξ on *CD* variation 50
Figure 3.9 Effect of roughness exponent α on *CD* variation 51
Figure 3.10 The simulated 3-D profiles of a rough isotropic surfaces with exponential ACFs 57
Figure 3.11 The simulated 3-D profiles of anisotropic surface with an exponential ACF and different ν values 57
Figure 3.12 Comparison of exponential ACFs of isotropic and anisotropic surfaces 58
Figure 3.13 The simulated 3-D profiles of isotropic surfaces with cosine-exponential ACF 59
Figure 3.14 Contour maps of exponential ACFs of a rough surface 59
Figure 3.15 Contour maps of cosine-exponential ACFs of a rough surface 60
Figure 3.16 Simulated complex rough surface and the contour map of the combined ACFs 61

Figure 3.17 Simulation of non-Gaussian rough surfaces with different minus skewness 63
Figure 3.18 Simulation of rough surfaces with different positive skewnesses 64
Figure 3.19 Simulation of rough surfaces with different kurtosises 65
Figure 3.20 Simulation of rough surfaces with different correlation lengths 66
Figure 3.21 Simulations of self-affine rough surfaces 67
Figure 4.1 Schematic diagram of MBE process 73
Figure 4.2 Diagrams of nanoscale specimens to be fabricated with MBE process and their materials selection 75
Figure 4.3 Diagram of the MBE system used for fabrications of nanolinewidth and nanopitch specimens 78
Figure 4.4 Schematic diagram of MBE system with ultrahigh vacuum chambers 78
Figure 4.5 Steps of thinning process of HRTEM samples 80
Figure 4.6 HRTEM images of fabricated specimens. (a) nanolinewidth. (b) nanopitch 81
Figure 4.7 Tilt correction of HRTEM images of fabricated nanoscale specimens: (a) nanolinewidth specimen and (b) nanopitch specimen 82
Figure 4.8 Main steps of the algorithm for detecting the line edges from a HRTEM image 83
Figure 4.9 Categories of line edges and corresponding line edge detection process 89
Figure 4.10 Diagram of the equivalent wavelet transform of $WT_{\xi}f(x,a)$ 92
Figure 4.11 Diagram of the equivalent wavelet transform of $WT_{\eta}f(x,a)$ 92
Figure 4.12 Steps of the wavelet transform-based multiscale line edge detection 94
Figure 4.13 Wavelet transform-based multi-scale line edge detection for the nanolinewidth and nanopitch specimens 95
Figure 4.14 The HHCF of a grating line whose nominal linewidth is 4nm shown in Figure 4.13(b) 97
Figure 4.15 The HHCF of the left edge of the first grating line shown in Figure 4.13(d) 97
Figure 4.16 PSD of the left line edge whose nominal linewidth is 4nm as shown in Figure 4.13(b) 98
Figure 4.17 PSD of the left line edge of the first grating line as shown in Figure 4.13(d) 98
Figure 5.1 Diagram of the MIS capacitor with HfO_2 as high k dielectric 106
Figure 5.2 UHV multifunction magnetron sputtering system used to deposit the HfO_2 dielectric 108
Figure 5.3 Fabrication flow of the electrodes of the MIS capacitor 109
Figure 5.4 The fabricated MIS capacitors 110
Figure 5.5 Δ and ψ curves of HfO_2 dielectric film 110
Figure 5.6 XRD patterns of the deposited HfO_2 films 112
Figure 5.7 Comparison of leakage current densities of HfO_2 layers 113
Figure 5.8 Comparison of C-V properties of HfO_2 films which did and did not undergo the annealing process 115
Figure 5.9 AFM images of HfO_2 films which were not annealed and annealed at 117

	different temperatures	
Figure 5.10	SEM aerial images of the Mo/HfO_2 and HfO_2/Si interfaces	119
Figure 5.11	The SEM images filtered with a Gaussian filter	120
Figure 5.12	Extracted HfO_2 line edge profiles	122
Figure 5.13	Extracted Mo line edge profiles	123
Figure 5.14	HHCF curves of line edges profiles (dielectric HfO_2 films)	124
Figure 5.15	HHCF curves of line edges profiles (Mo films)	125
Figure 5.16	PSD curves of line edges profiles (dielectric HfO_2 films)	126
Figure 5.17	PSD curves of line edges profiles (Mo films)	127
Figure 6.1	SEM-based nanoroughness measurement process	140
Figure 6.2	SEM image preprocessing for nanoroughness metrology	141
Figure 6.3	Filtration operation changes the profile and position of a line edge	142
Figure 6.4	Effects of sampling length and sampling interval on values of LER/LWR	142
Figure 6.5	Uncertainty propagation model of SEM-based LER/LWR measurement	143
Figure 6.6	The relationship of measured and real values of LER/LWR for different sampling lengths	152
Figure 6.7	Schematic diagram of how noise effects the apparent measured position of a real line edge	153
Figure 6.8	Schematic of median line fitted from a nanoroughness profile	155
Figure 6.9	SEM image of the fabricated nanograting	157
Figure 6.10	Diagram of the line edge profile extracted from the line edges marked in the red box in Figure 6.9	159
Figure 6.11	Schematic of height correlation function of left line edge marked in red box in Figure 6.9	160
Figure 6.12	Diagram of the relationship between nanoroughness and S	160
Figure 7.1	Diagram of a nanoscale multi-stepheight specimen	170

LIST OF TABLES

Table 2.1 LER in lithography metrology technology requirements-long term 24
Table 2.2 LWR in lithography metrology technology requirements-long term 24
Table 4.1 Mismatching ratio between GaAs and AlGaAs 77
Table 4.2 Linewidth and RMS σ of LER/LWRs of the nanolinewidth specimen 96
Table 4.3 Pitch and RMS σ of LER/LWR of the nanopitch specimen 96
Table 4.4 Correlation length ξ of the line edges of the nanolinewidth specimen 97
Table 4.5 Correlation length ξ of the line edges of the nanopitch specimen 98
Table 4.6 Roughness exponent α of the line edges of the nanolinewidth specimen 99
Table 4.7 Roughness exponent α of the line edges of the nanopitch specimen 99
Table 5.1 Comparison of relevant properties for some high k dielectrics and silicon oxides 105
Table 5.2 Thickness and LER/LWR of HfO_2 and Mo films annealed at different temperatures (unit: nm) 128
Table 5.3 Calculated correlation lengths ξ (unit: nm) and roughness exponents α of line edge profiles of dielectric HfO_2 and Mo films 128
Table 5.4 Relationships of the annealing temperature, the surface roughness and the leakage current densities of the deposited HfO_2 dielectric films 129
Table 5.5 LER/LWR (unit: nm) of HfO_2 films annealed at different temperatures 130
Table 5.6 Correlation length ξ (unit: nm) and roughness exponent α of line edge profiles of HfO_2 films 131
Table 6.1 Relative measurement error of LER/LWR with different sampling length 152

LIST OF PUBLICATIONS

Journal

Z.D. Jiang, F.X. Zhao, W.X. Jing, Philip D. Prewett, and Kyle Jiang. *Motif Parameters Based Characterization of Line Edge Roughness of a Nanoscale Grating Structure*. Key Engineering Materials. 2010. **437**:45-50.

Z.D. Jiang, X.Y. Zhou, Q. Zhu, Z.X. Zhao, H.R. Wang, Philip D. Prewett, and Kyle Jiang. *Recent study on the related problems in evaluation of mechanical properties for MEMS materials*. International Journal of Applied Mechanics. 2009. 1(**4**): p765-779.

Z.D. Jiang, L.B. Zhao, Y.L. Zhao, Y.H. Liu, Philip D. Prewett, and Kyle Jiang. *Oil-filled Isolated High Pressure Sensor for High Temperature Application*. Key Engineering Materials. 2010. **437**:397-401.

Conference

Z.D. Jiang, F.X. Zhao, W.X. Jing, Philip D. Prewett, and Kyle Jiang. *Characterization of Line Edge Roughness and Line Width Roughness of Nano-scale Typical Structures*. 4th IEEE International Conference on Nano/Micro Engineering and Molecular Systems. Shenzhen, 2009. p299-303.

Z.D. Jiang, F.X. Zhao, W.X. Jing, C.Y. Wang, Philip D. Prewett, and Kyle Jiang. *Estimation of measurement uncertainty of LER/LWR based on the next generation GPS*. 10th International Symposium on Measurement and Quality Control. Osaka, 2010. p F1-154-1-4.

Z.D. Jiang, L.B. Zhao, Y.L. Zhao, Philip D. Prewett, and Kyle Jiang. *Research and evaluation of a high temerature pressure sensor chip*. 4th IEEE International Conference on Nano/Micro Engineering and Molecular Systems. Shenzhen, 2009. p 661-665.

CHAPTER 1

INTRODUCTION

1.1. Introduction to the Research Project

Nanoroughness is defined as the roughness at the nanoscale of a line or a surface. It is becoming a very important specification for many nanostructures and nanodevices since it affects the performance of components based on nanostructures, such as the electrical performance of transistors[1.1], the capacitance of thin dielectric films[1.2], the light scattering in optoelectronic devices[1.3], the flow in micro/nano channels[1.4], and the adsorption of proteins on surfaces[1.5] and the wetability of surfaces[1.6]. Nanoroughness does not scale down with the dimensions of the nanostructures/nanodevices of interest. It alters significantly not only the physical or chemical properties of a material, but also the operation of corresponding nanostructures/nanodevices.

Self-affine fractal surfaces and quasi-periodic surfaces are usually produced from various patterning processes for nanostructures and nanodevices, such as lithography,

etching and deposition processes[1.7]. A self-affine surface looks the same after an affine transformation. Nanoroughness is frequently employed to describe the properties of these surfaces. Nanoroughness metrology can directly connect the performance of a nanostructure (nonalinewidth and nanopitch specimens) or a nanodevice (a capacitor with HfO_2 film with a high dielectric constant) with a specific process, hence ensuring the quality of a product of interest[1.8].

The nanoroughness study framework can be generally outlined as shown in Figure1.1[1.7]. This framework is made up of three parts as shown below: 1) identifying nanostructure and nanodevice specifications (related to nanoroughness) to demonstrate the importance of nanoroughness for the operation of the nanostructure and nanodevice as well as the specifications for nanoroughness control; 2) developing nanoroughness metrology and characterization methods to quantify nanoroughness; 3) selecting material and processes to ensure the required level of roughness.

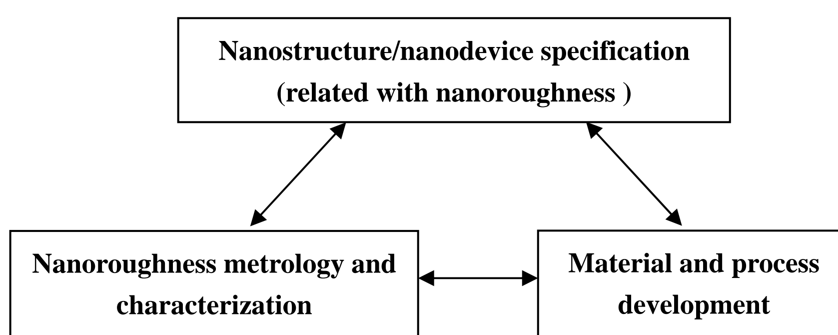

Figure 1.1- Nanoroughness study framework[1.7].

For nanoroughness characterization, two metrological approaches are usually used: 1) instruments such as Scanning Electron Microscopy (SEM), Atomic Force Microscopy (AFM), High Resolution Transmission Electron Microscopy (HRTEM), and Near-field Scanning Optical Microscopy (NSOM) etc. are employed to get the aerial

images of features of interest[1.9]; 2) mathematical tools from scaling theory are used to characterize the dimensional or geometrical features, such as the root-mean-square (RMS) σ, the height-height correlation function (HHCF) and the power spectral density (PSD), etc[1.7], as describe in Section 3.2.2. Usually a three parameter model is enough for the description of self-affine edges, which includes the RMS value σ, the correlation length ξ and the roughness exponent α [1.7]. In some cases, especially for the characterization of 3-D surfaces, these three parameters are not sufficient to describe the features of interest[1.10]. New parameters and algorithms are required to describe the detailed characteristics of the features in order that more accurate metrology information could be fed back to nanostructures and nanodevices modeling as well as to material selection and process control.

This research project is part of an ongoing cooperative project between the University of Birmingham and Xi'an Jiaotong University (PR China) financially supported by the National Nature Science Foundation of China. The title of the project is 'Traceability and metrology in nanomanufacturing'.

1.2. Aims and Objectives

The aims of the research project are to establish the relationship between the performance of nanostructures and nanodevices and roughness resulting from specific processes, and eventually to put forward a standard proposal for Standardization Administration of the People's Republic of China/Technical Committee 336 (SAC/TC336). The specific samples and device for test fabrication are nanolinewidth and nanopitch of less than 10 nm, and a metal-insulator-semiconductor (MIS)

structure with a HfO_2 film as a high k dielectric material.

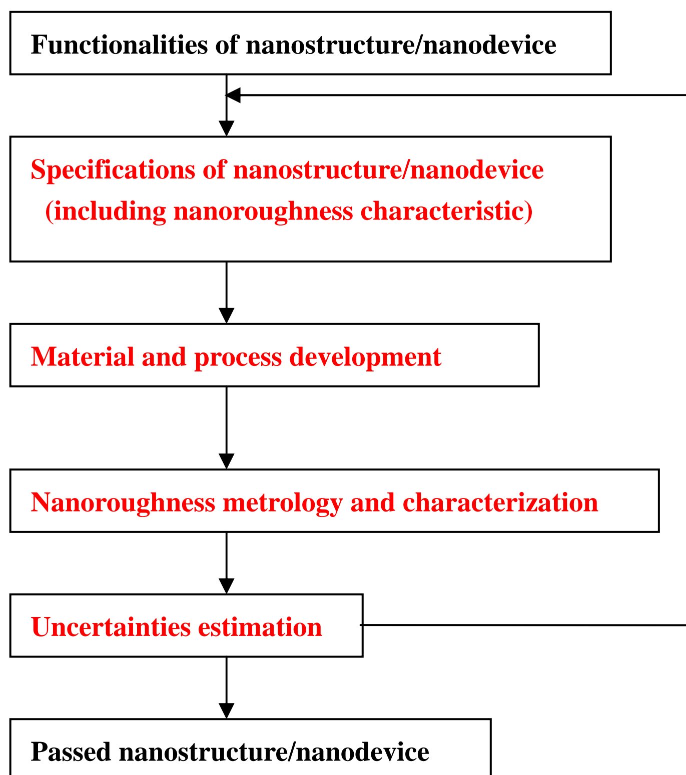

Figure 1.2- Study flow of nanoroughness metrology.

Nanoroughness metrology and its effect on the nanostructure/nanodevice performance is a mulit-disciplinary subject. Specification of nanostructure/nanodevice, nanoroughness metrology and characterization, material selection and process control, as well as measurement uncertainty estimation, all play a critical role in nanoroughness effect on nanostructure/nanodevice performance. Figure 1.2 illustrates the areas of importance relating to nanoroughness metrology and its effect on nanostructure/nanodevice performance. Under each of the areas, several issues have been identified. Also issues in one area can have relationships with other areas. Specifications of nanostructure/nanodevice, material selection and process control, nanoroughness metrology and characterization as well as the measurement

uncertainty estimation, which are the foci of this project, are highlighted in red in Figure 1.2.

To achieve the project aims above, project objectives are set out as follows:

1) Review the current development of nanoroughness metrology and the effects of nanoroughness on specific nanostructure/nanodevice performance.

2) Simulate and visualize the effect of the characteristic descriptors on the properties of given random rough curves and surfaces.

3) Employ molecular beam epitaxy (MBE) technique to fabricate nanolinewidth and nanopitch specimens with both the nominal linewidth and nominal pitch less than 10nm.

4) Fabricate MIS capacitors with HfO_2 film as the high k dielectric, and dielectric thickness of about 60nm.

5) Perform nanoroughness characterization and electrical testing for nanolinewidth/nanopitch specimens as well as the MIS capacitors, and regulate specific process parameters in term of the nanoroughness metrology and characterization.

6) Conduct uncertainty estimation for SEM-based roughness metrology.

1.3. Thesis Structure

This thesis consists of seven chapters. Chapter 1 introduces the topic of nanoroughness metrology and its effect on the performance of the nanostructures and the nanodevice covered by this thesis. It identifies the increasing effects of nanoroughness metrology and characterization on the performance of various

nanostructures and nanodevices. The project's aim and objectives are set out in this chapter.

Chapter 2 reviews the current research progress on nanoroughness metrology and its effects on the performance of various nanostructures and nanodevices. It first analyzes the challenges in nanoroughness metrology, including nanoroughness measurement and characterization. This is followed by the effects of nanoroughness on properties of various nanostructures/nanodevices, including nanoscale reference specimens, the capacitance of thin dielectric films, the electrical properties of sub-50nm metal-oxide-semiconductor transistor etc. Finally it proceeds to measurement uncertainty estimation for nanoroughness metrology, involving uncertainty estimation for the instruments employed and nanoroughness metrology operations.

Chapter 3 discusses the characterization and simulation of self-affine curves and 3-D rough surfaces. The chapter starts with the characterization and simulation of self-affine curves, including characterization parameters and the simulation of the effect of these parameters on the variation of the critical dimension. This is followed by the characterization and simulation of 3-D rough surfaces, including the simulation of Gaussian, non-Gaussian, complicated and self-affine random rough surfaces. This chapter presents detailed descriptors and algorithms for the nanoroughness characterization in the following chapters.

Chapter 4 presents the MBE-based fabrication and characterization of nanolinewidth and nanopitch specimens. The detailed design and fabrication processes for the above mentioned specimens are presented, including the selection of materials for the

specimens and the identification of the process parameters. Then HRTEM-based line edge roughness (LER) and line width roughness (LWR) of the fabricated specimens are discussed and characterized. Taking characterization of LER and LWR into consideration, this chapter finally proceeds to describe regulating specific process parameters in order to improve the quality of the above mentioned specimens.

Chapter 5 investigates nanoroughness metrology and its effects on the properties of the MIS capacitor with HfO_2 films as the high k dielectric. It first presents the design and the process flow for the capacitor in detail. Then it proceeds to the electrical performance measurement and the interface/surface roughness characterization for the capacitor. This is followed by the effect of interface/surface roughness on electrical performance. Finally it covers the regulation of specific process parameters for the fabrication of the MIS capacitor, from a consideration of the characterization of interface/surface roughness.

Chapter 6 deals with the measurement uncertainty estimation for nanoroughness measurement. The chapter first presents theoretical fundamentals of measurement uncertainty. This is followed by the uncertainty propagation model for SEM-based nanoroughness measurement, including the preprocessing of SEM aerial images. For preprocessing, three operations are investigated in detail; these are filtering, extraction and fitting. Then this chapter proceeds to the evaluation of uncertainties produced by SEM. This is followed by the uncertainty estimation for SEM image processing. Finally this chapter presents a case study, showing the detailed uncertainty estimation flow for SEM-based nanoroughness measurement.

Conclusions on nanoroughness metrology and its effect on nanostructure/nanodevice performance are presented in Chapter 7 where the main findings obtained from this study are summarized. Some possible future work is also suggested.

1.4. Summary

This introductory chapter describes the need for a systematic approach to nanoroughness metrology and its effect on the performance of the nanostructures (nanolinewidth and nanopitch specimens) and a nanodevice (an MIS capacitor with a HfO_2 film as the high k dielectric). The research, its aims and objectives and an introduction to the structure of this thesis have been described. Although the main motivation of this research is to perform nanoroughness metrology and characterization for the nanolinewidth and nanopitch specimens (with the normal linewidth and the normal pitch both less than 10nm) as well as the MIS capacitor (with 60nm HfO_2 film as the high k dielectric), the nanoroughness metrology and characterization, the relationships between performance of nanostrutures/nanodevices and relevant process control, and measurement uncertainty estimation all have the opportunity to open up new applications in other fields of nanotechnology.

CHAPTER 2

A REVIEW ON FABRICATION AND NANOROUGHNESS CHARACTERIZATION OF SPECIFIC NANOSTRUCTURES AND NANODEVICES

2.1. Introduction

This chapter presents a review on the background relating to the research work. The proposed research is planned to be carried out on the basis of the existing technology and to develop it further.

The review starts with challenges in nanoroughness metrology. Then it proceeds to the fabrication of nanolinewidth and nanopitch specimens. The survey also examines nanoroughness modeling and visualization. Recent research progress on the effects of nanoroughness on the properties of specified nanostructures/nanodevices is covered in detail. The uncertainty evaluation for SEM-based metrology for CD and nanoroughness will be discussed. Examples from each category will be investigated, particularly in the field of nanoroughness metrology. Attention is paid to the regulation of the fabrication process according to relevant nanoroughness

characterization by other researchers.

2.2. Challenges in Nanoroughness Metrology

As mentioned in Chapter 1, nanoroughness is regarded as a critical specification for various nanostructures and nanodevices[2.1]. It influences strongly not only the electrical, mechanical, magnetic, optical and fluidic performances of nanostructures and nanodevices, but also the relevant fabrication optimization and material selection[2.2-2.7]. Nanoroughness metrology is being investigated in various disciplines and for many engineering applications[2.8-2.10].

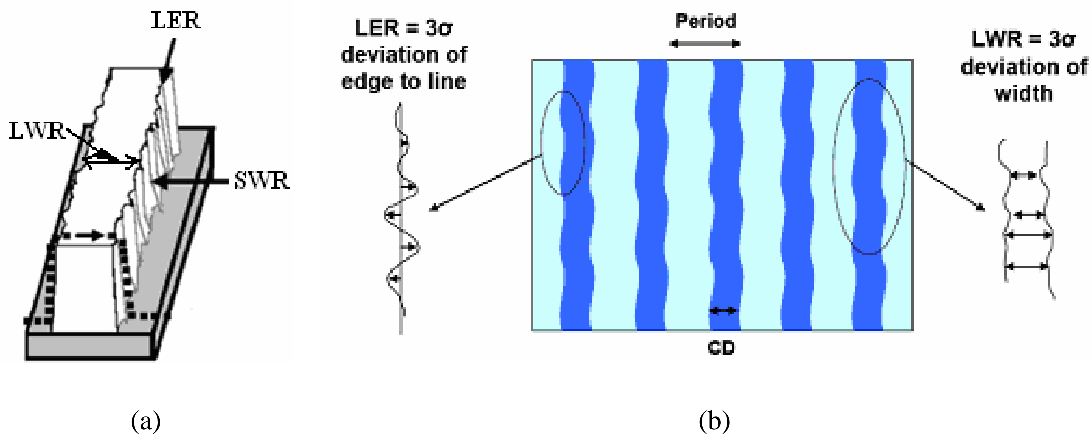

(a) (b)

Figure 2.1 – (a) Schematic diagram of LER, LWR and SWR[2.11]. (b) Definitions of LER and LWR[2.13].

Five kinds of nanoroughness are investigated in the nanotechnology community; they are line edge roughness (LER), line width roughness (LWR), sidewall roughness (SWR), interface roughness and surface roughness.[2.11, 2.12]. LER refers to the root-mean-square (RMS) deviation of a line edge coordinates, while LWR is defined as the corresponding RMS deviation of a line width[2.13]. Figure 2.1 shows a schematic diagram of the above mentioned roughnesses[2.11] as well as the

definitions of LER and LWR[2.13].

Challenges in nanoroughness metrology mainly come from three aspects: developing instruments for nanoroughness measurement, characterizing relevant nanoroughness, and establishing the relationships between nanodevice performances, nanoroughness and the corresponding quality control of the fabrication process[2.14, 2.1].

For the development of instruments for nanoroughness metrology, one major issue is to fabricate corresponding standard nanoscale specimens for calibration and traceability; the other is to evaluate the measurement uncertainty for the specific instrument[2.15, 2.16]. Challenges in nanoscale specimen fabrication include material selection and introduction of new fabrication techniques to produce specimens with less critical dimensions and high accuracy. Research in this area is reviewed in Section 2.3. SEM is a widely-used instrument in the nanometrology community. Evaluation of SEM measurement uncertainty plays an important role in the process of increasing measurement accuracy[2.17, 2.18]. Issues to evaluate SEM-based method uncertainty and implementation uncertainty are investigated widely by different research groups. The challenges in this area are covered in Section 2.6.

In regard to nanoroughness metrology, issues of research interest include characterization, simulation and visualization of various random surfaces and curves produced by fabrication processes[2.19-2.21]. Challenges in this area include selection of descriptors, the effect of a specific descriptor on the properties of a random surface or curve, and the regulation of the fabrication process based on nanoroughness characterization. They are discussed in Section 2.4.

Nanoroughness effects on the properties of nanostructures and nanodevices were investigated by a wide variety of research groups from multiple academic disciplines[2.22-2.24]. The main challenge is to establish the relationship between nanoroughness and the specific property of nanostructures/nanodevices of interest. This is covered in Section 2.5.

2.3. Fabrication of Nanolinewidth and Nanopitch Specimens

Nanoscale specimens are frequently employed to help measure specific nanoscale parameters and to calibrate various nanoscale instruments, such as scanning tunnelling microscopy (STM), AFM, SEM, TEM and NSOM, etc[2.14]. For a certain measurand, the specimen provides a datum for comparisons of measurement results not only between different measurement instruments, but also between different measurement positions for the same instrument[2.14]. Fabricating relevant nanoscale specimens is one important aspect of nanometrology[2.25]. The size features of different specimens include linewidth, pitch, step height, slope. Figure 2.2 shows schematic diagrams of frequently-used specimens in nanometrology [2.26].

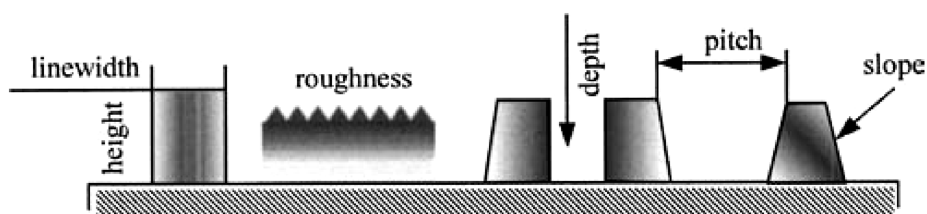

Figure 2.2 – Schematic diagram of frequently-used specimens[2.26].

Fabricating different nanoscale specimens involves many challenges from the micro/nano-manufacturing area. The fabrication of specimens is becoming more and more dependent on very specialist processes using a wide range of very expensive

facilities[2.25]. Various fabrication processes were proposed by different research groups and corporations for supplying different specimens for nanometrology. These processes and the corresponding specimens are summarized below.

McClelland et al[2.27] at National Institute of Standards and Technology proposed laser-focused atomic deposition to fabricate nanoscale pitch standard specimens. The laser light (wavelength around 300nm) was stabilized at the frequency near a strong optical absorption line in chromium atom. Through the standing wave of the laser light (as an array of 'lenses' for Cr atoms) the atoms were evaporated onto a sapphire substrate, and the average pitch is nominally half the laser wavelength (see Figure 2.3). A pitch specimen of 212.7787nm with a combined standard uncertainty of 0.0049nm was fabricated shown in Figure 2.4. According to the fabrication principle, the unique characteristic of this technique is that the average pitch can be traced directly to an atomic transition frequency.

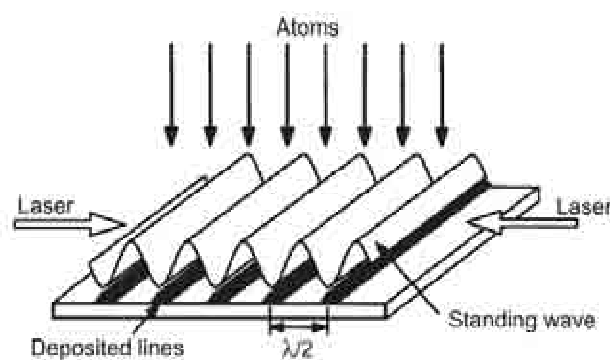

Figure 2.3 – Schematic diagram of laser-focused atomic deposition process[2.27].

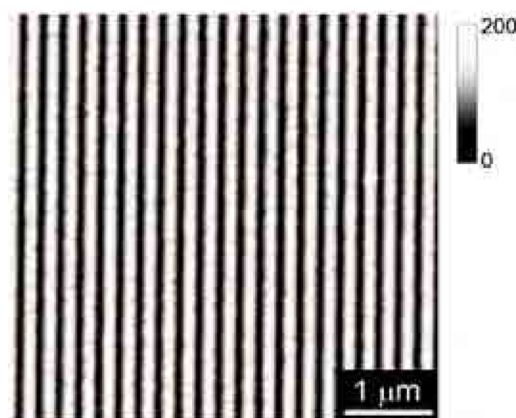

Figure 2.4 – AFM image of the fabricated specimen[2.27].

AFM tip-induced anodic oxidation on a Si(100) substrate was employed to fabricate a nanopitch pattern with a nominal pitch of 95nm[2.28]. The oxidation of the Si substrate is an electrochemical process[2.29, 2.30] and is induced by the electric field

of the conducting AFM tip. The ultimate oxide thickness that can be grown is limited by dielectric breakdown events. The lateral resolution of the process is primarily determined by a condensed film of water that forms near its apex. Figure 2.5(a) shows the fabricated nanopitch pattern with a pitch of 96nm.

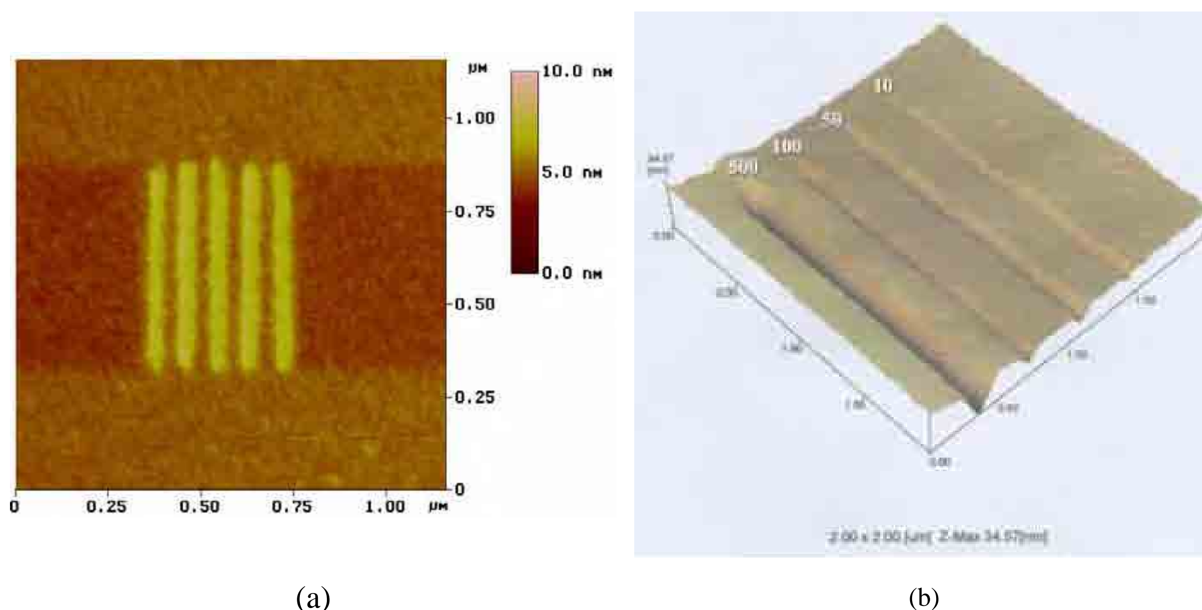

(a) (b)

Figure 2.5 – AFM image of the fabricated grating lines. (a) Oxide lines produced on Si (100) substrate[2.28]. (b) Grating line patterns scratched on Al substrate [2.31].

The AFM tip scribing technique was also used to fabricate similar nanopatterns on an Al substrate [2.31, 2.32]. With an AFM in the scribing mode and a force applied on the AFM cantilever, an Al film deposited by an RF sputtering system was scratched by the tip at the end of the cantilever and formed a fine groove. The rectangular cantilever with higher stiffness for scribing was made of stainless steel coated with platinum, and the diamond tip at the end of the cantilever was a pyramid with an apex angle of60° and tip radius of about 15nm. For the groove measurement with the same AFM, a cantilever with a lower stiffness was used, and its tip was made of Si_3N_4. Figure 2.5(b) demonstrates the scratched grating line pattern. The minimum groove

width of the fabricated pattern was less than 50nm.

The significant advantage of AFM-based techniques is that the fabrication and the traceability of the fabricated pitch can be integrated in one system on condition that two laser interferometers are placed in the x and y directions [2.33].

Tortonese et al[2.34] at VLSI Standard Inc. presented another way to produced sub-50nm isolated trench and line width specimens. The method is based on an idea regarding the specific layer thickness of a deposited multilayer structure as the nominal linewidth of the desired specimen. After growing an oxide layer, by thermal oxidation on two silicon wafers, and bonding them together, the structure was put into a buffer oxide etch solution, etching back the oxide layer to a desired length and producing an isolated trench, see Figure 2.6(a). For line width specimen in Figure 2.6(b), both the silicon and silicon oxide layers were deposited on a silicon wafer alternately. After the subsequent processes including silicon oxide etching in the buffer oxide etch solution, the silicon line protruded out, forming the linewidth specimen.

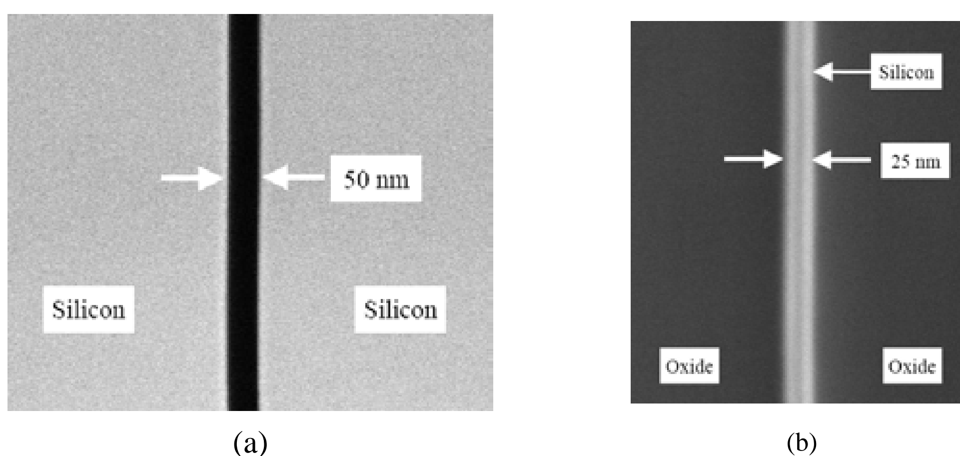

(a) (b)

Figure 2.6 – SEM images of the respective trench and line. (a) Trench width 50nm. (b) Line width 25nm[2.34].

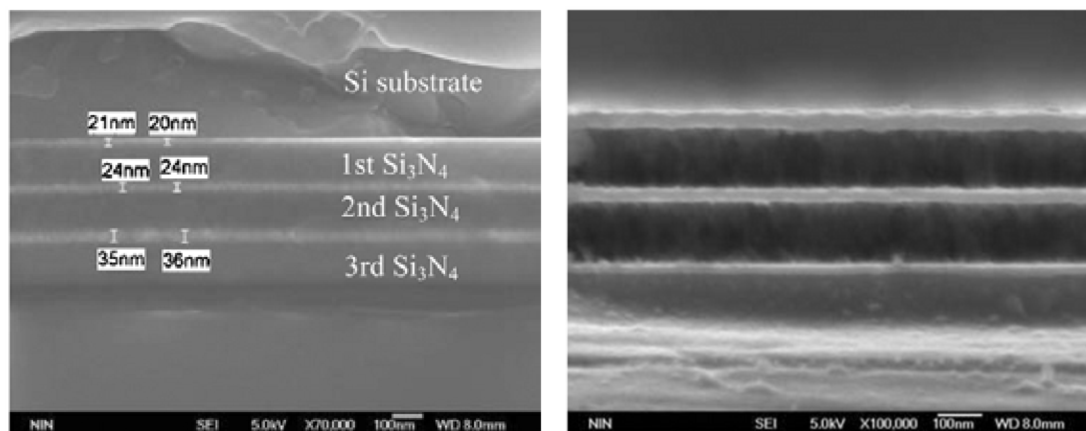

(a) (b)

Figure 2.7 – SEM diagrams of THE fabricated nanoscale specimen[2.35]. (a) Linewidths of the specimen. (b) Si_3N_4 layers were etched off by RIE process for 100 seconds.

A similar method is described in the literature[2.35] in which chrome and silicon nitride layers were deposited on a Si substrate by radio frequency (RF) magnetron sputtering followed by low-temperature plasma enhanced chemical vapor deposition (PECVD), as shown in Figure 2.7(a). Figure 2.7(b) demonstrates the chrome linewidth pattern with the silicon nitride partially etched off by reactive ion etching(RIE).

The advantage of this method is the high uniformity of the fabricated lines and trenches which arises from the application of thin film deposition technologies.

The Lateral Pattern Definition (LPD) process was employed to fabricate specimens with precisely-controlled nanoscale width [2.36]. Figure 2.8 shows the fabrication process for LPD. First Si_3N_4 (23nm-49nm) was deposited on a <110> Si wafer (see Figure 2.8(a)), and standard optical lithography was used to produce Si_3N_4/Si steps shown in Figure 2.8(b). Then the wafer was thermally oxidized at a temperature range

of 800-950°, see Figure 2.8(c). Later the Si_3N_4 layer was etched off selectively (Figure 2.8(d)). Finally Si was etched by a high selective plasma process, resulting in the desired line pattern with linewidth below 100nm (see Figure 2.8(e)). The advantages of this process include its low cost and ease of fabrication for line patterns less than 100nm.

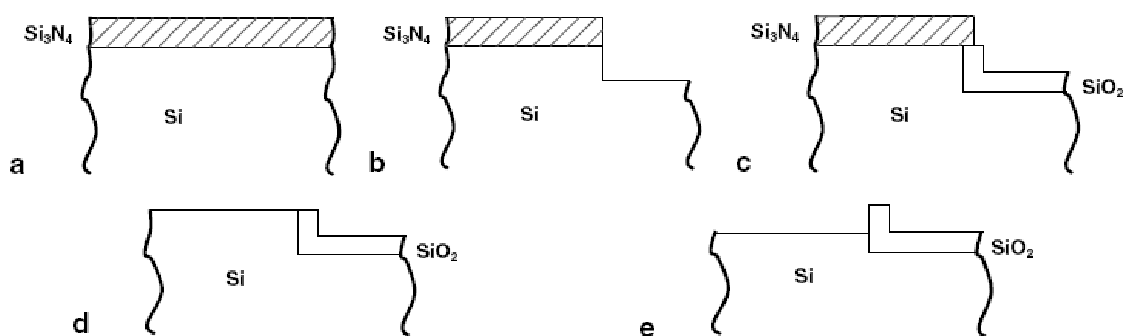

Figure 2.8 – Diagram of LPD process for patterns with linewidth less than 100nm[2.36].

From the above review it can be concluded that the main disadvantage of these techniques is the difficulty of fabricating nanoscale specimens with nominal linewidth less than 10nm. Other techniques and materials should be employed and investigated.

MBE is a technique for epitaxial growth by the interaction of one or several molecular or atomic beams at the surface of a heated crystalline substrate[2.37]. It can deposit layers of materials with atomic thicknesses onto the substrate, hence it is a potential candidate to fabricate specimens with linewidth less than 10nm. The MBE technique will be introduced and investigated to fabricate nanoscale linewidth and pitch specimens later in this thesis.

2.4. Modeling and Visualization of Nanoroughness Metrology

Patterning processes usually produce self-affine fractal and quasi-periodic surfaces, and these random rough surfaces demonstrate either Gaussian, non-Gaussian, fractal,

or complicated properties[2.1, 2.38]. Compared with experimental investigation, modelling and visualization of these random rough surfaces are more flexible, and can create reference data and decrease relevant investigation cost and time[2.39]. In order to describe these surfaces and analyze relevant properties, scaling theory is used, assisted by simulation and visualization.

In order to simulate rough random surfaces for specific applications, many algorithms have been employed[2.40]. In 1972 a multivariate-multidimensional random process with a given spectral density was proposed to synthesize a rough surface[2.41]. In 1978 a linear transformation on random matrices was used to generate a matrix of rough amplitudes with a given autocorrelation function (ACF) matrix, while time series and Fast Fourier Transform (FFT) were widely employed also[2.42]. In 1982 auto-regressive (AR) and moving average methods were used to generate rough surfaces[2.43, 2.44]. In 1991 FFT, auto-regressive and moving average were used[2.45]. In 1992 finite impulse response filters were employed[2.46]. In 1995 FFT was used to produce a one-dimensional fractal profile[2.47]. Specific simulation process should be carefully selected in order to meet the requirements of the desired engineering surfaces.

Gaussian random surfaces can be synthesized with given spectral density or ACF in more than two directions[2.40]. Figure 2.9(a) shows the generated 50×50-point surface with a given spectral density and sampling interval 0.01μm[2.40]. Figure 2.9(b) shows the height distribution for the simulated surface, which has a Gaussian distribution[2.40]. In the case of only one surface being simulated, this method can

guarantee the profile of the surface has the correct ACF, but for several profiles being simulated, it cannot, although the average ACF of the profiles is very close that required.

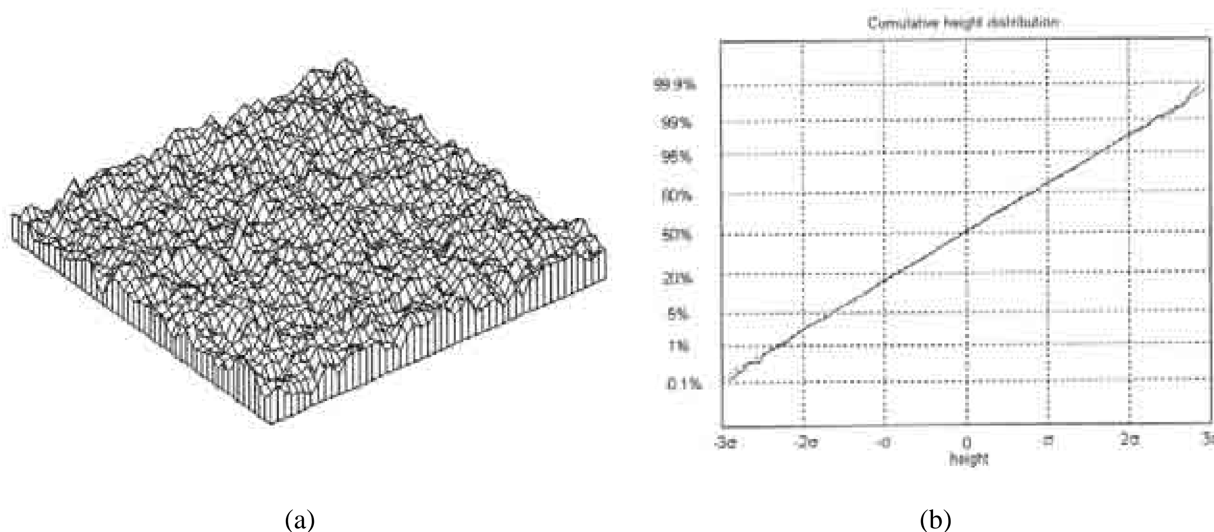

(a) (b)

Figure 2.9 – The generated surface with given spectral density and sampling interval 0.01μm. (a) The 3-D rough surface. (b) Height distribution of the generated surface[2.40].

In the literature[2.48] non-Gaussian surfaces with given skewness, kurtosis and spectral density or ACF were generated by FFT. From the given spectral density or auto-correlation function the amplitude of the surface was generated, while the phase of the surface was obtained by the Johnson translator system. Figure 2.10(a) and (b) show the height distribution and the spectral density of the generated surface. The standard deviation, skewness and kurtosis of the target profile are 1nm, -0.5 and 5.0, while that of the generated one are 0.9746nm, -0.5 and 5.0. Good agreement between two profiles was found, showing the simulation validity.

Figure 2.11 shows the simulation and visualization of random rough surfaces with the fractal model[2.49]. The Mabdelbrot-Weierstrass (W-M) equation with different fractal dimensions D and randomly-generated phase Φ was used to visualize the

simulated surfaces. The simulation shows that the surface roughness in the fractal model was scale-independent and could be described by fractal dimension D, one of the major advantages of the fractal modelling.

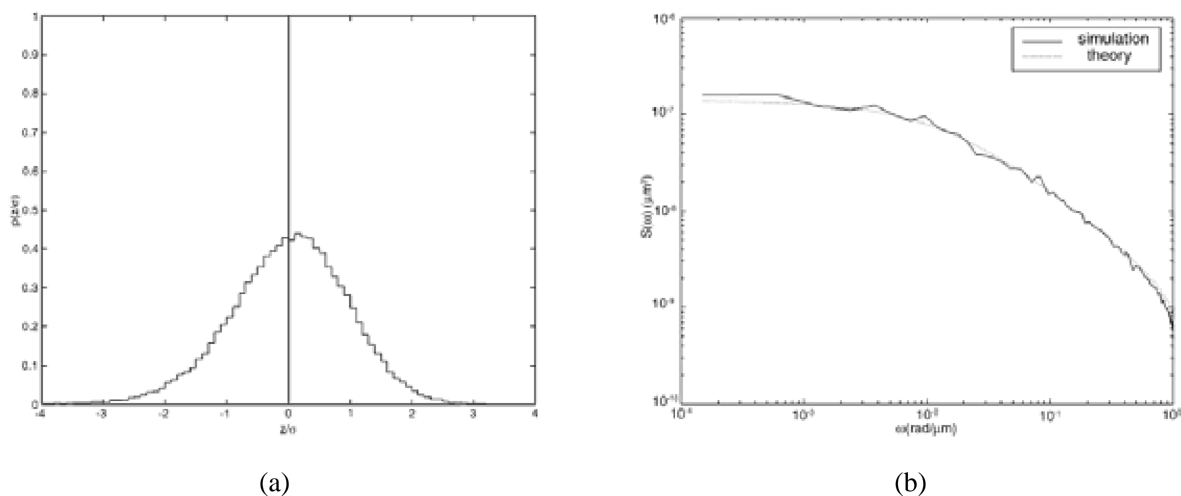

(a) (b)

Figure 2.10 – The generated surface with given spectral density and sampling interval 0.01μm [2.48]. (a) Height distribution. (b) Spectral density.

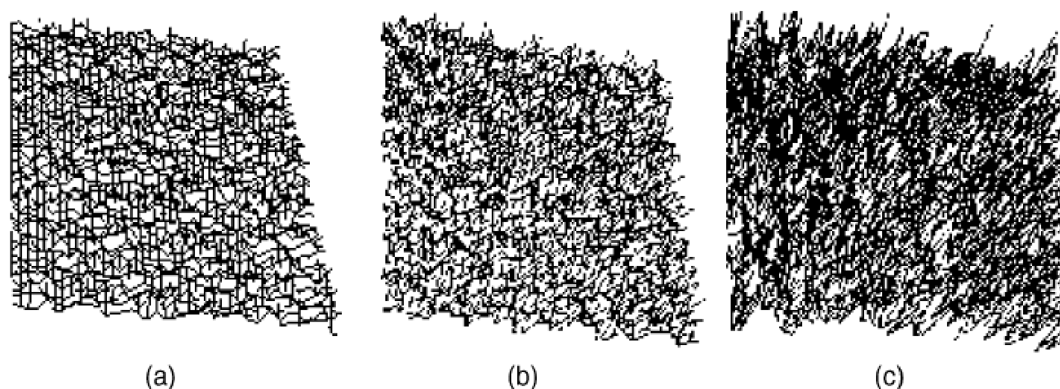

Figure 2.11 – Surfaces simulated with M–W equation for different fractal dimension D: (a) D =1.3, (b) D=1.5 and (c) D=1.8[2.49].

In order to establish the relationship between process parameters and roughness parameters, the back propagation algorithm along with the gradient descent learning procedure in artificial neural networks was employed[2.50]. Figure 2.12 demonstrates the detailed network topology [2.50]. The network trained with experimental data can

predict corresponding roughness for specific process parameters, thus establishing the relationship between specific fabrication process and relevant roughness parameters.

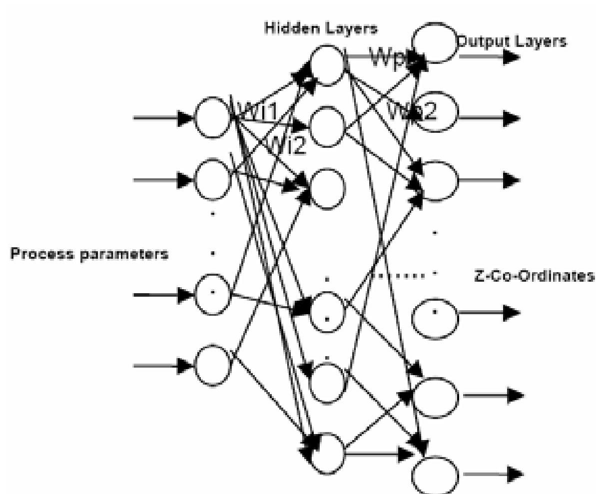

Figure 2.12 – Network topology with process parameters as input layer and roughness parameters as output layer[2.50].

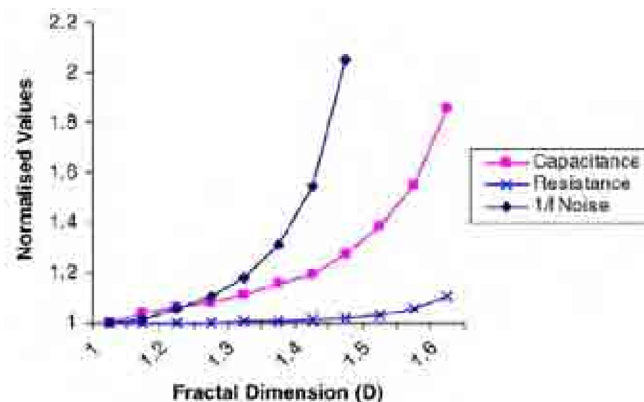

Figure 2.13 – Relationship between resistance, capacitance, 1/f noise spectral density and fractal dimension D[2.50].

Figure 2.13 exhibits the relationship between the capacitance of an interconnect capacitor and the fractal dimension D of one rough plate of the capacitor, while the other plate is supposed to be perfectly smooth [2.50]. It can be seen that the capacitance increased as the fractal dimension D became larger. Figure 2.13 demonstrates the simulated effect of roughness on the resistance of thin films. It was concluded that low values of the fractal dimension had less effect on the capacitance, while the roughness effect on the capacitance of the thinner films were more significant than that on thick ones.

The relationship between 1/f noise and corresponding surface roughness of the Cu film is also demonstrated in Figure 2.11. Lorentzian spectra were used to simulate the noise, in which the calculation of the spectral density was based on the electron tunneling between hillocks on the rough surface, introducing the process parameters

into the model. The larger the fractal dimension, the larger the noise.

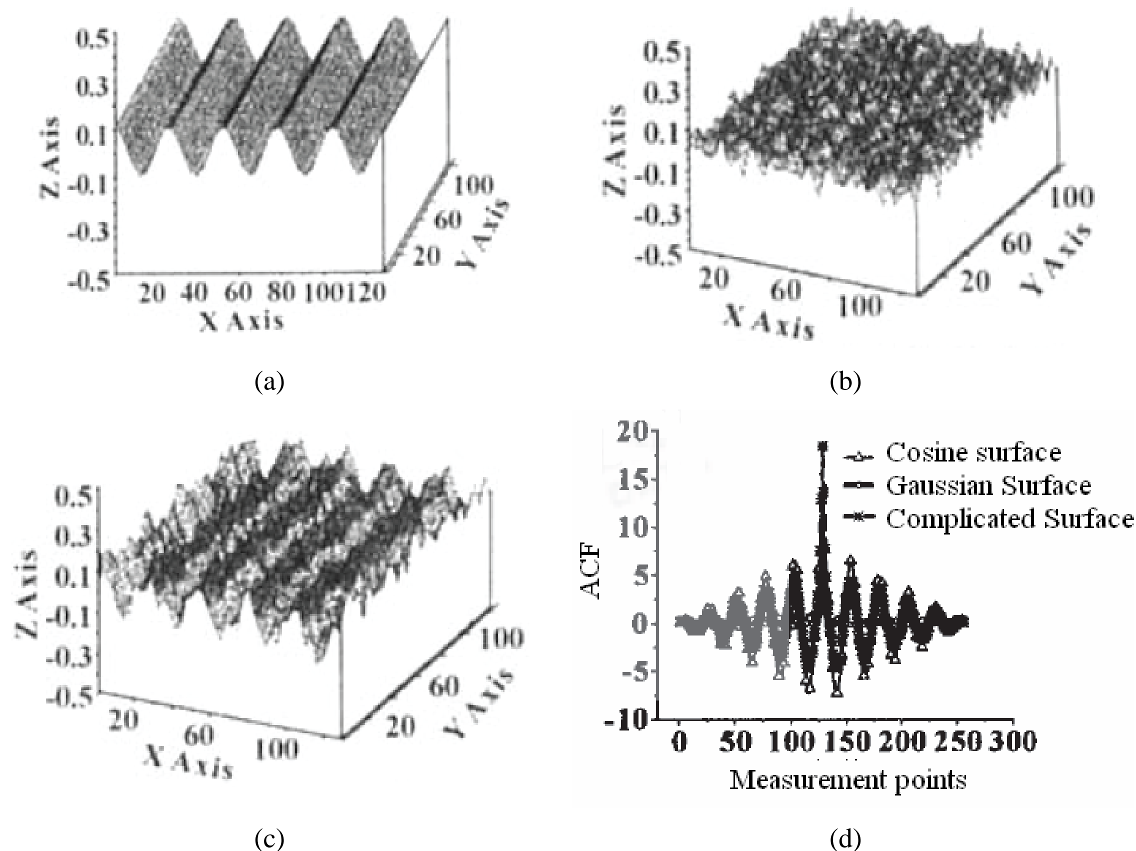

Figure 2.14 – The simulation of a complicated rough surface[2.52]. (a) A cosine surface. (b) A Gaussian surface. (c) A complicated rough surface. (d) The ACF comparison of the three rough surfaces.

Only a few reports have been traced on simulation of complicated random rough surfaces. Wold [2.51] proposed that any discrete stationary process could be described as the sum of two processes which are totally uncorrelated, one is a deterministic process, the other is non-deterministic. According to this theory, engineering surfaces were also regarded as the sum of two or more Gaussian surfaces, hence a complicated random rough surface could be simulated by the combination of a periodic surface and a Gaussian surface[2.52]. Figure 2.14 shows the surface components and the combined complicated rough surface. The ACF of the simulated complicated surface demonstrated not only the periodic component, but also an exponential one (also the

property of ACF of a Gaussian rough surface). Much work has still to be conducted in this area.

From the above review one can conclude that several algorithms were employed to generate 3-D random rough surfaces, such as the W-M function, ACF, PSD, auto-regression and multivariate-multidimensional random process, etc., while Monte Carlo simulation and the convolution method are frequently used to produce random sequences with given properties. Although these algorithms had been employed already by different research groups, in each of their publications only one or two properties of 3-D rough surfaces were investigated. Random rough surfaces with different properties remain to be systematically investigated and visualized.

2.5. Effects of Nanoroughness Metrology on the Properties of Nanostructures/ Nanodevices

Nanoroughness impacts on the performance of a wide range of nanostructures and nanodevices. One example is from the semiconductor industry. The International Technology Roadmap for Semiconductors (ITRS) is a set of documents produced by a group of semiconductor industry experts every few years. These experts are representatives of the sponsoring organizations which include the Semiconductor Industry Associations of the US, Europe, Japan, Korea and Taiwan. In 2001 LER was introduced in the edition of the ITRS Metrology 2001[2.53]. Table 2.1 shows the LER requirements for different technology nodes[2.53]. In ITRS Metrology 2003, LWR replaced LER and was introduced to analyze an increase in transistor leakage current (see Table 2.2) [2.54]. ITRS Metrology 2003 also pointed out that although CD-SEM

and lithography process simulation systems had software to determine LER, there was no standard method to evaluate LER, demonstrating standardized assessment of LER and LWR according to the roadmap requirements was not possible.

Table 2.1 – LER in lithography metrology technology requirements-long term[2.53].

Year of Production	2001	2003	2004	2007	2010	2013	2016
DRAM ½ Pitch (nm)	130	100	90	65	45	32	22
LER (nm, 3 σ)	4.5	3.3	2.7	1.8	1.3	0.9	0.65

Table 2.2 – LWR in lithography metrology technology requirements-long term[2.54].

Year of Production	2010	2012	2013	2015	2016	2018
DRAM ½ Pitch (nm)	45	35	32	25	22	18
LWR (nm, 3 σ)	1.4	1.1	1.0	0.8	0.7	0.6

2.5.1. Capacitance of Thin Insulating Films

LER significantly affects not only the capacitance of thin insulating films, but also interconnects, with cross-sectional dimensions below 100nm, of CMOS transistors[2.55]. Artificial periodic square-shaped LER in the meander-fork structure of the narrow Cu wire was introduced to investigate its effect. This method demonstrated two disadvantages, one is that the artificial LER is far from being stochastic, the other is that the measurement methodology is indirect[2.55]. To overcome these drawbacks, a discrete random sequence of roughness amplitudes was used to simulate the LER, which was obtained by the inverse Fourier transform of Gaussian or exponential approximations of the measured auto-covariance function(see Figure 2.15(a)). This sequence was regarded as a relevant roughness and

superimposed on an ideal interconnect architecture model with no LER, and wire capacitance and resistance were eventually extracted(see Figure 2.15(b)). Figure 2.15(c) demonstrates other frequently used approximations to the measured auto-covariance function. The simulations concluded that the higher the roughness amplitudes and the smaller the correlation lengths, the larger the capacitance C. A similar behavior was observed for resistance R.

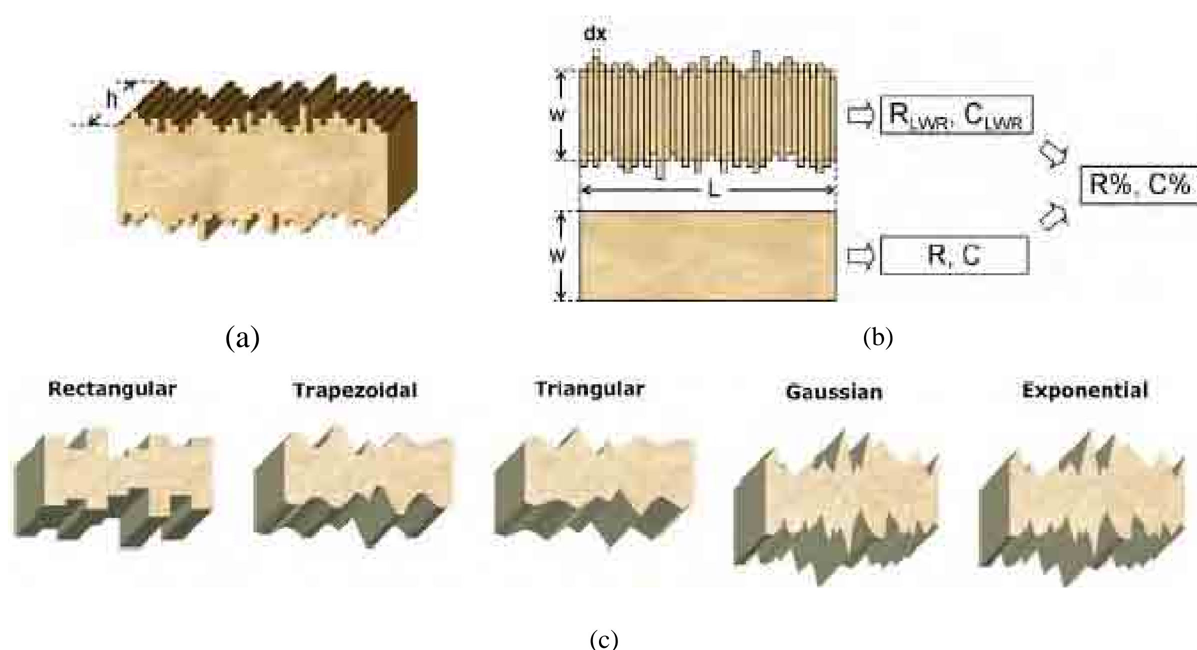

Figure 2.15 – Simulation of LER effect of Cu interconnect on its performance[2.55]. (a) Discrete random sequences as roughness amplitudes. (b) LWR effects on resistance R and capacitance C. (c) Other approximations of the measured auto-covariance function.

The ITRS roadmap 2005 has employed the above mentioned simulation methodology with the exponential approximation of LER for scaling the interconnect dimensions. Figure 2.16 shows the simulations of LER for the resistance and capacitance of the meander-fork Cu interconnect for future technology nodes[2.55]. In Figure 2.16(a), the correlation length and $3\sigma_{LWR}$ of the LWR were set as 20nm and 6nm respectively. Also in Figure 2.16(b), the correlation length was set as 20nm, and $3\sigma_{LWR}$ was scaled

as predicted by the ITRS roadmap.

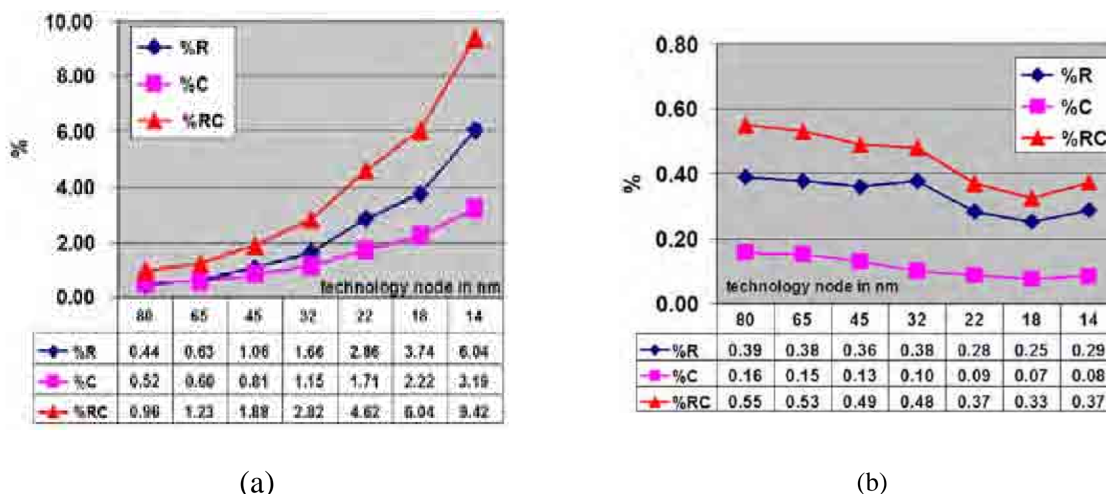

(a) (b)

Figure 2.16 – Estimated impact of different LWRs on Cu interconnects for future technology nodes[2.55]. The y-axis percentage means the growth rates of resistance R, capacitance C and time constant RC respectively.

SiO_2 is frequently employed as a dielectric material for a MIS capacitor adopted in semiconductor devices. With continuous shrinkage of semiconductor devices, the equivalent oxide thickness (EOT) of the SiO_2 film has to be very thin, resulting in large leakage current and worsening the stability and reliability of relevant devices[2.56]. In order to overcome this drawback, high k dielectrics are introduced to replace SiO_2. Due to its high dielectric constant and thermal stability when in its amorphous structure, HfO_2 is a promising candidate for the next-generation of MOSFET devices [2.57-2.59]. Influential factors which affect the performance of the MIS capacitor with HfO_2 as a high k dielectric include the morphology and the grain structure quality of the deposited HfO_2 film, and they are highly correlated micro-structural observables[2.60]. In the literature, an MIS capacitor was made up of the upper and lower electrodes(ruthenium and p type Si respectively) as well as HfO_2 film. The Ru electrodes were deposited by atomic laser deposition(ALD) and physical

vapor deposition(PVD). AFM was employed to characterize the surface morphologies of Ru thin films. Figure 2.17(a) and (b) show the curves of the capacitance versus voltage and the electric field versus leakage current for the MIS capacitors[2.60]. It was concluded that different fabrication processes produced different surface morphologies, and an increase in the interface roughness resulted in a decrease in the dielectric constant and an increase in the leakage current.

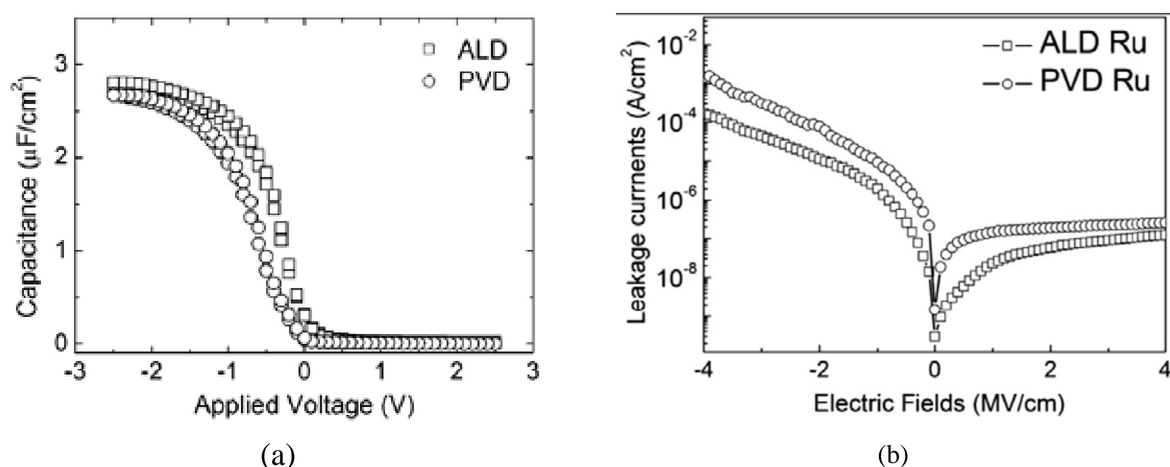

Figure 2.17 – Interface roughness effect on the performance of the MIS capacitor with HfO_2 as high k dielectric[2.60]. (a) C-V curves. (b) Electric fields vs leakage currents.

Mixed thin films of high k dielectric materials and silica were employed to produce high quality dielectric films for the MIS capacitor[2.61]. The promising composites are hafnia–silica (HfO_2:SiO_2) and zirconia–silica (ZrO_2:SiO_2) systems. The morphologies of the mixed thin films were measured by an AFM. RMS roughness, power spectral density, height-height correlation and autocorrelation analysis were employed to characterize the surface morphologies, and to further investigate their evolution.

Figure 2.18 demonstrates the characterization of the surface morphologies[2.61]. It is concluded that the addition of silica in the composite hafnia films resulted in

appreciable morphological and grain structure transformations, especially at lower silica contents. That is, the hafnia–silica composite films exhibited a more favourable morphological evolution compared with the zirconia–silica thin film samples.

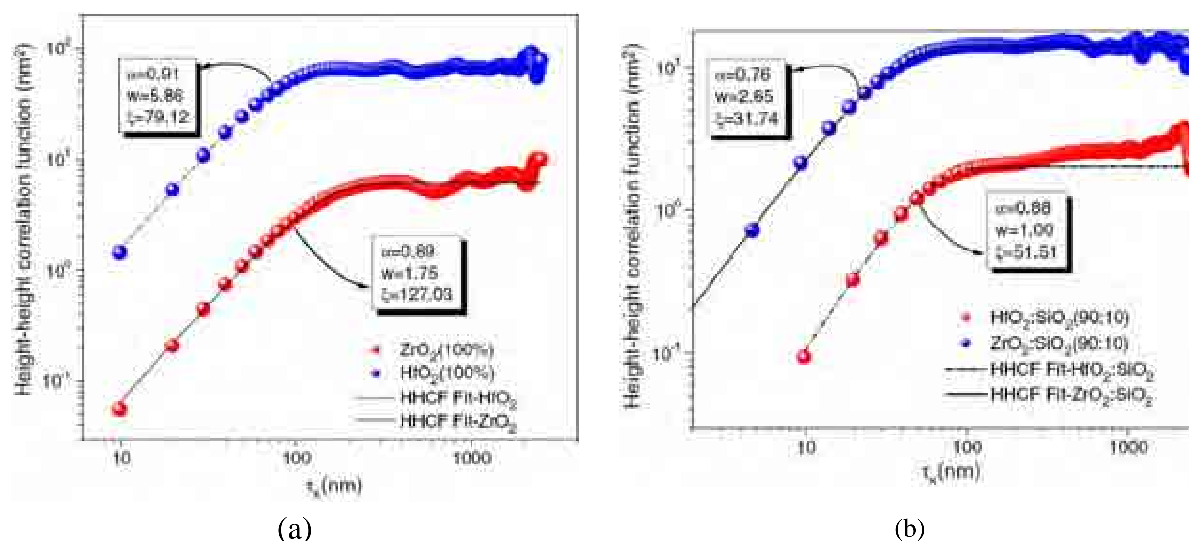

(a) (b)

Figure 2.18 – Nanoroughness of pure and composite thin films of the high k dielectrics [2.61].

2.5.2. Electrical Properties of Sub-50nm MOS Transistors

The LER of the gate line of the sub-50nm MOSFET device impacts significantly on its performance. The effect falls into two categories, one is performance degradation(see Figure 2.19(a)), the other is performance variation(see Figure 2.19(b)) [2.62]. For the degradation of a MOSFET device, the LER of the gate line may result in larger leakage current, degrading the device performance. With regard to the performance variation of several devices, the LER of the gate lines may cause performance fluctuation. Also the width variation (another kind of LER) may make its own contribution to performance fluctuation(see Figure 2.19(c)) [2.62].

Here W_g denotes the width of a MOSFET device, L_g denotes its length, V_g is the voltage applied to the gate of the device and I_d is the drain current. The

characterization process for the above mentioned LERs can be summarized as follows: SEM images of the device were obtained; then the images were noise-smoothened and the line edge profiles were extracted with corresponding algorithms; finally RMS σ and CD were used to evaluate relevant roughness, and the LER effect on the device performance was estimated, including the degradation and variation.

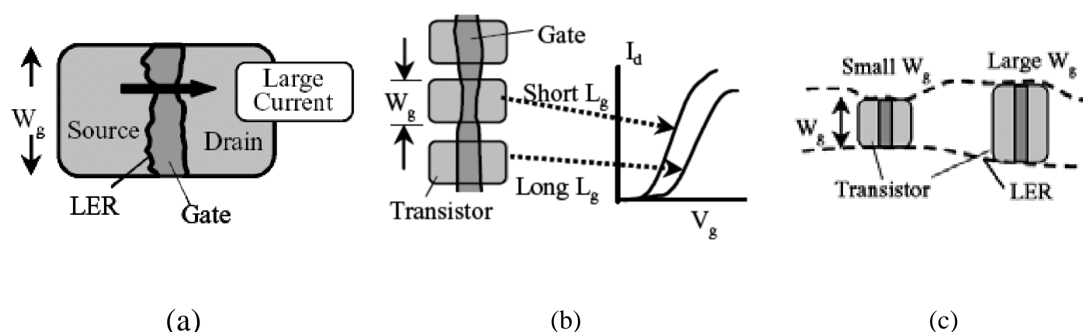

(a) (b) (c)

Figure 2.19 – Three modes of LER influence on sub-50nm transistor performance[2.62]. (a) The degradation of one MOSFET device. (b) The variation of several MOSFET devices along the gate length direction. (c) The variation of several MOSFET devices along the gate width direction.

2.5.3. Light Scattering in Optoelectronic Devices

One kind of silicon light emitting device is based on the MOS device structure. As for the Si-substrate based device, additional momentum is required for the light emission process [2.63]. The rough oxide scattering is one way to provide this additional momentum for the radioactive electron-hole recombination, hence requiring an increase of the interface roughness at the oxide/Si interface[2.63].

In this work [2.63] a very high vacuum pre-bake before rapid thermal oxidation was used to increase the oxide roughness. With the oxide roughness increased, the light emission intensity and the emission efficiency of the device increased also. Figure 2.20 demonstrates these detailed relationships[2.63]. Here the oxide thickness was

measured by ellipsometry, the roughness by an AFM, and RMS σ was employed to descript the roughness.

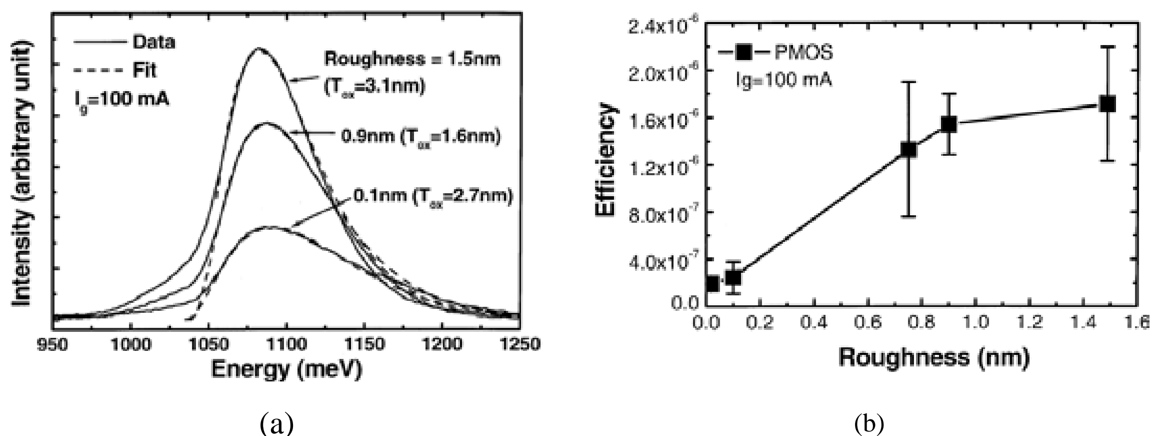

(a) (b)

Figure 2.20 – Nanoroughness effect on the light scattering in optoelectronic devices[2.63]. (a) Light emission intensity versus the oxide roughness. (b) Relationship between the oxide roughness and light emission efficiency.

2.5.4. Adsorption of Proteins on Surfaces

Biocompatibility means the chemical and structural compatibility of a material integrated in the desired biological environment. Recent studies have recognized the importance of not only the chemical compatibility, but also surface topography [2.64].

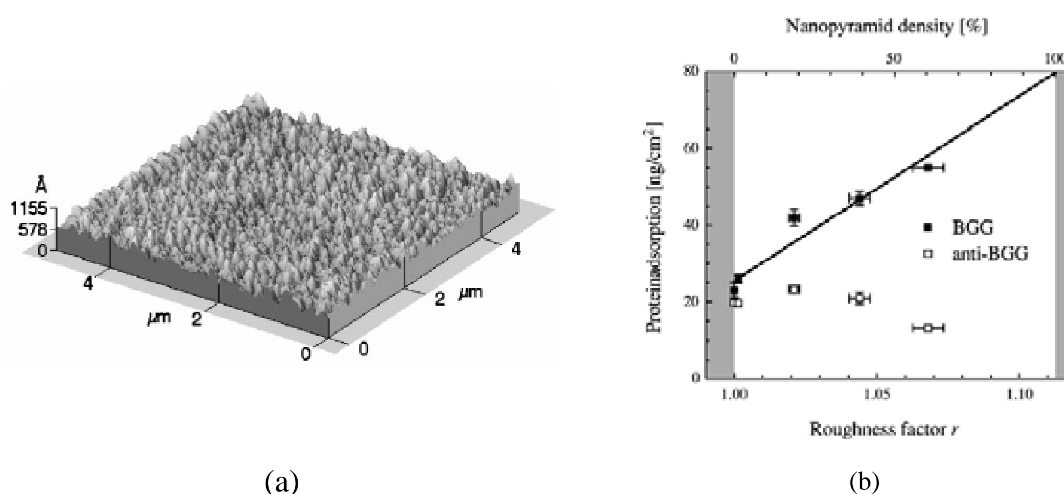

(a) (b)

Figure 2.21 – Evolution of the contact diameter on rough surfaces with time scales[2.64]. (a) Linear time scale. (b) Logarithmic time scale.

In the literature [2.64] ultrahigh vacuum chemical vapor deposition was used to grow well-defined germanium nanopyramids naturally on a Si(001) substrate. The density of the nanopyramids was precisely controlled by the growth conditions. Then the silicon substrate with the Ge nanopyramids was exposed to air so that the sample was oxidized. The ratio of the effective surface to the projected one (that is, roughness factor) was used to characterize the surface roughness with high precision (also the effective surface). Bovine γ-globumin(BGG) with sizes comparable to the nanopyramids was labelled with fluorescein isothiocyanate, and fluorescence spectroscopy was employed to obtain the quantity of BGG adsorbed on substrates with different densities of the nanopyramids. Figure 2.21(a) shows the AFM image of a fabricated substrate. Figure 2.21(b) demonstrates the protein adsorption of BGG vs roughness factor. From Figure 2.21(b) one can conclude that the amount of adsorbed BGG was more than a factor of 2 higher on the rough than on the flat substrate, although the effective surface only increases by 7%.

2.5.5. Wettability of Surfaces

Nanoroughness also affects the dynamics of wetting and de-wetting of solid surfaces. In the literature[2.65] single-side polished silicon wafers were processed to create a thin, hydrated silicon dioxide layer that was highly hydrophilic, and used as a substrate on which to culture osteoblasts. Surface roughness was measured by an AFM in tapping mode with a Si_3N_4 V-shaped cantilever, and characterized using the parameters such as the arithmetic average roughness(R_a), the root mean square roughness(R_q), the roughness surface ratio(r) and the fractal dimension (D_f) of the

surface.

Figure 2.22(a) demonstrates the relationship between surface roughness and cell proliferation. It was concluded that the number of cells increased with R_a, while R_q and the roughness surface ratio r gave a saturation value for cell proliferation[2.65]. Figure 2.22(b) shows the relationship between surface roughness characterized by the fractal dimension D_f and cell proliferation [2.65]. The cell proliferation increased with D_f, and no saturation was found in the curve.

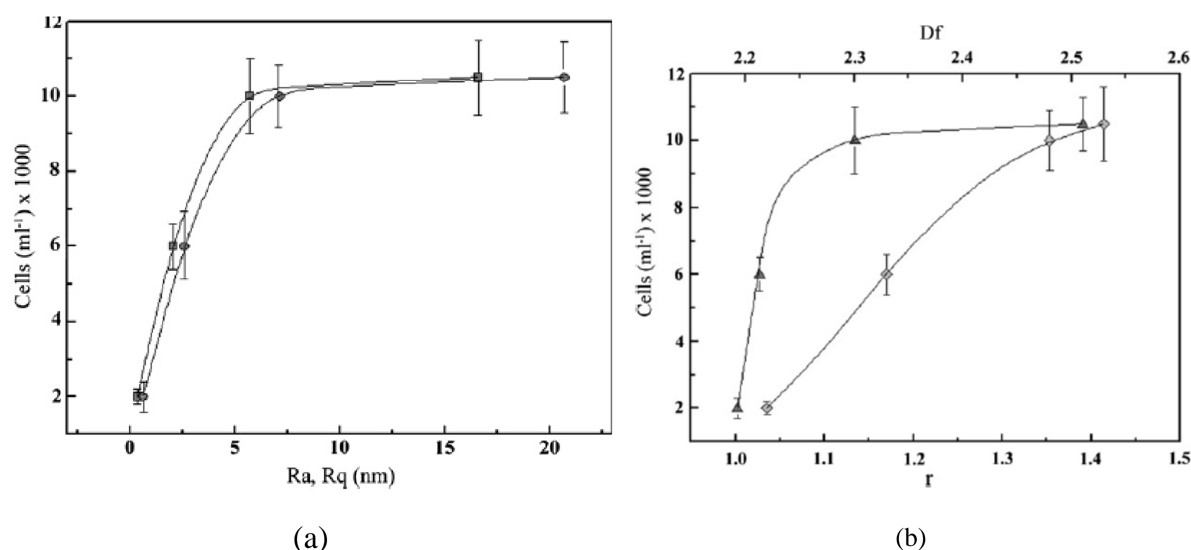

Figure 2.22 – Relationship between the number of cells released from the samples and surface roughness[2.65]. (a) Roughness described by Ra (squares) and Rq (circles). (b) Roughness described by the roughness surface ratio r (triangles) and D_f (diamonds).

The review above shows that nanoroughness impacts the performances of a wide variety of nanostructures and nanodevices. In the literature only one or two descriptors of relevant nanoroughness was (or were) frequently used by different groups. The detailed properties of relevant nanoroughness were not characterized. In order to establish an accurate relationship between performance and the process used to make a specific nanostructure or nanodevice, the method of determining and

characterizing the nanoroughness should be explained in detail, especially for nanoscale specimens and the MIS capacitor with HfO_2 as a high k dielectric.

2.6. Uncertainty Evaluation of SEM-based Metrology

Relevant standards of ISO Geometrical Product Specifications and Verification (ISO GPS) classify the uncertainties of a product as measurement uncertainty, correlation uncertainty, specification uncertainty, compliance uncertainty and total uncertainty[2.66]. Figure 2.23 shows the detailed relationships between the above mentioned uncertainties[2.66]. In Figure 2.23 measurement uncertainty is the sum of measurement uncertainty and implementation uncertainty. The Guide to the Expression of Uncertainty in Measurement (GUM) and ISO 14253-2 present the corresponding process and algorithms for the evaluation of the measurement uncertainty [2.67,2.68]. Accordingly SEM-based measurement uncertainties fall into two kinds, one kind from the SEM instrument itself (the implementation uncertainty), the other kind from the operations of relevant image processes and characterization (the method uncertainty).

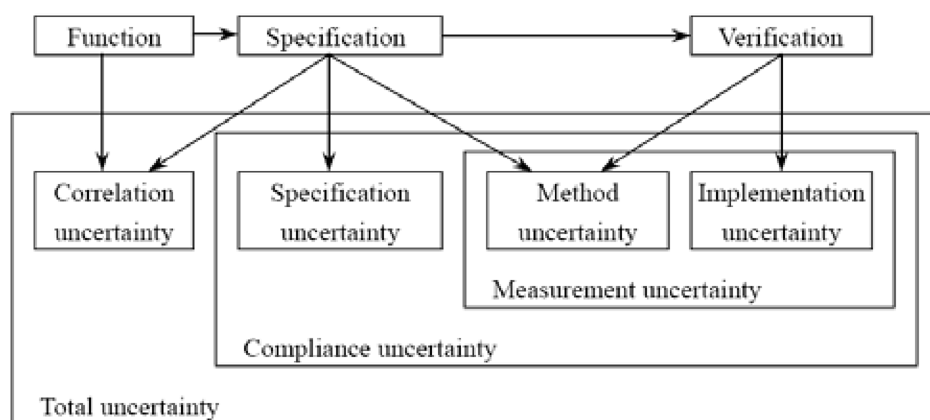

Figure 2.23 – Relationships between various uncertainties of a geometric product[2.66].

2.6.1. Implementation Uncertainty of SEM-based Metrology

In the implementation uncertainty of SEM measurement, one main influential factor is the assignment of a line edge position which produces significant uncertainty [2.69]. Line edge positions in the SEM image of a specimen should be accurately assigned in order to get measurement results with high accuracy. Three methods are being employed to assign line edge positions, namely the threshold edge criterion[2.70, 2.71], the model-based library[2.72] and the piecewise-defined continuous function[2.73]. A review of these three methods follows.

Of the threshold approaches to determine a line edge position, one simple and frequently-used method is based on the SEM image grey scale of the nanostructure directly as shown in Figure 2.24[2.70]. Linewidth (that is, the distance between the positions of both edges of the nanostructure) varies according to the changes of the threshold, hence corresponding uncertainties are introduced. This method is more random and empirical, resulting in larger uncertainty for CD and LER/LWR measurements.

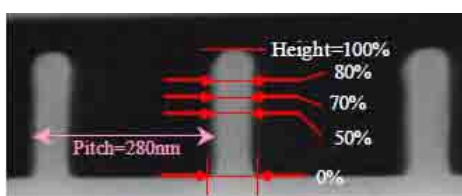

Figure 2.24 – Threshold-based determination of the linewidth[2.70].

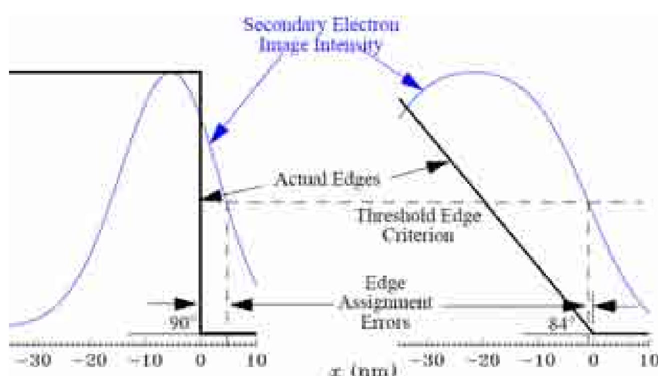

Figure 2.25 – The Edge assignment errors caused by the threshold edge criterion[2.71].

The other threshold method is based on the profile of the SEM signal intensity for the

nanostructure. Figure 2.25 demonstrates the schematic to determine the edge position of a nanostructure[2.71]. With the threshold value on the SEM image intensity varied (here the threshold is set half way between the intensity peak and the baseline), the position of the line edge changes too, introducing relevant uncertainties in the measurement of the line width, space width or LER/LWR. In this example, the sidewall angle variation of the nanostructure contributes considerably to the uncertainty of the edge position determination. Also the smoothing operation for the SEM grey scale image may broaden the SEM signal intensity profile and cause a change in assignment of the edge position.

In order to assign the position of a line edge more accurately and quickly, Villarrubia et al [2.72] at NIST established an SEM model-based library of typical specimens by Monte Carlo simulation. First the specimen shape was parameterized, and then the eight parameters were iteratively adjusted to obtain the best least squares fit to the measured image. Since it is very time-consuming to use a Monte Carlo simulator frequently for the iterative calculation, a library of simulation results for parameters covering the process space of interest was established in advance. If the measured SEM signal profile does not agree with the simulated ones, a function will be employed to interpolate the SEM model-based library rapidly, hence increasing the calculation efficiency.

Figure 2.26(a) shows the model library-based measurement process, and Figure 2.26(b) demonstrates the comparison of the width bias as a function of sidewall angle for a specimen obtained by four frequently-used methods, namely the maximum

derivative, the regression to baseline, the sigmoidal fit and the model-based library[2.74]. The width bias produced by the approach of the model-based library is less than that generated by other ones, and more stable along with the change of the sidewall angles of the specimens, reducing the error of the line width measurement.

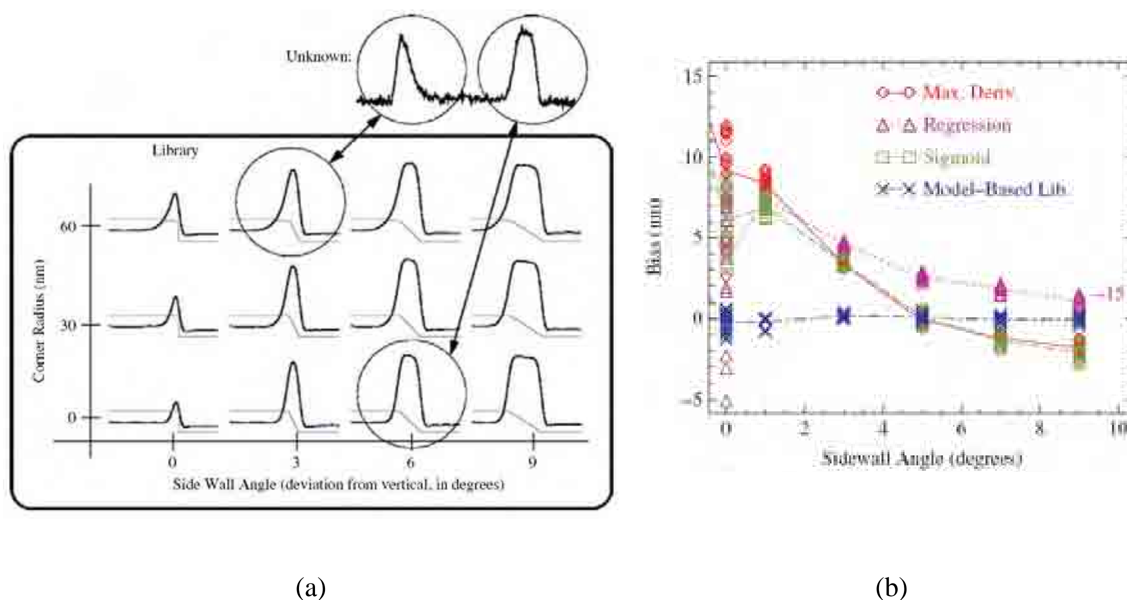

(a) (b)

Figure 2.26 – Schematic of the model-based library (a), and the comparison of the width bias obtained by four methods(b) [2.72].

In order to overcome the drawbacks of the model library-based approach, Frase et al [2.73] at Physikalisch-Technische Bundesanstalt(PTB) presented a new algorithm to evaluate the CD of nanostructures from SEM images. Figure 2.27 demonstrates electron diffusion by a Monte Carlo simulation at a silicon line and the corresponding secondary electron image, and Figure 2.28 shows the new algorithm based on the physical modeling of the SEM image formation by Monte Carlo simulation[2.73]. A piecewise-defined continuous function with five characteristic parameters was employed to model the SEM intensity profile, here x1 is the foot of the left edge, x2 is the shoulder of the left edge, x3 is the point of the transition from the left edge to the

right edge, x4 is the shoulder of the right edge, and x5 is the foot of the right edge. A least-squares fit is used to approximate the measured profile extracted from the images, and the five characteristic parameters can be obtained. Hence the CD values can be directly determined as follows: TopCD=x4-x2, and BottomCD=x5-x1.

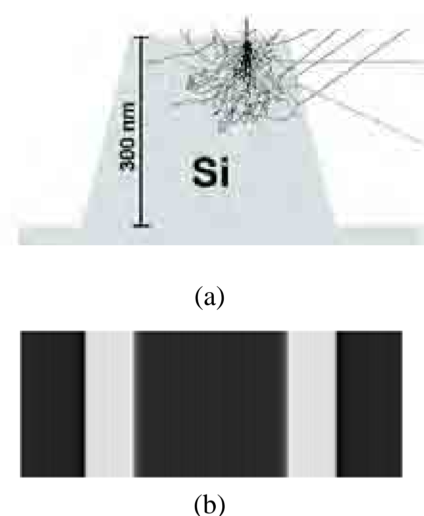

Figure 2.27 – (a) Simulation of the secondary electron diffusion at a silicon line. (b) the corresponding secondary electron image [2.73].

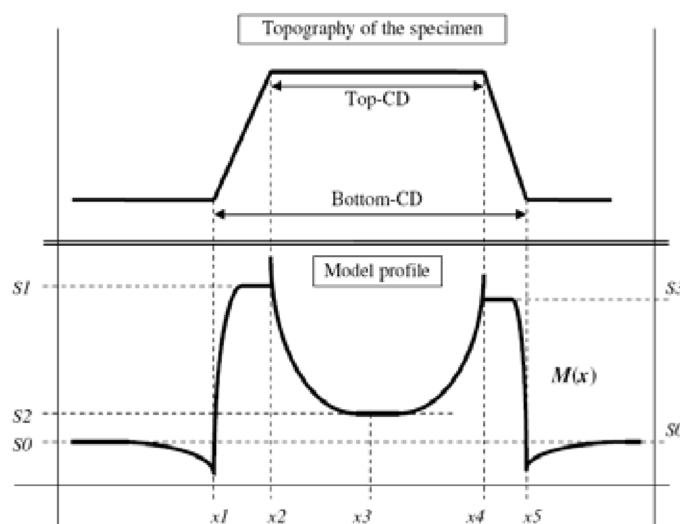

Figure 2.28 – The topography of the structure and its corresponding model profile [2.73].

2.6.2. Method Uncertainty of SEM-based Metrology

Method uncertainty is mainly caused by filtering, extraction and fit operations[2.66]. For example, the mean value filter, median filter and Gaussian filter are three frequently used to smooth SEM images[2.75]. With different filters being employed to smooth the SEM image, corresponding uncertainty is introduced.

With regard to the extraction of the line edge profiles from the smoothed SEM image, Prewitt, Canny, Sobel, Log, Canny, and Robert operators are employed widely[2.76]. Wavelet transform-based multi-scale line edge detection is a new operator developed in recent years[2.77]. The use of different extraction operators also leads to

uncertainty.

Fit operators for the median line of the extracted line edge profile also cause uncertainties for the determination of line edge positions as well as for LER/LWR[2.78]. Generally two algorithms are available to fit corresponding median line of the line edges of a given SEM image, one is the least-squares median line, the other the arithmetic average median line. Different fit operators result in different characterization of LER/LWR, hence introducing uncertainty in LER/LWR characterization.

The following conclusions can be obtained from the above review. Either implementation uncertainty or method uncertainty of SEM-based measurement has been estimated already by different research groups, but in every publication only one or two uncertainty (-ies) was (or were) investigated. SEM-based nanoroughness metrology requires the evaluation and combination of all uncertainties produced in the measurement process, this still remains to be systematically investigated and estimated.

2.7. Summary

A review on nanoroughness metrology is presented. Various techniques were used to fabricate nanolinewidth and nanopitch specimens, the major disadvantage of these techniques is the difficulty of producing specimens with nominal linewidth and pitch less than 10nm. The MBE technique is a potential candidate to deposit GaAs and GaAsAl films alternately on a GaAs substrate with film thickness less than 10nm; hence it will be introduced in this thesis. This is followed by the modeling and

visualization of various random rough surfaces. Real rough surfaces demonstrate Gaussian, non-Gaussian or fractal properties, and most publications discuss only one or two properties of 3-D rough surfaces. In this thesis the emphasis will be on the simulations of the detailed properties of various rough surfaces. This review also covers the effects of nanoroughness on the performances of various nanodevices, especially the MIS capacitor with HfO_2 as high k dielectric. More nanoroughness descriptors than those introduced in many publications are needed to establish the relationships between the performances of nanodevices and nanoroughness, and further to regulate the corresponding fabrication process. Finally this chapter presents the review of SEM-based measurement uncertainty evaluation, including the method uncertainty and implementation uncertainty. In this thesis more attention was paid to SEM-based implementation uncertainty than the method uncertainty to improve nanoroughness measurement accuracy.

The review in this chapter has significant influence on the direction of this research. The techniques for the fabrication of the nanostrucutres, the algorithms for nanoroughness simulations and the measurement uncertainty evaluations are identified. The review of the nanoroughness effects on the nanodevices from other institutions has also demonstrated that full descriptors of the nanoroughness characterization need to be introduced in order to improve the quality control for the employed processes. The main challenges faced in this research are identified as the fabrication of the nanoliwidth and nanopitch specimens, as well as the characterization and measurement uncertainty evaluation of nanoroughness.

CHAPTER 3

CHARACTERIZATION AND SIMULATION OF SELF-AFFINE CURVES AND 3-D ROUGH SURFACES

3.1. Introduction

In this study random rough curves and surfaces are characterized, and the effects of their characteristic parameters on the properties of curve profiles and surface textures are investigated and simulated. The intention of the study in this chapter is to visualize these relationships, which also will be employed to characterize the curves of the nanostructures demonstrated in Chapters 4 and 5.

This chapter begins with characterization of random rough curves, including the Weierstrass-Mandelbrot ($W-M$) function for a random rough surface and three descriptors of a 2-D random rough curve[3.1]. Then the effects of LER/LWR parameters on critical dimension (CD) variation are investigated and self-affine curves are visualized in simulation. It is followed by the characterization with six descriptors and relevant simulations of frequently used 3-D rough surfaces, such as Gaussian, non-Gaussian random rough surfaces, complicated and self-affine rough

surfaces.

3.2. Characterization and Simulation of Random Rough Curves

There are various profiles of the grating lines in nanostructures, such as sine, cosine, exponential, Gaussian and self-affine ones, etc. In most cases the amplitude variation of these profiles are different and relationships between both edge profiles of a grating line are correlative or noncorrelative, impacting the properties of specific nanodevices very much.

3.2.1. Fractal Model of a Random Rough Surface

Surfaces produced by micro/nano fabrication techniques almost always are random, disordered and multiscale [3.2]. From a mathematical point of view, profiles of this kind of surface are continuous, anywhere non-differentiable and self-affine. The non-differentiablilty of the surface shows that more detailed information will emerge as the profile of the surface is magnified continuously, meanwhile the tangent does not exist at any point on the profile. The self-affine of a surface means that the self similarity of a profile will appear at different magnification times of the image, see Figure 3.1[3.3].

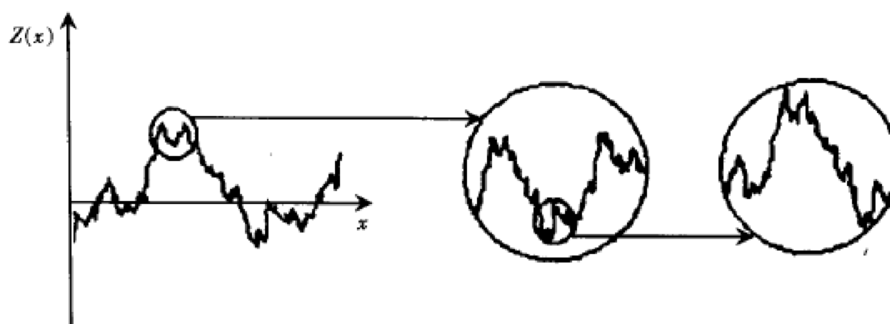

Figure 3.1 - Diagram of the self similarity of a self-affine profile [3.3].

The fractal model of a rough surface based on the $W-M$ function was established by Majumda and Bhushan[3.1] and applied to the profiles of engineering surfaces[3.4]. The $W-M$ function with a fractal dimension D is defined as below:

$$z(x)=G^{(D-1)}\sum_{n=n_l}^{\infty}\frac{\cos 2\pi\gamma^n x}{\gamma^{(2-D)n}} \tag{3.1}$$

Where $z(x)$ denotes the profile of a random surface,

D is the fractal dimension, and $1<D<2$,

G is the factor of the characteristic scale,

γ^n is the spatial frequency of the profile,

n_l is the lowest cut-off frequency of the profile,

γ is the a positive decimal fraction and larger than 1.

The constant γ corresponds to the reciprocal of the wavelength of a rough surface and determines the frequency spectrum of the rough surface. It makes the spatial frequency in Eq.3.1 change as a geometric series, and demonstrates thoroughly the randomness of the rough surface by superimposing every cosine function.

The following properties of the $W-M$ function can be concluded from Eq.3.1[3.4]:

- The self-affine property of a random rough surface can be expressed in Eq.3.2, i.e., with x magnified by γ times, the amplitude z will be enlarged by γ^{2-D} times.

  $$z(\gamma x)=\gamma^{2-D}z(x) \tag{3.2}$$

- Invariability of the power spectrum density (PSD). That is why the $W-M$ function is always employed to characterize the fractal property of a random rough surface.

- The fractal parameters D (the fractal dimension) and G (the factor of the characteristic scale) are independent of the resolution of the instrument and the size of the surface profile.

3.2.2. Descriptors of 2-D Random Rough Curves

The following three descriptors are always used to characterize the profiles of a random rough curve which is self-affine: the root mean square σ of the amplitudes of the surface profile, the height-height correlation function (HHCF) and PSD[3.5].

3.2.2.1. Root Mean Square σ

The RMS, σ, is in common use to characterize the amplitude characteristics of a line profile. It demonstrates the standard deviation of the distances of the points on the line edge from its associated median line. Generally speaking the less the value of σ, the higher the quality of the line edge. The definition of RMS for LER and LWR of a line profile are given below:

$$\sigma_{LER} = \sqrt{\frac{1}{N}\sum_{i=1}^{N} x_i^2} \tag{3.3}$$

$$\sigma_{LWR} = \sqrt{\frac{1}{N}\sum_{i=1}^{N} (W_i - W)^2} = \sqrt{\frac{1}{N}\sum_{i=1}^{N} w_i^2} \tag{3.4}$$

Where N is the number of measurement points on a line edge, and $N = \frac{L}{d}$ (L is the sampling length, d is the sampling interval),

x_i is the distance from the point on the line edge to its median line.

W_i is the real width of a grating line on a specific measurement point, and $W_i = X_{li} - X_{ri}$,

X_{li} and X_{ri} are the positions of the left and right points on the line edge,

W is the average width of the grating line, $W = \sum W_i / N$,

w_i is the residual error of the grating line width, $w_i = W_i - W$.

3.2.2.2. HHCF

For autocorrelative line edges, the spatial characteristics of the nanoroughness can be characterized with the roughness exponent α and correlation length ξ. HHCF is employed to calculate these two spatial parameters. It describes quantitatively the correlation between the heights of two positions on the profile, and gives the detailed spatial information on LER/LWR.

The HHCF, $G(r)$, of the line edge sequence x_i at the location is defined as below:

$$G(r = md) = \sqrt{\frac{1}{N-m}\sum_{i=1}^{N-m}\left(x_{i+m} - x_i\right)^2} \tag{3.5}$$

$$N = \frac{L}{d} \tag{3.6}$$

Where r is the distance between the two positions on a line edge, and $r = 0,1,2,...,m$, $m < N$,

N is the number of measurement points on the line edge,

L is the sampling length,

d is the sampling interval.

The autocorrelation function (ACF), $\rho(r)$, of the line edge sequence x_i is given below,

$$\rho(r) = \frac{1}{\sigma^2} \cdot \frac{1}{N-r}\sum_{i=1}^{N-r} x_i x_{i+r} \tag{3.7}$$

The following relationship between $G(r)$ and $\rho(r)$ can be deduced,

$$G^2(r) = 2\sigma^2[1 - \rho(r)] \tag{3.8}$$

Figure 3.2 shows the HHCF curve of a self-affine line edge. It follows, from the definition of *G(r)* that,

$$G(0) = 0, \tag{3.9}$$

$$G(r \to \infty) = \sqrt{2}\sigma \; (r >> \xi), \tag{3.10}$$

$$G(r) \approx r^{\alpha} \; (0 < \alpha < 1, \;\; r < \xi), \tag{3.11}$$

Where σ is the root mean square amplitudes of the profile,

ξ is the correlation length,

α is the roughness exponent.

The correlation length, ξ, describes the range within which the points on a line-edge profile are correlative. It can be demonstrated by,

$$\rho(\xi) = 1/e \tag{3.12}$$

$$G(\xi) = \sqrt{2(1-1/e)}\sigma = 1.125\sigma \tag{3.13}$$

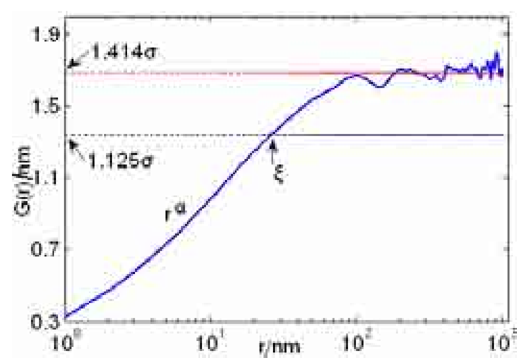

Figure 3.2 - HHCF curve of a line edge profile.

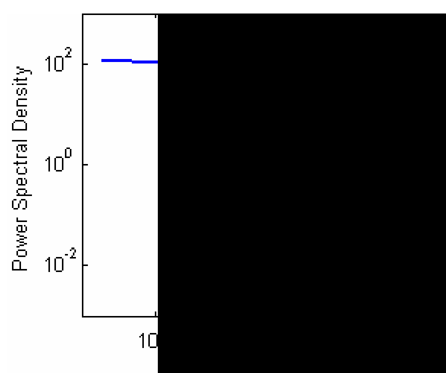

Figure 3.3 - PSD curve of a line edge profile.

The roughness exponent, α, describes the roughness variation in the high frequency domain. The larger the value of α, the less the roughness variation in the high frequency domain, and the smoother the line edge. The smaller the value of α, the more the roughness variation in the high frequency domain, and the rougher the line

edge.

3.2.2.3. PSD

The HHCF describes only the statistical properties of LER/LWR in the spatial domain. In order to characterize the frequency characteristics of LER/LWR, the PSD is used. PSD is employed to decompose the surface profile into its spatial Fourier component wavelengths. For a 1-D line edge profile, the discrete form of PSD is given below:

$$P(f) = \frac{2\Delta}{N}\left|\sum_{i=0}^{N-1} z(i)e^{-2i\pi fj\Delta}\right|^2 \tag{3.14}$$

Where f is the spatial frequency of the roughness,

$z(i)$ is the profile of the line edge,

i is an ordinal number, $i = 0,1,2,...,N-1$,

Δ is the sampling interval,

N is the number of sampling points.

If the measured profile is of a self-affine random rough surface, its ACF is given by:

$$R(r) = \sigma^2 \exp\left(-\frac{|r|\Delta z}{\xi}\right)^{2\alpha} \tag{3.15}$$

Where Δz is the discrete distance between every two neighboring points on the line edge,

σ is the RMS deviation of LER/LWR,

ξ is the correlation length,

α is the roughness exponent.

The approximate PSD form of Eq. 3.15 is given by,

$$P(f) = \frac{2\sigma^2\xi}{\left[1+(f\xi)^2\right]^{a+0.5}} \tag{3.16}$$

Where f is the spatial frequency, $f = i\frac{2\pi}{N\Delta}$ $(0 \le i \le \frac{N}{2})$ and $f_{\min} < f < f_{\max}$,

$f_{\min}$ and $f_{\max}$ are the minimum and maximum values of the spatial frequency,

Figure 3.3 shows the PSD curve produced by Eq.3.16 subject to the conditions that $\sigma = 1.2nm$, $\xi = 25nm$, $\Delta = 1nm$, $\alpha = 0.5$ are met. It can be concluded that when $f > \xi^{-1}$, the PSD of the line-edge profile follows a power law. According to fractal geometry[3.6], the roughness exponent, α, and the slope, b, of the PSD curve are related by,

$$b = -(2\alpha + 1) \qquad (3.17)$$

So the roughness exponent, α, can be derived from the slope, b, of the PSD curve .

3.2.3. Simulation of Self-affine Fractal Curves

The following simulations include self-affine curves and the effects of the parameters of LER/LWR on CD variation of a nanostructure.

3.2.3.1. Simulation of Self-affine Curves

The PSD is frequently employed to simulate the self-affine profiles with specific RMS, correlation length and roughness exponent values [3.7]. Figure 3.4 briefly shows the simulation process.

Suppose the line edges to be generated have 2048 points, and the sampling interval is 1nm. Three examples are given in Figure 3.5. The following conclusion can be drawn: the larger the value of σ, the rougher the line edges. The longer the value of ξ, the slower the change in the line edges. The smaller the value of α, the rougher the line edges.

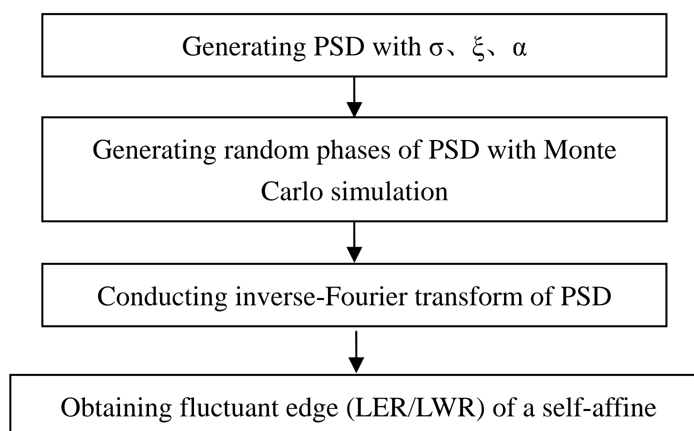

Figure 3.4 - Simulation of a self-affine curve.

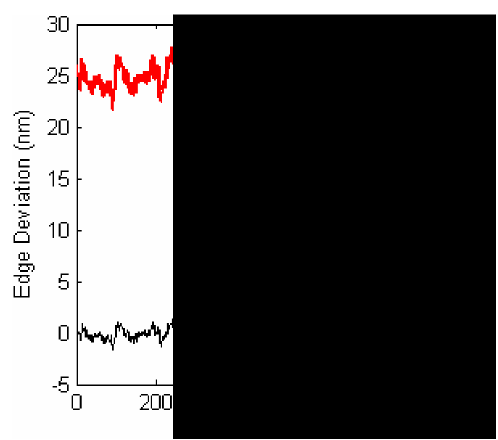

(a) ξ =25nm, α =0.5

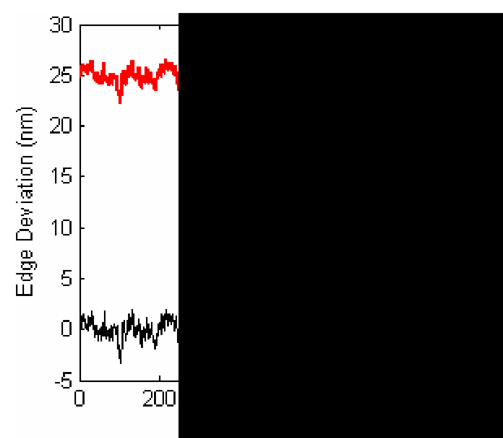

(b) σ =1nm, α =0.5

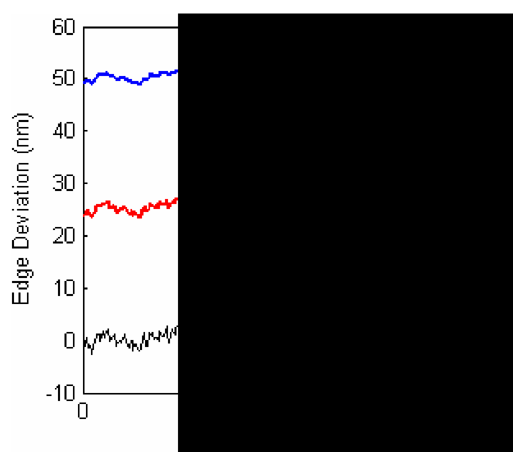

(c) σ =1nm, ξ =25nm

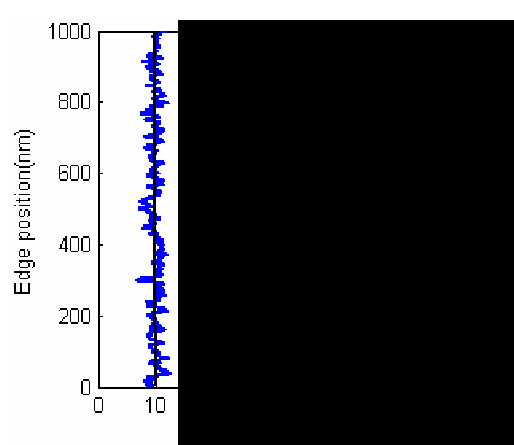

(d) CD=50nm, σ =1nm, α =0.5, ξ =25nm

Figure 3.5 - Simulation of self-affine curves with different σ, ξ and α values.

3.2.3.2. Simulation of the Effect of Parameters on CD Variation

CD variation of a nanostructure means the uniformity of CDs, and has a great effect on the performance of specific nanodevices [3.8]. Suppose M denotes the measurement number within a measurement length where, CD_1, CD_2, ……, CD_M are measured CD values; $\overline{CD}$ is the average value and δ the limit variation. Then

$$\delta = 3\sqrt{\frac{\sum_{i=1}^{M}\left(CD_i - \overline{CD}\right)^2}{M-1}} \tag{3.18}$$

By changing parameters σ, α and ξ of Eq. 3.16, 1000 self-affine line edges were generated, and the parameter effects on CD variation were simulated.

- CD

1000 self-affine line edges with specific RMS σ (1nm), α (0.5) and ξ (25nm) were generated. Figure 3.6 shows the histogram of CD variation. The smaller the CD, the larger the CD variation, as expected.

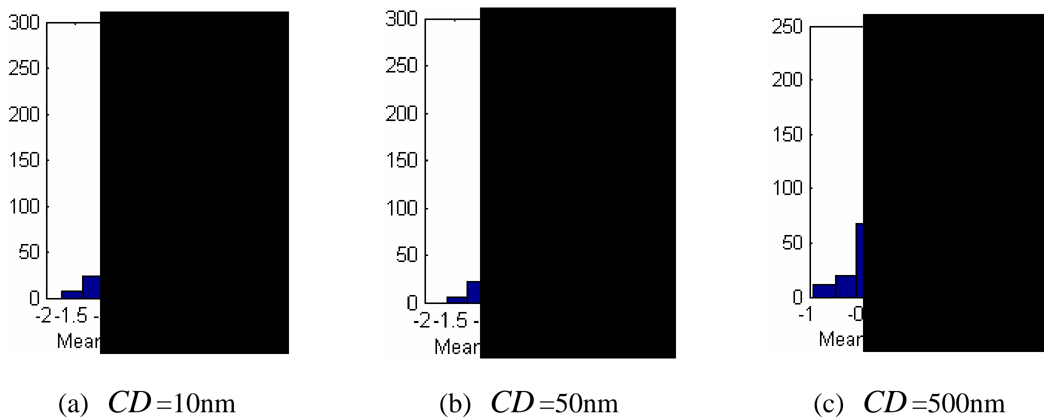

(a) CD=10nm (b) CD=50nm (c) CD=500nm

Figure 3.6 - Histogram of the CD variations with CD values of (a) 10nm, (b) 50nm and (c) 500nm.

- **RMS** σ

RMS σ also affects CD variation greatly. 1000 self-affine line edges with specific α (0.5), ξ (25nm) and RMS σ within the range 0.2nm to 3nm were generated. Figure 3.7 shows the effect of RMS σ on CD variation. The following conclusion can be drawn: the larger the RMS σ, the larger the CD variation; there is an approximate linear relationship between the two. The smaller the CD, the larger the effect of the RMS σ on the CD variation.

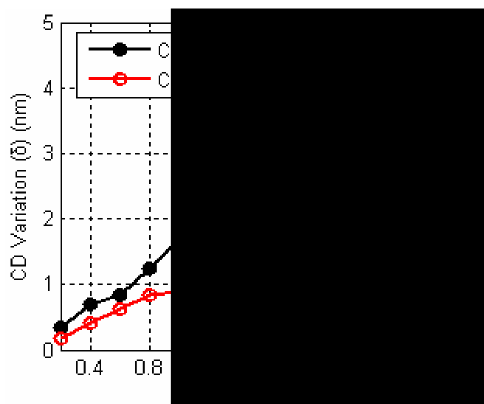

Figure 3.7 – Effect of RMS σ on CD variation.

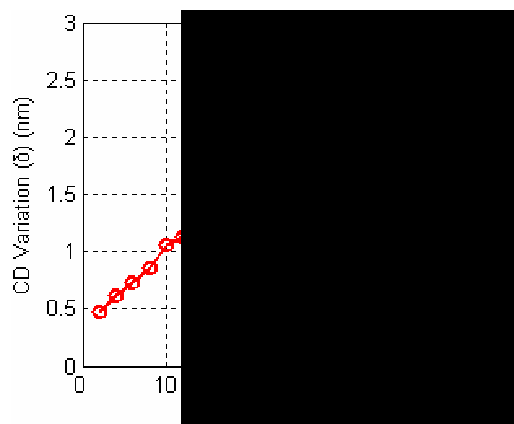

Figure 3.8 - Effect of correlation length ξ on CD variation.

- **Correlation Length** ξ

The correlation length ξ is also one of the main factors which influences CD variation. 1000 self-affine line edges with specific RMS σ (1nm), α (0.5) and ξ within the range 10nm to 30nm were generated. Figure 3.8 shows the effect of correlation length ξ on CD variation. Clearly the longer the correlation length ξ, the larger CD variation. That is, when the correlation length ξ increases from 10nm to 30nm, the corresponding CD variation increases from 1.059nm to 2.147nm.

- **Roughness Exponent** α

The roughness exponent α is another factor which influences CD variation. 1000 self-affine line edges with specific RMS σ (1nm), ξ (25nm), and α within the range from 0.1 to 0.9 were generated, CD values of 25nm and 50nm were used. Figure 3.9 shows the effect of the roughness exponent α on CD variation. With the roughness exponent α within the range 0.1 to 0.25, the larger the roughness exponent α, the smaller the CD variation. With the roughness exponent α within the range from 0.25 to 0.9, a larger roughness exponent α has less effect on CD variation. It is noted that the smaller the CD value, the larger the CD variation.

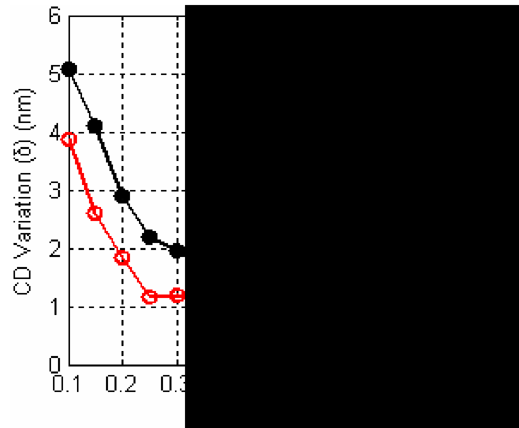

Figure 3.9 – Effect of roughness exponent α on CD variation.

3.3. Characterization and Simulation of 3-D Rough Surfaces

In this section six descriptors are identified to characterize 3-D rough surfaces. The effects of the characteristic parameters on the properties of Gaussian, non-Gaussian and self-affine random rough surfaces are simulated and visualized.

3.3.1. Characterization of 3-D Rough Surfaces

Statistical parameters and functions are identified to characterize 3-D random surfaces, such as RMS deviation S_q, skewness S_{sk}, kurtosis S_{ku}, the autocovariance function,

ACF, and PSD.

3.3.1.1. Root Mean Square S_q

RMS S_q is the RMS value of the height distribution of a rough surface, demonstrating the height distribution in an evaluation area. Its discrete form is given below,

$$S_q = \sqrt{\frac{1}{MN}\sum_{i=1}^{M}\sum_{j}^{N} z^2(x_i, y_j)} \tag{3.19}$$

Where M and N are the numbers of the points in the x and y directions respectively,

$z(x_i, y_j)$ is the height at point (x_i, y_j).

3.3.1.2. Skewness S_{sk}

Skewness S_{sk} is defined as the average of the third power of the heights on a profile,

$$S_{sk} = \frac{1}{S_q^3}\left[\frac{1}{A}\iint_A z^3(x, y)dxdy\right] \tag{3.20}$$

Where S_q is RMS of a surface,

A is the evaluation area,

$z(x, y)$ is the height at point (x, y).

S_{sk} demonstrates the symmetry of a random rough surface within an evaluation area. If the height distribution of a rough surface is symmetric, S_{sk} =0. If the peaks of a surface are deleted, S_{sk} <0. If the valleys of a surface are deleted, S_{sk} >0.

3.3.1.3. Kurtosis S_{ku}

Kurtosis S_{ku} is defined as the average of the fourth power of the heights on a profile,

$$S_{ku} = \frac{1}{S_q^4}\left[\frac{1}{A}\iint_A z^4(x, y)dxdy\right] \tag{3.21}$$

Where S_q is the RMS of a surface,

A is the evaluation area,

$z(x, y)$ is the height at point (x, y).

S_{ku} shows the height distribution of a random rough surface within an evaluation area. For a Gaussian rough surface, S_{ku}=3. If S_{ku}>3, there are more peaks and valleys on the rough surface, and the density probability plot of the surface is sharper than that of a Gaussian rough surface. If S_{ku}<3, there are less peaks and valleys on the rough surface, and the density probability plot of the surface is smoother than that of a Gaussian rough surface.

3.3.1.4. Autocovariance Function and Autocorrelation Function

The autocovariance function and autocorrelation function of a 3-D random rough surface are as below:

$$\rho(\tau_x, \tau_y) = \iint_A z(x, y) z(x + \tau_x, y + \tau_y) dxdy \tag{3.22}$$

$$R(\tau_x, \tau_y) = \frac{\rho(\tau_x, \tau_y)}{\rho(0,0)} = \frac{\iint_A z(x, y) z(x + \tau_x, y + \tau_y) dxdy}{\iint_A z(x, y) z(x, y) dxdy} \tag{3.23}$$

Where τ_x and τ_y are the lags in the x and y directions respectively,

$z(x, y)$ is the height at point (x, y),

A is the evaluation area.

3.3.1.5. PSD

The PSD illustrates the extent to which the texture direction and the wavelength of a rough surface influence RMS σ of 3-D surface roughness.

$$P_s(f_x, f_y) = \lim_{l_x, l_y \to \infty} \frac{1}{4\pi^2} \int_{-l_y}^{l_y} \int_{-l_x}^{l_x} \rho(\tau_x, \tau_y) e^{-j(\tau_x f_x + \tau_y f_y)} d\tau_x d\tau_y \tag{3.24}$$

Where f_x, f_y are the spatial frequencies in x and y directions respectively,

l_x, l_y are the lengths of a 3-D continuous surface in x and y directions respectively,

τ_x and τ_y are the lags in x and y directions respectively.

3.3.1.6. HHCF

The HHCF is equivalent to the ACF, and is defined below:

$$G(\tau_x,\tau_y)=\frac{1}{(l_x-\tau_x)(l_y-\tau_y)}\int_0^{l_x-\tau_x}\int_0^{l_y-\tau_y}\left[z(x,y)-z(x+\tau_x,y+\tau_y)\right]^2 dxdy \qquad (3.25)$$

Where τ_x, τ_y are the correlation lengths in the x and y directions respectively,

l_x, l_y are the lengths of a 3-D continuous surface in the x and y directions respectively,

$z(x,y)$ is the height at point (x,y).

3.3.2. Simulation of 3-D Rough Surfaces

Gaussian, non-Gaussian, complicated and self-affine random rough surfaces were simulated, and the effects of the characteristic parameters on the surface textures were visualized.

3.3.2.1. Simulation of a Gaussian Random Rough Surface

Based on an autoregression model and a 2-D digital lowpass filtration, a specific ACF was generated, thus a Gaussian random rough surface could be simulated [3.9-3.11]. Suppose that an arbitrary random process $\eta(x,y)$ undergoes a 2-D lowpass filter, then a random process $z(x,y)$ is generated as below,

$$z(x,y)=\sum_{k=0}^{n-1}\sum_{k=0}^{m-1}h(\tau_x,\tau_y)\eta(x+\tau_x,y+\tau_y) \qquad (3.26)$$

Where $\tau_x = 1,...,N$, $\tau_y = 1,...,N$,

$n = N/2$, $m = M/2$,

$h(\tau_x, \tau_y)$ is the impact response function of the filter.

The Fourier transformation of Eq. 3.26 is given by

$$Z(\omega_x, \omega_y) = H(\omega_x, \omega_y) \times A(\omega_x, \omega_y) \quad (3.27)$$

Where $Z(\omega_x, \omega_y)$, $H(\omega_x, \omega_y)$ and $A(\omega_x, \omega_y)$ are Fourier transforms of $z(x, y)$, $h(\tau_x, \tau_y)$ and $\eta(x, y)$ respectively

$\omega_x = e^{j\omega x}$, $\omega_y = e^{j\omega y}$.

Suppose $P_\eta(\omega_x, \omega_y)$ is defined as the PSD of the input sequence, then PSDs of input and output sequences $P_\eta(\omega_x, \omega_y)$ and $G(\omega_x, \omega_y)$ follow the following relationship,

$$G(\omega_x, \omega_y) = \left| H(\omega_x, \omega_y) \right|^2 P_\eta(\omega_x, \omega_y) \quad (3.28)$$

Since the input sequence is made up of independent random sequences, following a Gaussian distribution, its PSD $P_\eta(\omega_x, \omega_y)$ can be regarded as a constant C , then

$$H(\omega_x, \omega_y) = (G(\omega_x, \omega_y) / C)^{1/2} \quad (3.29)$$

According to above analysis, the simulation steps for a Gaussian rough surface with a specific ACF are summarised as follows. A random sequence $\eta(x, y)$ of a 2-D random surface was generated and its Fourier transform $P(\omega_x, \omega_y)$ was determined. The PSD $G(\omega_x, \omega_y)$ of the output sequence was calculated from the Fourier transform of a specific ACF $R_z(\tau_x, \tau_y)$, and its constant C was determined. According to Eq.3.29 the transfer function $H(\omega_x, \omega_y)$ of the filter was obtained. According to Eq.(3.27) the Fourier transform $Z(\omega_x, \omega_y)$ of the output sequence was calculated. Finally the height distribution function $z(x, y)$ of the random surface was

obtained from the inverse Fourier transform $Z(\omega_x, \omega_y)$.

1) Exponential ACF

An exponential ACF is frequently employed to establish an ACF model of a rough surface [3.12]. It can be expressed as:

$$R(\tau_x, \tau_y) = \sigma^2 \exp\left(-2.3\left(\left(\frac{\tau_x}{\beta_x}\right)^2 + \left(\frac{\tau_y}{\beta_y}\right)^2\right)^{\frac{1}{2}}\right) \tag{3.30}$$

Where σ is RMS roughness,

β_x and β_y are correlation lengths in x and y directions, respectively,

τ_x and τ_y are lags between two positions in x and y directions, respectively.

If β_x is equal to β_y, the surface is isotropic. Otherwise the surface is anisotropic. The simulation surfaces all were 128nm×128nm. Figure 3.10 shows the simulated 3-D profiles of rough isotropic surfaces with exponential ACFs: the shorter the correlation length, the rougher the surface.

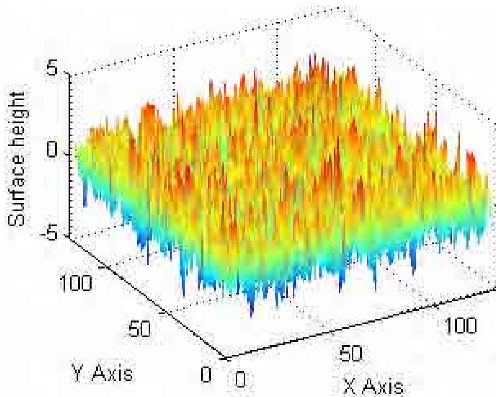

(a) $\beta_x = \beta_y$ =5nm, σ =1nm.

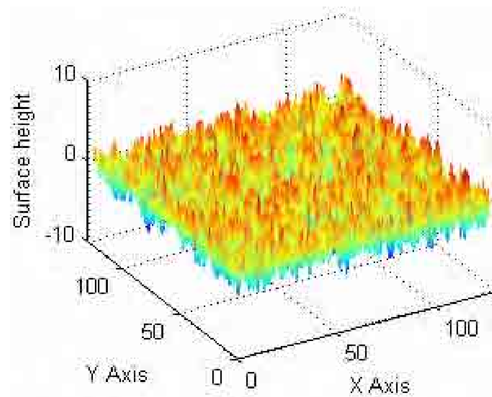

(b) $\beta_x = \beta_y$ =10nm, σ =1nm.

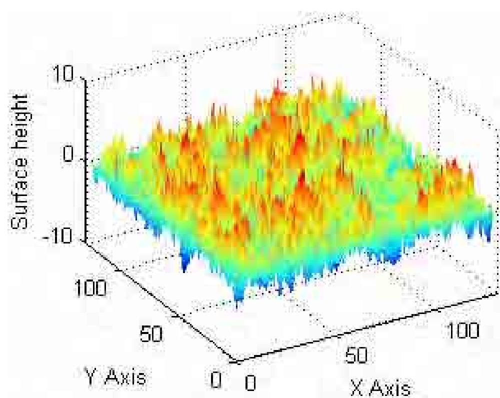

(c) $\beta_x = \beta_y$ =25nm, σ =1nm.

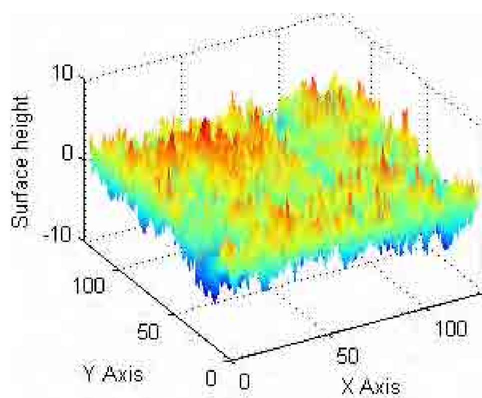

(d) $\beta_x = \beta_y$ =50nm, σ =1nm.

Figure 3.10 – The simulated 3-D profiles of a rough isotropic surfaces with exponential ACFs.

In order to simulate the anisotropic surface parameter $\nu = \beta_x / \beta_y$ was employed. Figure 3.11 shows the simulated 3-D profiles of rough anisotropic surfaces with exponential ACF and different ν values. Clearly when ν is larger than 1, the surface has lateral texture, and the larger the parameter ν, the more distinct the texture. When ν is less than 1, the surface has longitudinal texture, and the larger the parameter ν, the more distinct the texture. Figure 3.12 shows the comparison of exponential ACFs of isotropic and anisotropic surfaces.

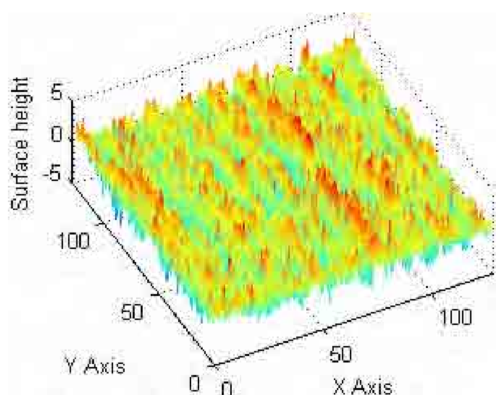

(a) β_x =500nm, β_y =5nm, σ =1nm.

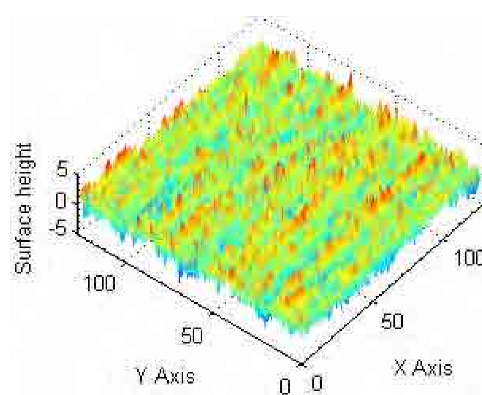

(b) β_x =5nm, β_y =500nm, σ =1nm.

Figure 3.11 – The simulated 3-D profiles of anisotropic surface with an exponential ACF and different ν values.

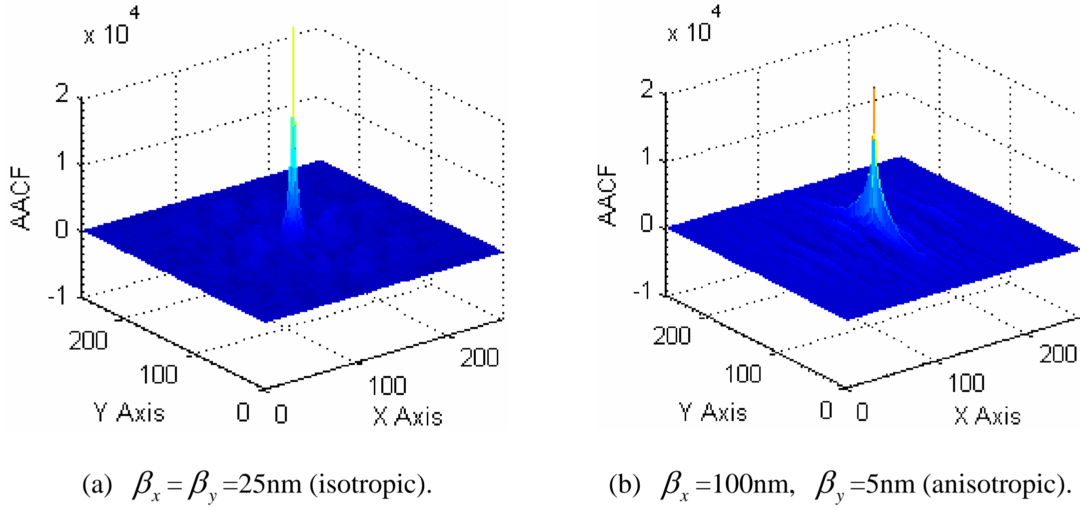

(a) $\beta_x = \beta_y$ =25nm (isotropic). (b) β_x =100nm, β_y =5nm (anisotropic).

Figure 3.12 – Comparison of exponential ACFs of isotropic and anisotropic surfaces.

2) Cosine-exponential ACF

In some circumstances the rough surfaces are modeled by cosine-exponential ACF. The expression for a cosine-exponential ACF is shown below:

$$R(\tau_x, \tau_y) = \sigma^2 \exp\left(-2.3\left|\tau_x / \beta_x\right|\right) \frac{\cos\left(\tau_y / \beta_y\right)}{\tau_y / \beta_y} \tag{3.31}$$

Where σ is RMS roughness,

β_x and β_y are correlation lengths in x and y directions respectively,

τ_x and τ_y are lags of two positions in the x and y directions respectively.

Figure 3.13 shows the simulated 3-D profiles of rough isotropic surfaces (128nm×128nm) with cosine-exponential ACFs, RMS σ (1nm), and $\beta_x = \beta_y$ (5nm, 10nm, 25nm and 50nm respectively). The surface texture in the y direction demonstrates a monotonic decrease, while that in the x direction exhibits a periodic oscillation. Correlation lengths influence the texture of the surface, the longer the

correlation lengths, the rougher the amplitude of the surface.

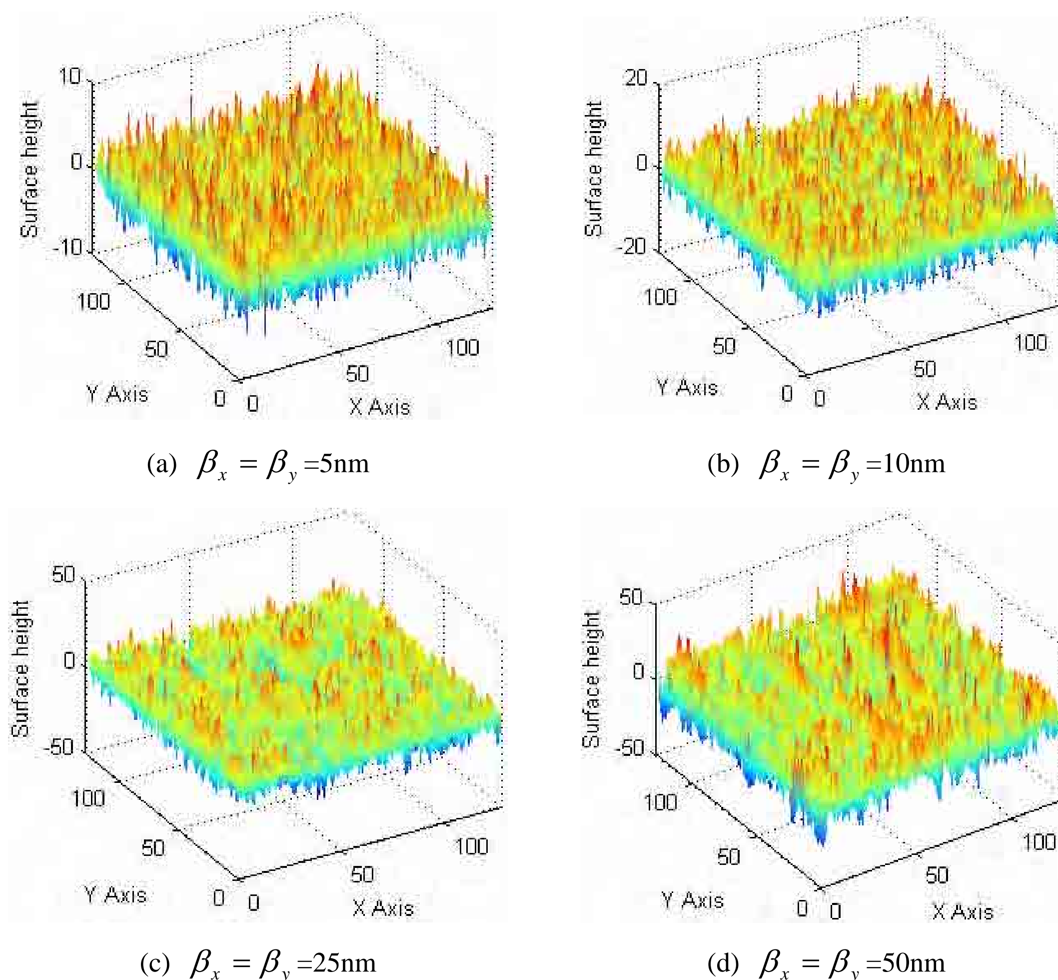

(a) $\beta_x = \beta_y$ =5nm (b) $\beta_x = \beta_y$ =10nm

(c) $\beta_x = \beta_y$ =25nm (d) $\beta_x = \beta_y$ =50nm

Figure 3.13 – The simulated 3-D profiles of isotropic surfaces with cosine-exponential ACF.

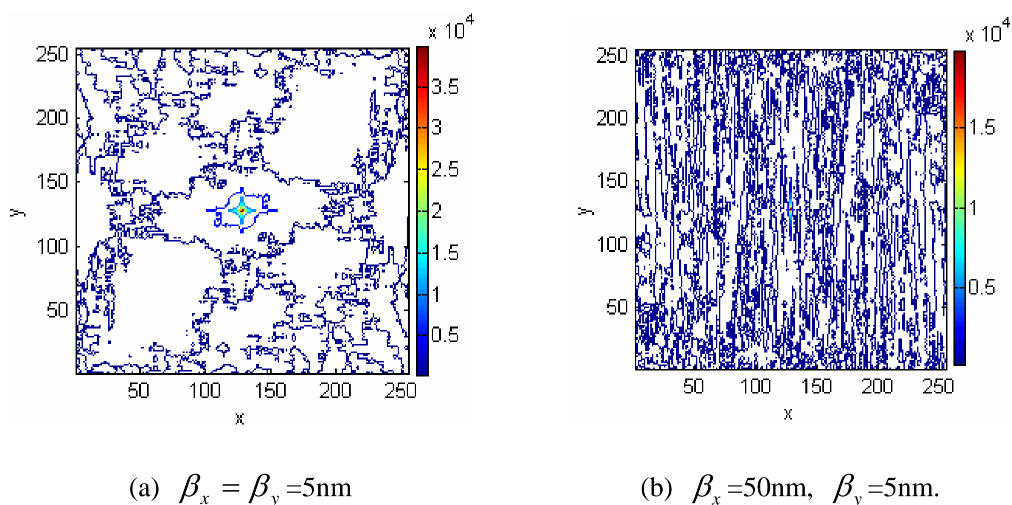

(a) $\beta_x = \beta_y$ =5nm (b) β_x =50nm, β_y =5nm.

Figure 3.14 – Contour maps of exponential ACFs of a rough surface.

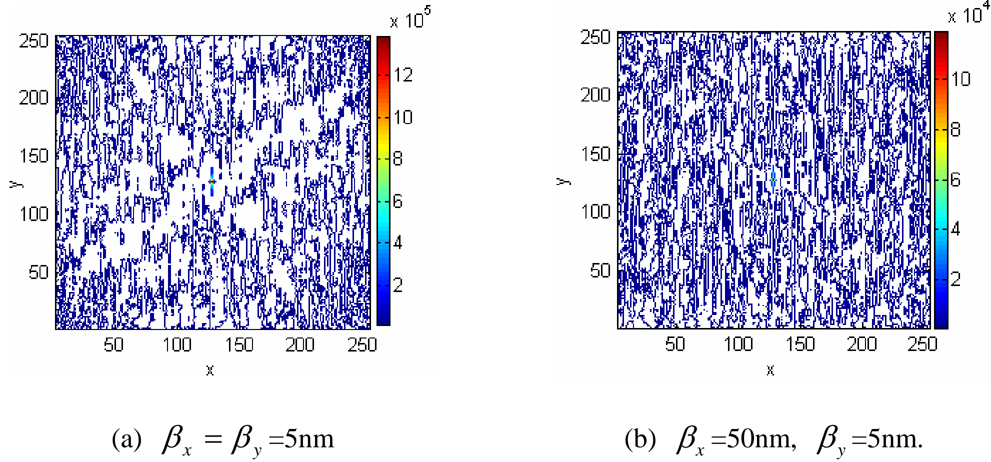

(a) $\beta_x = \beta_y$ =5nm (b) β_x =50nm, β_y =5nm.

Figure 3.15 – Contour maps of cosine-exponential ACFs of a rough surface.

Figure 3.14 and Figure 3.15 show the contour maps of exponential and cosine-exponential ACFs of rough surfaces respectively. The comparison of both figures shows that the surface texture with a cosine-exponential ACF is more complicated than that with an exponential ACF, and the periodic and fluctuating characteristics of the surface texture with a cosine-exponential ACF are more obvious that that with an exponential ACF.

3.3.2.2. Complicated Rough Surface

Any complex random process can be expressed as the summation of two simple uncorrelated processes, that is a periodic one and a random one. Suppose a complex rough surface is made up of exponential and cosine ACFs,

$$\begin{cases} R(\tau_x,\tau_y) = \sigma^2 \exp\left(-2.3\left(\left(\tau_x / \beta_x \right)^2 + \left(\tau_y / \beta_y \right)^2 \right)^{\frac{1}{2}} \right) \\ R(\tau_x,\tau_y) = \sigma^2 \dfrac{\cos(\tau_y / \beta_y)}{\tau_y / \beta_y} \end{cases} \tag{3.32}$$

Where σ is RMS roughness,

β_x and β_y are correlation lengths in x and y directions respectively,

τ_x and τ_y are lags in the x and y directions respectively.

Figure 3.16 shows the simulated complex rough surfaces and the contour maps of the combined ACF calculated from Eq. 3.32. Obviously the combined rough surface texture in Figure 3.16(a) has periodic as well as exponential components.

Other complicated rough surfaces can be combined with ACFs as well as the ones mentioned above[3.13].

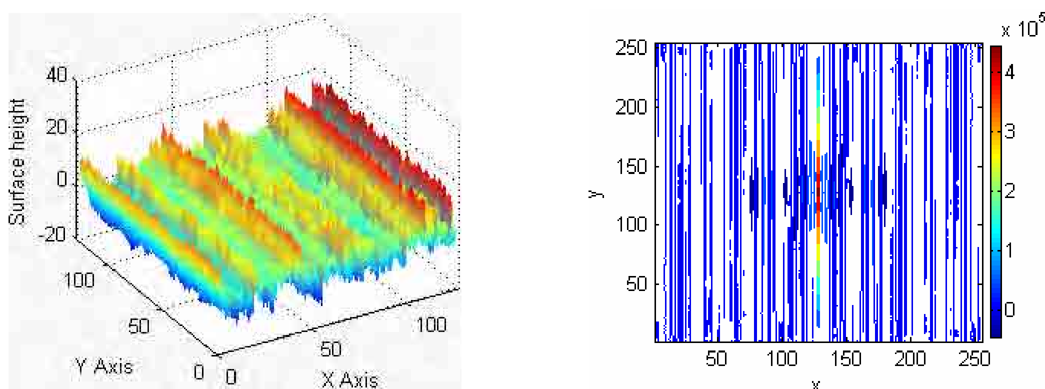

(a) Surface with the combination of exponential and cosine ACFs.

(b) Contour map of the combined ACF in (a).

Figure 3.16 – Simulated complex rough surface and the contour map of the combined ACFs.

3.3.2.3. Simulation of Non-Gaussian Random Rough Surface

Non-Gaussian rough surfaces often have negative skewnesses. The following simulations are based on the assumption that a Gaussian random sequence can be transformed into a non-Gaussian sequence by a Johnson transform [3.14], while its correlation function does not change by very much. Hu [3.15] and Peng [3.16] proposed that when a random sequence is filtered by a digital filter, its skewness and kurtosis may change slightly. So it is necessary to correct the skewness and kurtosis after filtering.

Suppose that the skewness and the kurtosis of an input random sequence are Sk_η and Sku_η respectively, then those of the output random sequence are Sk_z and Sku_z after Johnson transform are as below [3.17]

$$Sk_z = \frac{\sum_{k=0}^{N-1}\sum_{l=0}^{M-1} h(k,l)^3}{\left(\sum_{k=0}^{N-1}\sum_{l=0}^{M-1} h(k,l)^2\right)^{3/2}} Sk_\eta \qquad (3.33)$$

$$Sku_z = \frac{\sum_{k=0}^{N-1}\sum_{l=0}^{M-1} h(k,l)^4}{\left(\sum_{k=0}^{N-1}\sum_{l=0}^{M-1} h(k,l)^2\right)^{2}} (Sku_\eta - 3) + 3 \qquad (3.34)$$

Where Sk_η and Sk_z are skewnesses of the input and output random sequences,

Sku_η and Sku_z are the kurtosis of the input and output random sequences,

$h(k,l)$ is the impact response function of the filter.

Detailed simulation flow of a non-Gaussian random rough surface is summarized as follows. Skewness and kurtosis were set for the rough surface to be generated. The skewness Sk_η and kurtosis Sku_η of the input random sequence were calculated from Eq. 3.20 and Eq. 3.21. A discrete Gaussian random sequence $\eta(x,y)$ was generated with a random number generator. Using a Johnson tranform a non-Gaussian random sequence $\eta'(x,y)$ with given skewness and kurtosis was generated from a Gaussian random sequence $\eta(x,y)$ from Eq. 3.33 and Eq. 3.34. The transfer function $H(\omega_x, \omega_y)$ of the filter was obtained. And finally the height distribution function $z(x,y)$ of the surface with a lowpass filter was found. The following non-Gaussian random rough surfaces with exponential ACF were simulated.

1) Surfaces with negative skewness

Figure 3.17 exhibits simulated rough surfaces with different negative skewness values as well as corresponding 2-D profiles. It can be concluded that the surface texture with skewness S_{sk} (-1.0) is sharper than that with skewness S_{sk} (-0.3), and especially that it has deeper valleys.

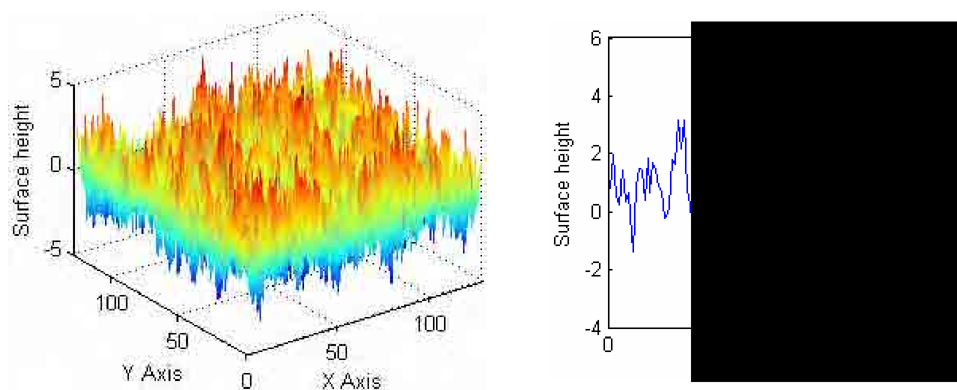

(a) $\beta_x = \beta_y$ =25nm， S_{ku} =5， S_{sk} =-0.3.

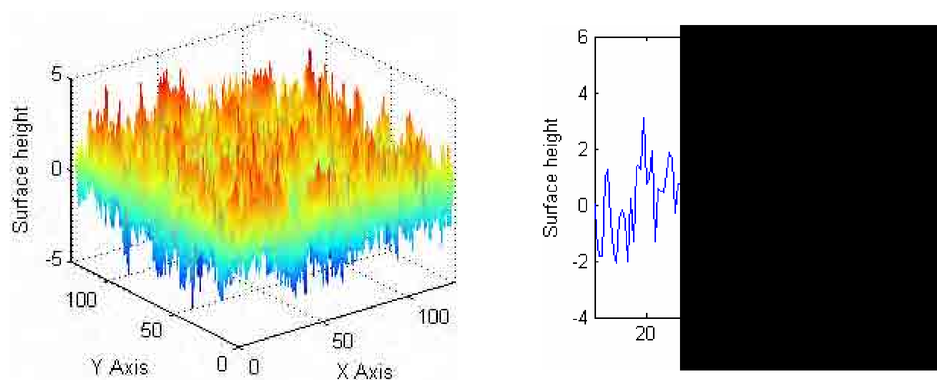

(b) $\beta_x = \beta_y$ =25nm， S_{ku} =5， S_{sk} =-1.

Figure 3.17 – Simulation of non-Gaussian rough surfaces with different negative skewness.

2) Surfaces with different positive skewness

Figure 3.18 shows rough surfaces with different positive skewness values as well as corresponding 2-D profiles. The larger the skewness, the more and sharper the high peaks, while the less the skewness, the more flat the low valleys. Comparing Figure 3.18 with Figure 3.17, one can conclude that when the skewness is less than zero, the

peaks are rather flat and the valleys sharper. On the other hand, when the skewness is greater than zero, the peaks are sharper and the valleys flatter. The same conclusion can be reached from the definition of skewness in Eq. 3.20.

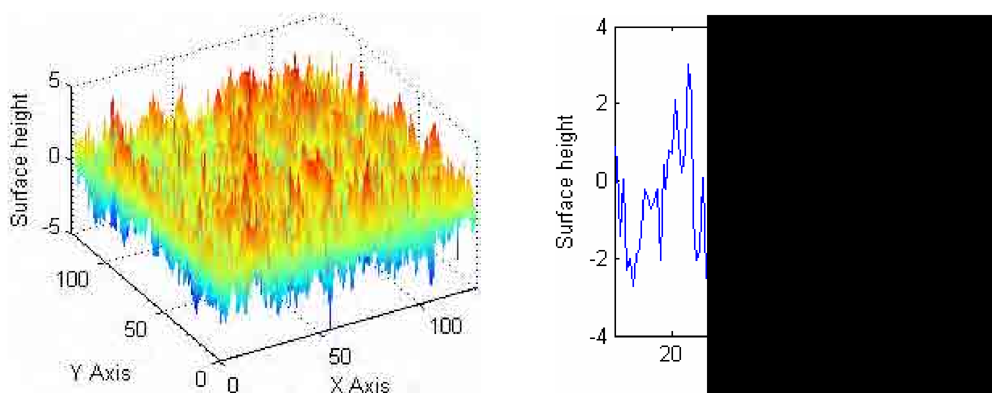

(a) $\beta_x = \beta_y$ =25nm, S_{ku} =3, S_{sk} =0.3.

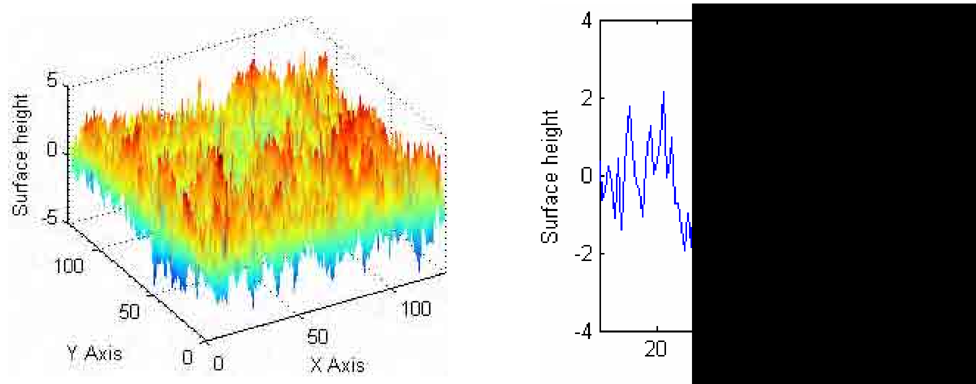

(b) $\beta_x = \beta_y$ =25nm, S_{ku} =3, S_{sk} =1.

Figure 3.18 – Simulation of rough surfaces with different positive skewnesses.

3) Surfaces with different kurtosis (and negative skewness)

Figure 3.19 shows the simulations of rough surfaces with different kurtosis values as well as corresponding 2-D profiles. It can be concluded that more high peaks and low valleys are produced in the surface texture with kurtosis S_{ku} larger than 3. Conversely, less high peaks and low valleys are formed in the surface texture with

kurtosis S_{ku} less than 3.

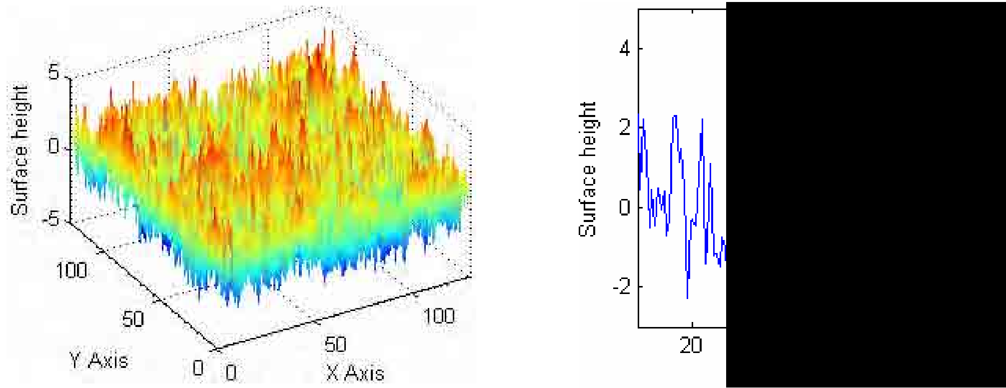

(a) $\beta_x = \beta_y$ =25nm， S_{ku} =2， S_{sk} =-0.3.

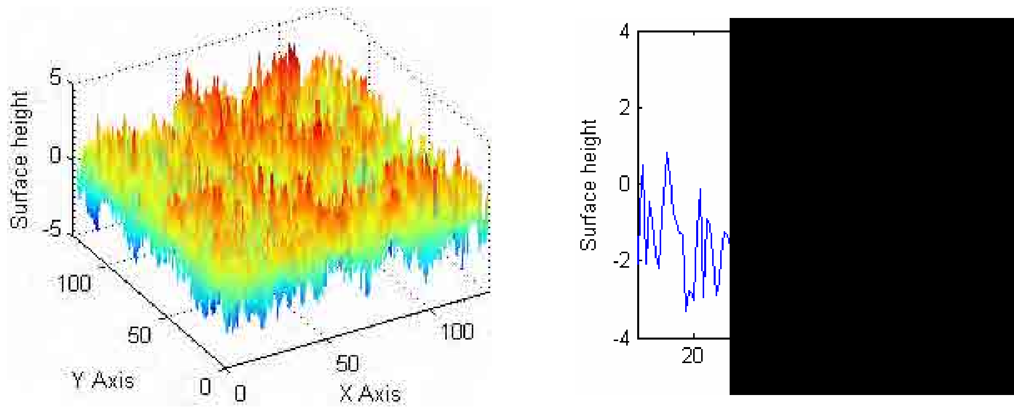

(b) $\beta_x = \beta_y$ =25nm， S_{ku} =5， S_{sk} =-0.3.

Figure 3.19 – Simulation of rough surfaces with different kurtosises.

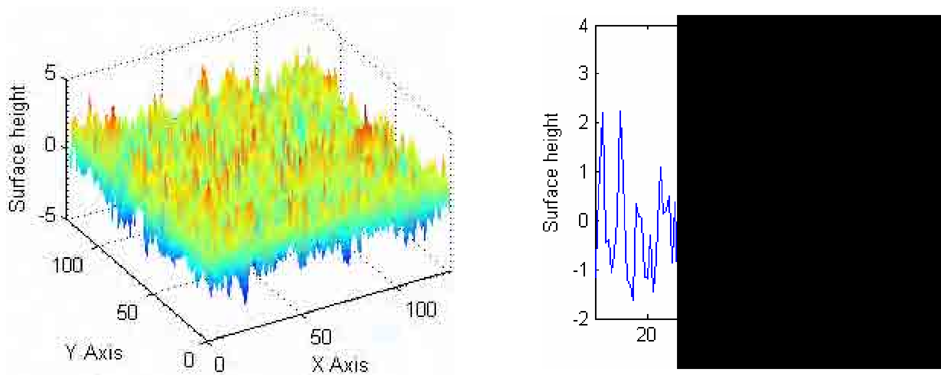

(a) $\beta_x = \beta_y$ =10nm， S_{ku} =3， S_{sk} =-0.3.

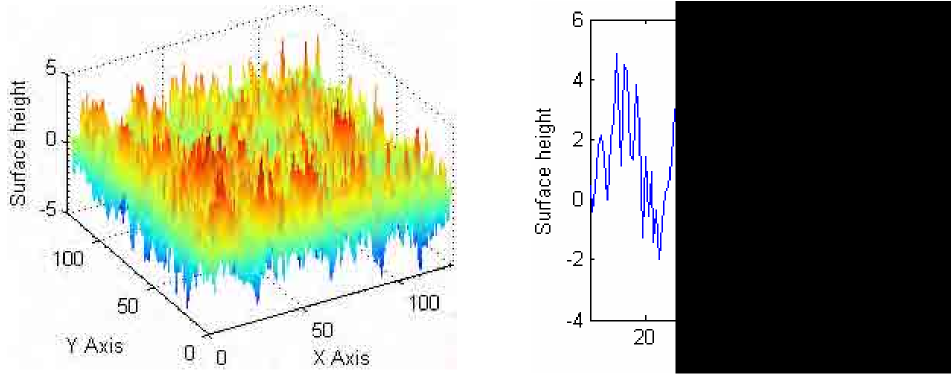

(b) $\beta_x = \beta_y$ =50nm， S_{ku}=3， S_{sk}=-0.3.

Figure 3.20 – Simulation of rough surfaces with different correlation lengths.

4) Surfaces with different correlation lengths

Figure 3.20 shows the simulation of rough surfaces with different correlation lengths as well as corresponding 2-D profiles. One can conclude that as correlation lengths β_x and β_y increase, the rough surface texture become sharper, and the number of peaks and valleys becomes less.

3.3.2.4. Simulation of a Self-affine Rough Surface

According to the conclusion obtained by Goff and Jordan [3.18], a self-affine rough surface is described by the following PSD function,

$$P(f_x, f_y) = \frac{2\alpha\beta_x\beta_y\sigma^2}{\left(1 + f_x^2\beta_x^2 + f_y^2\beta_y^2\right)^{(1+\alpha)}} \tag{3.35}$$

Where σ is RMS deviation,

β_x, β_y are correlation lengths in the x and y directions respectively,

α is the roughness exponent,

f_x, f_y are spatial frequencies in the x and y directions respectively.

The correlation function and HHCF of a self-affine rough surface are deduced from Eq.3.36 and Eq.3.37 respectively,

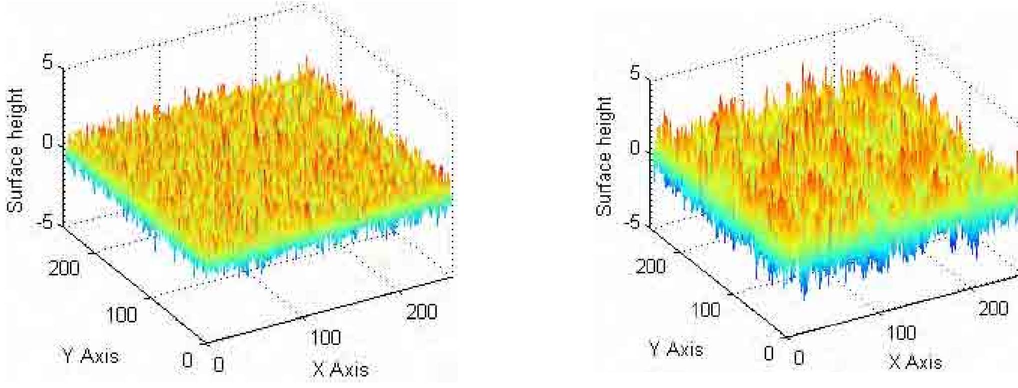

(a) $\beta_x = \beta_y$ =5nm, α =0.5, and σ =1nm. (b) $\beta_x = \beta_y$ =25nm, α =0.5, and σ =1nm.

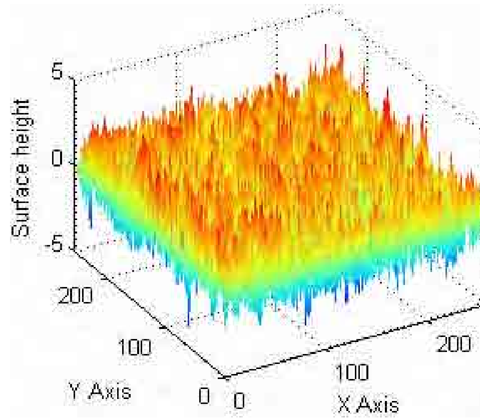

(c) $\beta_x = \beta_y$ = 25nm, α =0.8, and σ =1nm.

Figure 3.21 –Simulations of self-affine rough surfaces.

$$R(\tau_x, \tau_y) = \frac{1}{2^{\alpha-1}\Gamma(\alpha)}\left(\frac{\tau_x^2}{\beta_x^2} + \frac{\tau_y^2}{\beta_y^2}\right)^{\alpha/2} K_\alpha\left[\left(\frac{\tau_x^2}{\beta_x^2} + \frac{\tau_y^2}{\beta_y^2}\right)^{1/2}\right] \tag{3.36}$$

$$G(\tau_x, \tau_y) = 2\sigma^2\left\{1 - \frac{1}{2^{\alpha-1}\Gamma(\alpha)}\left(\frac{\tau_x^2}{\beta_x^2} + \frac{\tau_y^2}{\beta_y^2}\right)^{\alpha/2} K_\alpha\left[\left(\frac{\tau_x^2}{\beta_x^2} + \frac{\tau_y^2}{\beta_y^2}\right)^{1/2}\right]\right\} \tag{3.37}$$

Where σ is the roughness RMS,

α is the roughness exponent,

K_α is a modified Bessel function of the α th order [3.19],

$\Gamma(x)$ is a Gamma function,

β_x, β_y are correlation lengths in the x and y directions respectively,

τ_x and τ_y are lags between two positions in the x and y directions respectively.

Figure 3.21 shows the generated self-affine surfaces with different correlation lengths β_x and β_y, roughness exponent and RMS σ. The numbers of points in the x and y directions on the surface to be simulated were all 256. As expected, in Figure 3.21(a) and (b), the shorter the correlation lengths, the more compact the surface texture and the less fluctuating the amplitude of the rough surface. With regard to Figure 3.21 (b) and (c), the smaller the roughness exponent α, the more irregular structures in the rough surface. The same conclusion was obtained in Section 3.2.

3.4. Summary

In this Chapter, three descriptors for the characterization of random rough curves are identified: RMS σ, HHCF and PSD. Self-affine curves with different RMS σ, correlation length ξ and roughness exponent α were simulated and visualized. The effect of LER/LWR parameters on CD variation were visualized, including CD, RMS σ, correlation length ξ and roughness exponent α, etc.

For the characterization of 3-D rough surfaces six descriptors were identified: RMS S_q, skewness S_{sk}, kurtosis S_{ku}, the autocovariance function, ACF, PSD and HHCF. Gaussian and non-Gaussian random rough surfaces and self-affine rough surfaces with specific characeristic parameters were investigated and simulated. For a Gaussian random rough surface, the surface textures with exponential, cosine-exponential and complex ACFs were simulated, including visualization with contour maps. With regard to the simulatiom of non-Gaussian random surfaces,

surfaces with negative and positive skewnesses S_{sk}, different kurtosis S_{ku} plus negative skewness S_{sk} and different correlation lengths were simulated and visualized. HHCFs for self-affine random rough surfaces were simulated. These conclusions are necessary for the characterization of nanoroughness in relevant sections of Chapters 4 and 5.

CHAPTER 4

FABRICATION AND NANOROUGHNESS CHARACTERIZATION OF NANOLINEWIDTH AND NANOPITCH SPECIMENS

4.1. Introduction

One aspect of nanometrology research is fabrication of relevant specimens, for example, nanolinewidth and nanopitch specimens[4.1, 4.2]. Various techniques are frequently employed to fabricate nanolinewidth and nanopitch specimens in order to measure specific nanoscale parameters and to calibrate different nanoscale instruments. The difficulties in acquiring quality nanolinewidth and nanopitch specimens cab be summarised as listed here. (a) Nominal sizes of nanolinewidth and nanopitch specimens are more than 10nm; the small size rules out many fabrication processes. (b) The uniformity of grating lines of the specimens needs to be further improved. (c) The lengths of the specimens need to be increased[4.2]. In order to overcome the above mentioned drawbacks, in this chapter the molecular beam epitaxy

(MBE) process is introduced. The materials were selected carefully to fabricate nanolinewidth and nanopitch specimens with nominal sizes less than 10nm. Upon completion of the fabrication, high resolution transmission electron microscopy (HRTEM) was employed to measure the specimens, and the fabrication process uncertainty was evaluated in order that the process parameters could be further regulated.

In the following sections, first several fabrication techniques are compared and the MBE-based fabrication process is introduced. Then the chapter will proceed to MBE-based fabrication of nanolinewidth and nanopitch specimens, including the design of the nanolinewidth and nanopitch specimens, the material selection and parameter regulation of the fabrication process. The fabricated nanostructures will be measured with HRTEM and the LER/LWR of grating line edges will be characterized in detail, including filtering of HRTEM images, extraction, association and characterization of line edge profiles from the filtered HRTEM images. Following this, the results of the fabrication and characterization will be discussed.

4.2. A Brief Introduction to Fabrication of Nanolinewidth and Nanopitch Specimens

Fabrication and characterization of nanolinewidth and nanopitch specimens are playing more and more important roles in nanometrology[4.3]. The following three groups of ways are currently employed in providing high quality nanospecimens, including traditional fabrication techniques (such as optical, electron beam, ion beam and x-ray lithography, etc.), the intrinsic crystal lattice constant of some crystalline

materials being used as a natural specimen, and laser focused atomic deposition techniques.

Traditional fabrication techniques make it difficult to fabricate patterns with a nominal size less than 10nm and the cost is very high. Laser focused atomic deposition technique is good but it is difficult to fabricate the expected patterns, especially those with nominal size less than 10nm. For the specimens that use the constants of crystalline materials as the nominal size, these constants are intrinsic and cannot be modified easily to comply with the expected nominal size of the specimen. It is believed that the MBE-based process is a promising technique which can be employed to fabricate expected nanolinewidth and nanopitch specimens effectively. So in the following sections, the MBE-based fabrication and HRTEM-based characterization of nanolinewidth and nanopitch specimen will be discussed in detail.

4.3. MBE-based Fabrication of Nanolinewidth and Nanopitch Specimens

More precision planar lithography processes are needed to fabricate patterns with even smaller critical dimensions, such as electron beam lithgraphy (EBL), X-ray lithography and ion beam lithography. The shortcoming of these processes is the high cost. In comparison, film deposition techniques can be used to fabricate multiple layer films with small thicknesses. So the main method of fabricating nanolinewidth and nanopitch introduced in this chapter is to take the thicknesses of multilayers which are deposited alternately on a specific substrate as the linewidthes or pitches of a nanolinewidth or nanopitch specimen.

4.3.1. Background on the MBE process

Nowadays there are many film deposition processes in the IC industry and nanotechnology research institutions, such as metal-organic chemical vapor deposition (MOCVD), magnetron sputtering, vacuum evaporation as well as MBE, etc[4.4-4.7]. Of all these processes, it is difficult for first three methods to fabricate high quality nanostructures with CD less than 10nm. In contrast, the MBE process is very promising for the fabrication of heterojunction structures which have not only attractive properties, but also small critical dimensions[4.8]. So it is possible to employ MBE process to fabricate nanopatterens with CD less than 10nm.

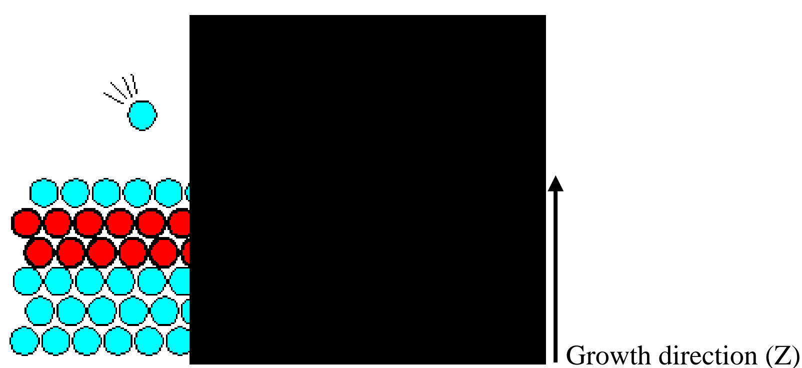

Figure 4.1- Schematic diagram of MBE process [4.9].

MBE is a new technology for growing high quality crystal films on a crystalline substrate. In a high vaccum chamber, various solid components of the expected crystal are heated in different cells to produce a vapour, forming molecule or atom beams after collimation by small apertures. The collimated molecule or atom beams are deposited directly, in a raster scanning mode, onto a single crystal substrate which is heated to the required temperature,. Films are formed layer by layer according to the alignment of the crystal. Figure 4.1 shows the diagram of depositing atoms or

molecules one by one on a substrate using MBE[4.9].

MBE has been used to fabricate monocrystal films which have only several dozens of atomic layers. With components and dopings changed alternately, ultrathin quantum wells also can be fabricated by the MBE process. The distinguishing features of MBE are listed below[4.9].

- The temperature for epitaxial growth is low (600℃-700℃), hence the effects of lattice mismatch caused by the thermal expansion on the interface and self-doped diffusion of impurities on the epitaxial layer are significantly decreased.
- Film growth rate is very slow (about 1μm/hour), enabling one to accurately control the beam intensity, the thickness, the structure, the components and the heterojunction. Actually it is an atom-scale fabrication technique and very suitable for the growth of supperlatice materials.
- Components of the crystal film and doping density can be promptly adjusted.
- Since the MBE process is performed in an ultra-high vacuum chamber, the substrate surface can be cleaned thoroughly and contamination during the epitaxy process can be effectively avoided, so high quality epitaxial layers can be fabricated. Moreover there are other instruments within the MBE high vacuum chamber which are employed to detect the surface structure, the components and the residual gas, so on-line monitoring of the composition and structural integrality of epitaxial layers can easily be conducted.
- MBE is a dynamic process, not a thermodynamic one. Neutral particles (such as atoms and molecules) are piled up one by one on a substrate to form the expected

films. So it can deposit films which cannot be grown by ordinary thermal equilibrium processes.

- MBE is a physical deposition process within an ultrahigh vacuum chamber, so the effects of chemical reactions during intermediate process and mass transfer need not to be taken into consideration. Besides these, the shutters in MBE system can be used to turn on or off the growth, so the components and doping density of epitaxial films can be quickly adjusted according to the changes of sources.

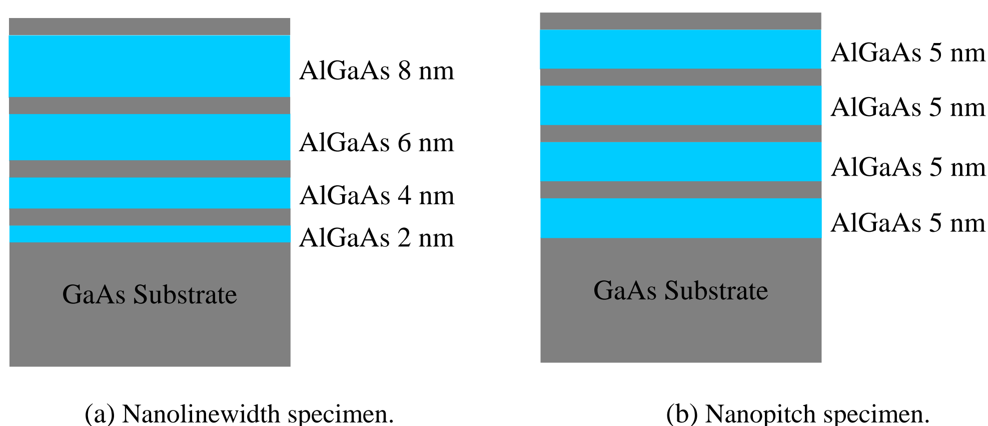

(a) Nanolinewidth specimen. (b) Nanopitch specimen.

Figure 4.2 - Diagrams of nanoscale specimens to be fabricated with MBE process and their materials selection.

4.3.2. MBE-based Design of Nanolinewidth and Nanopitch Specimens

The MBE process is to be employed for fabrication of nanolinewidth and nanopitch specimens. The materials such as chrome and silicon nitride in previous work are to be replaced by GaAs and AlGaAs. Figure 4.2 shows diagrams of the nanolinewidth and nanopitch specimens to be fabricated. For the nanolinewidth specimen, GaAs substrate is used and the thicknesses of deposited AlGaAs layers(here are 2nm, 4nm, 6nm, 8nm, etc.) are regarded as the nominal linewidthes of the nanolinewidth specimen, as shown in Figure 4.2(a). With regard to nanopitch specimens, the same

substrate is employed as for nanolinewidth specimens. Also the thicknesses of deposited AlGaAs layers are regarded as the nominal pitch (here 5nm) of the nanopitch specimen, see Figure 4.2(b).

4.3.3. Material Selection for MBE-based Fabrication of Nanolinewidth and Nanopitch Specimens

Materials selection has a great effect on the quality of nanolinewidth and nanopitch specimens fabricated with MBE process. Silicon-based materials are often chosen as a substrate. But it is necessary to look for new semiconductor materials to meet other application requirements. Two kinds of parameters need to be taken into consideration for material selection[4.10]: image contrast as well as the mismatch ratio between the epitaxy material and substrate material. Regarding the mismatch ratio, GaAs and AlGaAs have almost the same lattice constant, and the following two equations are widely used to calculate the mismatch ratio δ [4.11].

$$\delta = \frac{a_s - a_e}{a_s} \tag{4.1}$$

$$\delta' = \frac{2 / a_s - a_e /}{a_s + a_e} \tag{4.2}$$

Where a_s is the lattice constant of a substrate,

a_e is the lattice constant of an epitaxied material.

Table 4.1 shows that the mismatch ratio between GaAs and AlGaAs is significantly less than 5%, demonstrating the materials are appropriate for the MBE fabrication process. But there is another point that needs to be considered — image contrast. In this chapter HRTEM will be employed to characterize the fabricated nanostructures.

For HRTEM, two kinds of image contrast should be considered: diffraction contrast and phase contrast. Diffraction contrast means the variations in intensity of diffraction across the sample, while phase contrast the phase variations of the electron wave caused by the Coulomb field of atomic nucleus and outer shell electrons in the sample[4.12]. In this chapter GaAs will be selected as the substrate material, and AlGaAs with Al accounting for 0.3 as the material to be deposited so that a good picture can be obtained from HRTEM and a satisfactory mismatch ratio between GaAs and AlGaAs can be ensured.

Table 4.1 - Mismatch ratio between GaAs and AlGaAs

Material	Lattice constant (Å)	Mismatch ratio **δ** (%)	**δ**' (%)
GaAs	a_s =5.65361	0.14307	0.14317
AlGaAs	a_e =5.66171		

4.3.4. MBE System and Fabrication of Nanolinewidth and Nanopitch Specimens

The MBE system (V80H MBE, Oxford Instruments, UK) employed to fabricate nanolinewidth and nanopitch specimens is shown in Figure 4.3. It is used mainly for solid-state Ⅲ-Ⅴ compound semiconductor epitaxy. Figure 4.4 demonstrates its schematic diagram.

The equipment is made up of quick mounting, preparation and growth chambers. The quick mounting chamber is mainly for separating the preparation and growth chambers. It has a turbo-molecular pump to maintain a high vacuum level in the

preparation and growth chambers. Also in this chamber there is a heater to degas the sample. The preparation chamber is designed for storage of samples in a high vacuum environment, and also has a heater to degas the sample. Its vacuum is maintained by an ion pump. The growth chamber includes 8 temperature-controlled evaporation cells, with a shutter employed to turn on or off each evaporation cell. An ion pump is used to maintain the vacuum in an evaporation cell. A quadrupole mass spectrometer (QMS) is installed in the growth chamber to detect residual gases, and a reflection high energy electron diffraction (RHEED) system for real-time monitoring of growth quality and growth rate. In the growth process, liquid nitrogen is used to cool cryo-shrouds and a Ti sublimation pump is used to maintain a high vacuum environment.

Figure 4.3 - Diagram of the MBE system used for fabrications of nanolinewidth and nanopitch specimens.

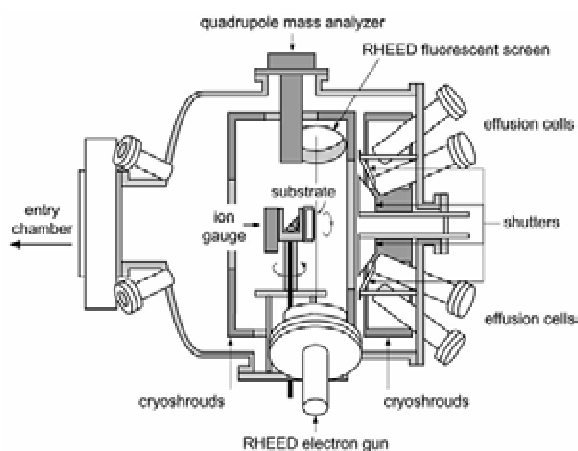

Figure 4.4 - Schematic diagram of MBE system with ultrahigh vacuum chambers.

Briefly, the process flow of MBE includes the following operations: system baking—degassing—inserting solid source materials—further system baking—further degassing—epitaxial growth—changing solid source materials—system baking.

In this chapter, a GaAs (100) wafer is selected as the substrate for MBE, which was supplied by ePAK international Inc (USA). The thickness of the substrate is 324μm. The detailed MBE-based process for nanolinewidth and nanopitch specimens is summarized as follows. First on the substrate 500nm buffer layer (GaAs) was grown, and the growth temperature was 600℃, the growth rate 1μm /h. This GaAs layer had less defects than the 324μm GaAs substrate, and was regarded as the substrate for the subsequent deposited GaAs and AlGaAs layers. Then GaAs and AlGaAs films were alternately grown on the substrate, the growth temperature was 630℃, the growth rate of GaAs 0.5μm /h, and that of AlGaAs 0.7μm /h. Finally 3nm GaAs was grown to protect the deposited multilayers, the growth temperature is 600℃, and the growth rate 1μm /h.

4.4. HRTEM-based Measurement of Nanolinewidth and Nanopitch Specimens

Once the specimens are fabricated, an instrument has to be selected to measure the fabricated specimens. Since the nominal sizes of the specimens are less than 10nm, in this chapter a HRTEM instrument is employed to measure the fabricated specimens. For HRTEM examination, the specimens should be thinned and processed prior to HRTEM measurement.

4.4.1. Samples Thinned and Processed Before HRTEM Measurement

In order to get images of a sample with HRTEM, two conditions should be met: the first one is that the sample should be transparent to the electron beam and the other is that it should be sufficiently thin. So a sample has to be thinned properly to meet these

requirements prior to HRTEM measurement for high quality images. The steps of the thinning process are summarised as follows.

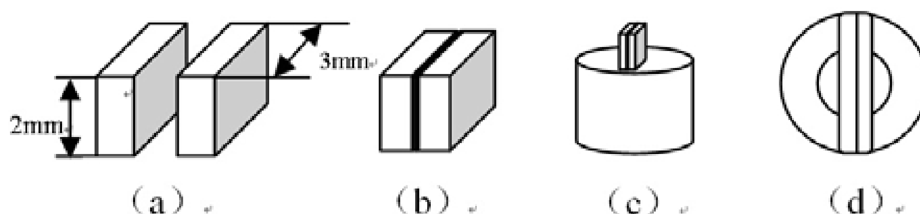

Figure 4.5 - Steps of thinning process of HRTEM samples.

Two rectangular samples, whose size are 3mm×2mm, were cut from the GaAs substrate on which AlGaAs and GaAs films were to be deposited (see Figure 4.5(a)). The glue was prepared to adhere the samples, the proportion of resin to hardner was 10:1. The samples were stuck together with the deposited layer of one substrate facing that of the other substrate. See Figure 4.5(b). The samples were clamped with forceps, ensuring the clearance between two samples was minimum, and baked on a heater whose temperature was set as 80℃ for 20 minutes. The surface of an abrasive tool was rinsed with alcohol. After the samples cooled down, they were placed to the center of the abrasive tool. The samples were manually ground off 1mm from both sides of the substrate with P5000# abrasive paper (granularity size 3.5μm). One side of the samples was polished with SiO_2 polishing powder (whose size was 0.05μm), then the other side till the thickness of the samples was 5~15μm. During the polishing process, the samples were rinsed with water frequently to avoid scratching the surface. The samples were stuck on a copper ring with the glue mentioned above. Outer and inner diameters of the copper ring were 3mm and 2mm respectively (see Figures 4.5(c) and (d)). The copper ring was heated to solidify the glue. The copper ring plus

samples were rinsed with acetone, then dried. The sample was thinned further, by ion-beam milling, until the thickness was about 50nm~100nm.

4.4.2. HRTEM Images of Fabricated Nanolinewidth and Nanopitch Specimens

Upon the completion of the above mentioned MBE-based fabrication and the thinning process, the nanolinewidth and nanopitch specimens were measured with a JEM2010 HRTEM (JEOL Ltd., Japan).

Figure 4.6(a) demonstrates an HRTEM image of the fabricated nanolinewidth specimen, and Figure 4.6(b) that of the fabricated nanopitch specimen. For the nanolinewidth specimen, the norminal linewidths are 2nm, 4nm, 6nm, 8nm respecitvely. With regard to the nanopitch specimen, the norminal pitch is 5nm. The detailed quality analysis of the fabricated specimens will be addressed in the next section of this chapter.

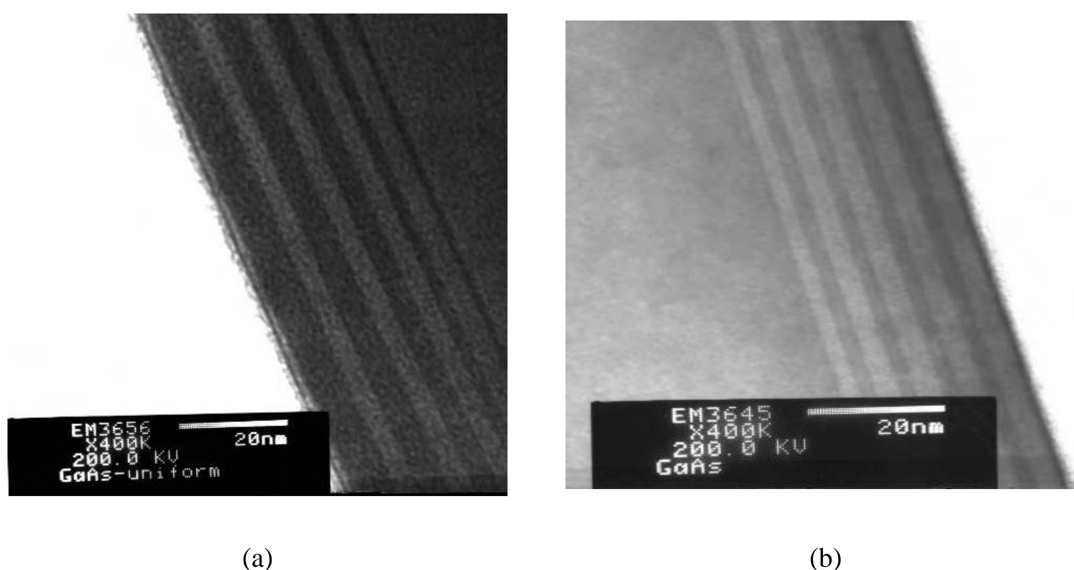

(a) (b)

Figure 4.6 - HRTEM images of fabricated specimens. (a) nanolinewidth. (b) nanopitch.

4.5. Nanoroughness Metrology and Its effect on the Precision of Nanolinewidth and Nanopitch Specimens

With HRTEM images of the specimens obtained, the characterization of LER/LWR of the grating lines will be conducted and the effects of nanoroughness on the precision of the specimens can be concluded. It should be noted that the tilt of images should be corrected first before filtration and extraction operations for line edge profiles of HRTEM images (see Figure 4.6) to be conducted in order that the characterization is more easy and accurate. Figure 4.7 demonstrates the HRTEM images after corresponding tilt correction.

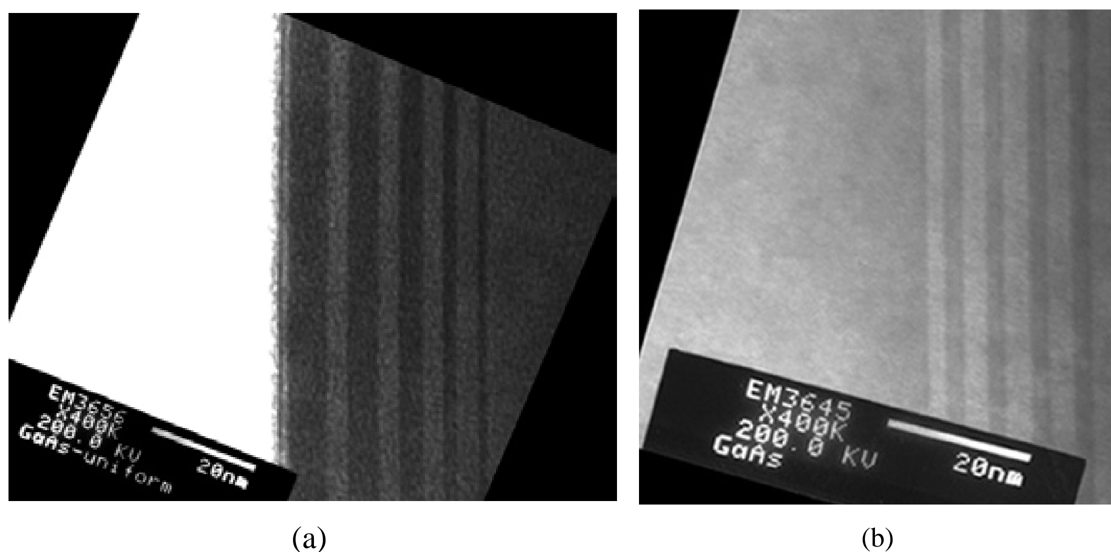

(a) (b)

Figure 4.7 - Tilt correction of HRTEM images of fabricated nanoscale specimens: (a) nanolinewidth specimen and (b) nanopitch specimen.

4.5.1. Main Steps for HRTEM Images Preprocessing

The main steps of the algorithm for the detection of the line edges from the HRTEM image shown in Figure 4.7 is demonstrated in Figure 4.8, including the transformation of a image into an array of pixel intensities, the determination of a pixel size in nm

unit, image noise-smoothing, selection of an image region for subsequent line edge analysis, and eventually line edge detection.

With the tilt of HRTEM images corrected as shown in Figure 4.7, the size of a pixel in the above mentioned images has to be determined for subsequent LER/LWR characterization. Coordinates (x, y) (in pixels) and an integer in the range (0 to 255) which represents a grey-scale, are employed to describe a given image. In the following sections we assume that the discrete spectrum of the image grey-scale values agrees with the continuous signal intensity values of HRTEM transmission electrons. Nevertheless real signals always include noise. This noise has to be reduced with noise-smoothing filters. The direct signals or their derivatives can be used to analyze the smoothed image, and in this chapter the direct signals are employed for more accurate characterization of LER/LWR. For the images in Figure 4.7, the size per pixel is 20/200, i.e. 0.2nm.

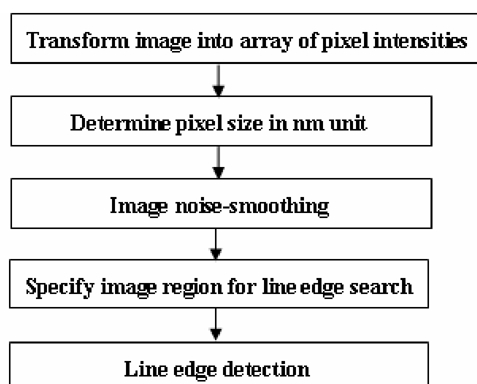

Figure 4.8 - Main steps of the algorithm for detecting the line edges from a HRTEM image.

4.5.2. Filtration of HRTEM Images

4.5.2.1. Introduction to Image Noises

Noise in HRTEM images should be smoothed before detection and characterization of the grating line edge profiles are conducted. Noise affecting the HRTEM imaging process includes the following: the noise caused by the components of the HRTEM, the dark current noise produced by incident electron beams, shot and thermal noise caused by the measurement current, the noise from the current change produced by mechanical vibration, and the noise caused by the electronic circuits of the measurement system[4.13].

To a large extent, the method of noise-smoothing depends on the kind of a noise. Usually noise includes additive noise, multiplicative noise, quantization noise, and pepper & salt noise[4.14]. Additive noise is random and uncorrelated with the image signals; examples include white Gaussian noise, channel noise produced during the image transmission process, random noise introduced by image sensors, and amplifier noise etc. Multiplicative noise is correlated with the image signals and varies along with the change in the image signals, such as the noise caused by film grain size as well as photon noise, etc. Quantization noise is the main source of noise in a digital image, and its magnitude is determined by the sampling frequency of the digital image and, hence, is unavoidable. In order to decrease the quantization noise, the sampling frequency has to be increased, resulting in larger storage required for the digital image. Therefore a compromise between the image storage and its visualization needs to be made for this kind of noise to be smoothed effectively. Pepper & salt noise is a pulse noise produced by image sensors, channel transmission and the decoding process, resulting in black and white dots in images.

4.5.2.2. Frequently-used Filters for Image Noises Smoothing

Pixel grey-scale values in one area of an image are highly correlated with those of their neighboring pixels. This correlation leads to the result that the image energy mainly concentrates within the low frequency domain, while the image details (and image noise) concentrate in the high frequency domain. The aims of image-smoothing are suppressing noise, increasing low frequency components and decreasing high frequency components[4.15]. There are two kinds of image smoothing methods, one is in the spatial domain method, and the other is the frequency domain method[4.15]. The spatial domain method is a direct processing of image pixels. The filters usually employed include a mean-value filter, a median filter and a Gaussian filter. The frequency domain methods are an indirect processing of images pixels in frequency domain first; then the results are transformed back to the spatial domain. Low-pass filters are always used to smooth this kind of noise. Attention needs to be paid to selecting appropriate filters for specific images to be processed.

- Mean-value filter

Mean-value filtering is a local processing method in the spatial domain, and the filter is a linear one. Suppose that the distribution of additive noise is independent and random, the mean-value of the neighboring grey-scales can be used to suppress noise. The detailed filtering flow is summarised as follows. Assume an image before filtering is $f(x, y)$ and the image after filtering is $g(x, y)$. Then the grey-scale value of every pixel is replaced by the average value of neighboring grey-scale values of point (x, y). The equation is as below:

$$g(x,y) = \frac{1}{M} \sum_{(i,j)\in S} f(i,j) \qquad (4.3)$$

Where S is the neighboring aggregate whose centre is (x,y),

M is the pixel number within the neighboring aggregate,

$g(x,y)$ is the grey-scale value at point (x,y) after filtration,

$f(i,j)$ is the grey-scale value at point (x,y) before filtration.

The advantages of the mean-value filter include its simplicity, high calculation speed, and being very effective for filtering Gaussian noise. The disadvantages are that the high frequencies of an image and the details near a sharp point are also filtered out, resulting in a blurry line edge. The effectiveness of filtering depends on the size of the template. The larger the size of the template, the more the blur in the filtered image.

- Median filter

Compared with the previous filter, the median filter is a typical nonlinear one which replaces the pixel grey-scale value at the center point of a window by the average value of the pixel grey-scale values in this window. Suppose $\left\{f_{ij},(i,j)\in I^2\right\}$ denotes the grey-scale value at a point in a digital image, then the filter output is as below,

$$g(i,j) = Med\{f_{ij}\} = Med\{f_{(i+k),(j+l)}(k,l) \in A(i,j) \in I^2\} \qquad (4.4)$$

The advantage of the median filter is that while the noise is being filtered out the edge details is saved, producing little blurring in the image. Nevertheless the form and the size of the filter window affect the filtering efficiency very significantly. Usually the window is set as 3 first, then 5, gradually increasing till filtering effectiveness is satisfactory. If the template is too large, the edge information would be lost and the image processing efficiency would be low. If the template is too small, the filtering is

unsatisfactory.

Since the statistic characteristics of the image to be filtered are not employed during image processing, the median filter is easy to use. It can not only filter out random noise (for example pulse noise, and pepper & salt noises, etc.), but also does not result in a blurry edge. So it can save the original signal well, and has a better filtering effectiveness when the variation of the grey-scale values is very little. The median filter is not suitable for the filtration of images which have features, such as points, lines and sharp peaks.

- Gaussian filter

The Gaussian filter is a linear filter which determines its weight value based on the form of a Gaussian function. It is very effective for suppressing noise whose distribution is a normal one. The following function (2-dimensional, the mean value is zero) is always employed as a Gaussian filter:

$$G(x, y) = e^{-\frac{x^2+y^2}{2\sigma^2}} \tag{4.5}$$

Where σ is a standard deviation and determines the width of the filter,

(x, y) is the coordinate of a point in the image of interest.

The filtering is achieved by convolution of Eq. 4.5 with the image of interest. The 2-D Gaussian function has the following important properties: rotational symmetry, uniqueness, separability as well as a unique value in the frequency domain. These properties ensure that this filter is an effective low-pass one not only in the spatial domain but also in the frequency domain as well.

4.5.2.3. Selection of the Filter for the Filtering of HRTEM Images

According to the literature [4.16], the following conclusions were employed to select the filter for the filtering of the HRTEM images. Gaussian filtering gave larger values of sigma, while median and linear filters were producing greater smoothing and gave lower values of sigma, since the latter two were greatly reducing the high frequency components of LER. It can be concluded that Gaussian filtering is better than the other two methods. Hence in this thesis a Gaussian filter is selected for filtering HRTEM images.

4.5.3. Extraction of Line Edge Profiles from HRTEM Images

With noises filtered out from the HRTEM images, the positions of line edge profiles of the fabricated specimens have to be detected for the subsequent characterization process. Detecting the position of line edges of the specimens is very important for LER/LWR characterization. Grating line edges mean the pixel aggregates those grey-scale values that have step or peak changes. These line edges form the 2-D profiles for further measurement and characterization of nanoroughness.

4.5.3.1. Traditional Line Edge Detect Operators

Line edges in an image demonstrate a discontinuity of the image characteristics within a local area, such as the changes of grey-scale values and their gradients. The detection of line edges is the first step in all boundary-based image segmentation. Traditional edge detection operators detect the grey-scale change of a specific neighboring area of a pixel, and determine the line edge using the changes of the first or second order derivatives. There are two steps in conducting line edge detection: first an edge enhancement operator is employed to mark a local edge, then the edge

intensity is defined and a threshold value is set to extract aggregates of edge points [4.17].

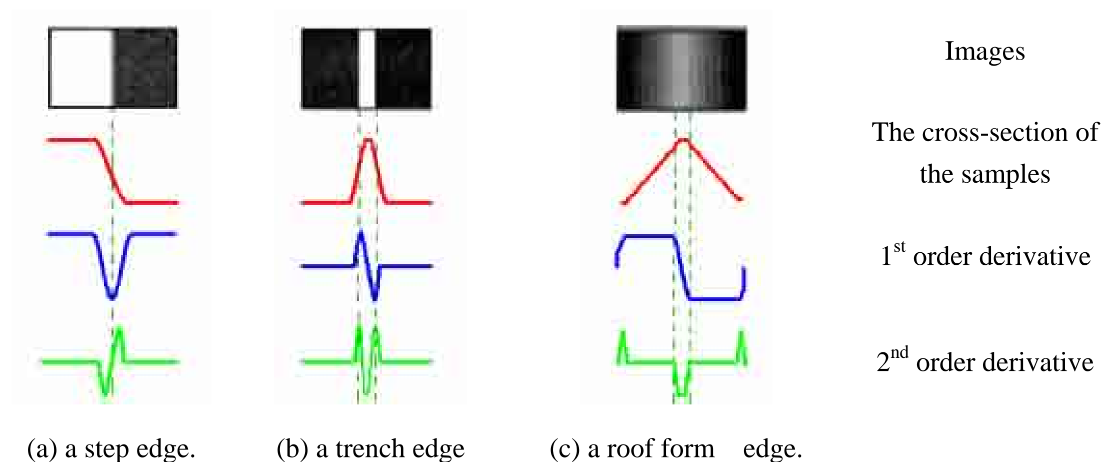

(a) a step edge. (b) a trench edge (c) a roof form edge.

Figure 4.9 - Categories of line edges and corresponding line edge detection process[4.18].

Generally speaking there are two kinds of line edges, one is a step edge and the other is a roof edge [4.18], see Figure 4.9. For a step edge, the values of grey-scales at both sides of the line edge are significantly different. A roof edge is a turning point where the values of the grey-scale change from increasing to decreasing. In this chapter the grating line edges to be investigated are all step edges, but were changed into slope edges by noises produced by the electron imaging system, sampling process and illumination conditions, etc.

According to the types of finite differences, edge detections can be classified as one of the following two kinds: the first order derivative operator and the second order derivative operator[4.19-4.20]. The representatives of the former include the Roberts operator, Sobel operator and Prewitt operator. The Canny, Laplacian and LOG operators represent the latter.

Line edges are not always detected successfully with traditional line edge detection

operators [4.21]. Blurred edges may be lost and false edges may be detected since HRTEM has the following disadvantages during the measurement of the grating structure with critical dimension less than 10nm, that is, considerable noise was included in HRTEM images, especially in images with high magnifications since the HRTEM image is a 2D projection of a 3D sample, and the image contrast of the grating line edge was low. This means that the traditional operators mentioned above cannot meet the requirements of the edge detection process. In the following sections a wavelet transform-based multi-scale line edge detection is introduced to detect the position of line edges in a nanoscale grating structure.

4.5.3.2. Wavelet Transform-based Multi-scale Line Edge Detection

Since noise and line edges in a HRTEM image are all signals with high frequencies, it is difficult to distinguish between them by frequency. It is noted that the main difference is that they have different energy, that is line edges have a higher energy and larger range. So the position of a signal on a grating line edge can be detected by the characteristics of its continuous wavelet transform, i.e. the properties on multi-scale (also call multi-resolution). According to this property, the signal can be investigated in different resolutions.

According to the Mallat modulus maximum principle[4.22], a wavelet transform is defined with a convolution transform. Suppose $\psi(x) \in L^2(R)$ is a mother wavelet, and meets the admissible condition of a wavelet. Then

$$\int_R \frac{|\psi(\omega)|^2}{\omega} d\omega < \infty \qquad (4.6)$$

Where $\psi(\omega)$ is Fourier transform of $\psi(x)$,

ω is the angular frequency.

The wavelet function with a scale a is shown below:

$$\psi_a(x) = \frac{1}{a}\psi(\frac{x}{a}) \quad (4.7)$$

According to Mallat's definition, the wavelet transform $WTf_\psi(x,a)$ of a arbitrary function $f(x) \in L^2(R)$ is the convolution of $f(x)$ and $\psi_a(x)$,

$$WTf_\psi(x,a) = f(x) * \psi_a(x) = \frac{1}{a}\int_{-\infty}^{+\infty} f(\tau)\psi(\frac{x-\tau}{a})d\tau \quad (4.8)$$

Suppose $\theta(x)$ is a low-pass filter function, and has the first and second derivatives denoted by $\xi(x)$ and $\eta(x)$. In accordance with the differential properties of the Fourier transform, it is concluded that both $\xi(x)$ and $\eta(x)$ meet the admissible condition and can be regarded as the wavelet mother function for wavelet transform. With the elastic factor a ($a > 0$) introduced, the following equation can be derived,

$$\theta_a(x) = \frac{1}{a}\theta(\frac{1}{a}) \quad (4.9)$$

For an arbitrary signal function $f(x) \in L^2(R)$, the wavelet transform at position τ with a scale as a is as follows,

$$WT_\xi f(x,a) = \frac{1}{a}\int_{-\infty}^{\infty} f(\tau)\xi(\frac{x-\tau}{a})d\tau = a\frac{d}{dx}[f(x) * \theta_a(x)] \quad (4.10)$$

$$WT_\eta f(x,a) = \frac{1}{a}\int_{-\infty}^{\infty} f(\tau)\eta(\frac{x-\tau}{a})d\tau = a^2\frac{d^2}{dx^2}[f(x) * \theta_a(x)] \quad (4.11)$$

Figure 4.10 and Figure 4.11 show that first the original signal $f(x)$ is filtered and its noises are smoothed, then the change rate of $f(x)$ is calculated by a differential operation. If there is a change point in $f(x)$, the change rate at this point is maximum, that is the modulus maximum of the wavelet factor. So the position where the extreme point $WT_\xi f(x,a)$ exists can be regarded as one point of the line edge

signal $f(x)$.

$WT_{\eta} f(x,a)$ is the second derivative of $f(x)$ which is filtered by $\theta_a(x)$. The zero point of the second derivative of a function corresponds to the extreme point of the first derivative. So the zero point of $WT_{\eta} f(x,a)$ is employed to detect the edge position of the signal $f(x)$. Usually the original signal $f(x)$ includes different kinds of noise, causing $WT_{\eta} f(x,a)$ to have many zero points; it is very difficult to detect the real position of a line edge with $WT_{\eta} f(x,a)$. In engineering applications it is necessary to employ the modulus maximum $WT_{\xi} f(x,a)$ to detect the real line edge of the signal $f(x)$.

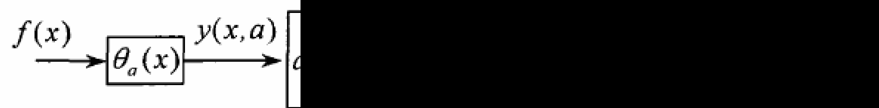

Figure 4.10 - Diagram of the equivalent wavelet transform of $WT_{\xi} f(x,a)$ [4.22].

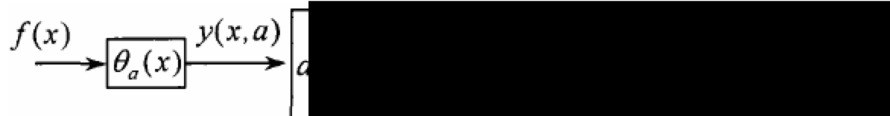

Figure 4.11 - Diagram of the equivalent wavelet transform of $WT_{\eta} f(x,a)$ [4.22].

4.5.3.3. Lipschitz Power Discrimination of a Noise Singular Point

For an image which includes additive Gaussian white noise, the maximum of the wavelet transform factor may correspond to a noise point, instead of a characteristic edge point. Hence it is necessary to find and delete these modulus maxima after their detection. The Lipschitz exponent (also called L exponent in the following sections) can be employed to detect these noise points. Mallat has proved that if the L

exponent of a function $f(x_1, x_2)$ is a, the modulus maximum satisfies the following inequalities[4.23],

$$\left|Mod\left[WTf(2^j, x_1, x_2)\right]\right| \le A2^{j(a+0.5)} \tag{4.12}$$

That is,

$$\log_2\left|Mod\left[WTf(2^j, x_1, x_2)\right]\right| \le (a+0.5)j + \log_2 A \tag{4.13}$$

Where A is a constant,

j is the scale,

a is the L exponent.

The above inequalities show that the modulus maximum of a wavelet transform is not larger than $A2^{j(a+0.5)}$ at the scale 2^j, and are always employed for wavelet transform-based detection of noise singular points.

4.5.3.4. Wavelet Transform-based Multiscale Line Edge Detection

According to the principle mentioned above, one HRTEM image was selected and smoothed with a Gaussian filter, see Figure 4.12(a). The filtered HRTEM image was scanned and the signal intensities of a line profile were obtained, see Figure 4.12(b). A wavelet function was selected to transform every scan line of the image, and the modulus maximums of the wavelet transform factors at different scales were calculated. Figure 4.12(c) shows the modulus maximum of a signal intensity line.

According to Eq.(4.13) the singular point was determined. If a was larger than or equal to zero and the corresponding modulus maximum of the wavelet transform decreased gradually when the scale j increased, the point was regarded as a line edge point. If a was less than zero and the corresponding modulus maximum of the

wavelet transform decreased more rapidly along when the scale decreased, the point was regarded as a noise point.

The value of a modulus maximum which corresponded to a line edge point was determined. In this chapter it was considered that the position accuracy of the modulus maximum was highest when the condition that $s = 1$ was met. All detected edge points were connected to form the line edge profile, see Figure 4.12(d).

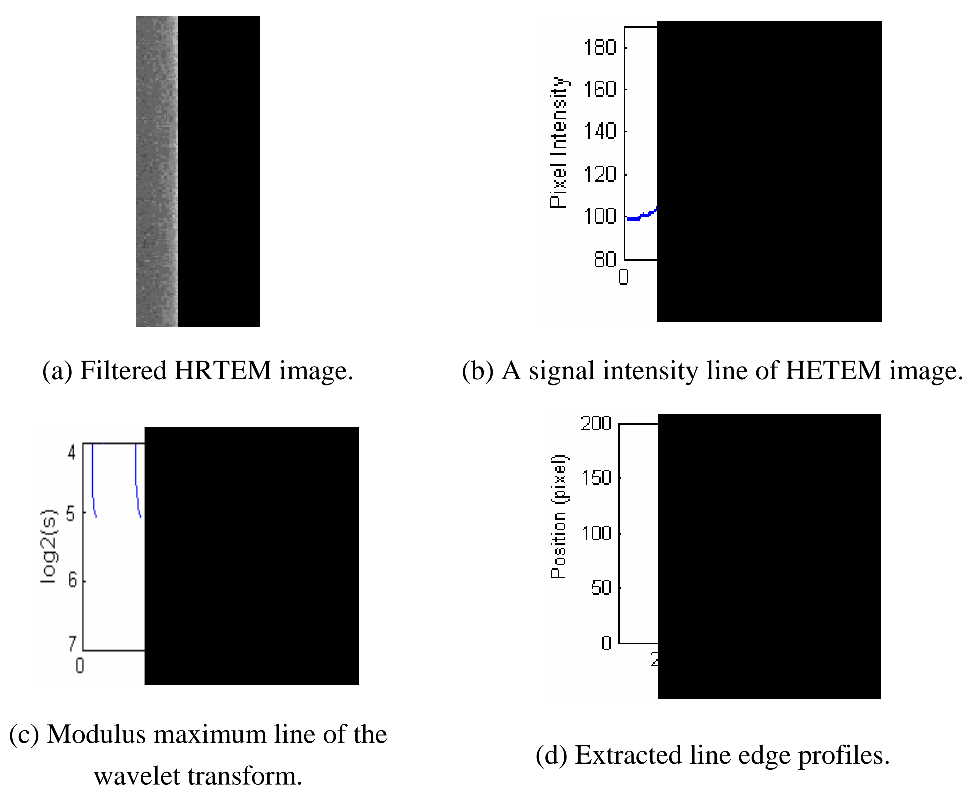

(a) Filtered HRTEM image.

(b) A signal intensity line of HETEM image.

(c) Modulus maximum line of the wavelet transform.

(d) Extracted line edge profiles.

Figure 4.12 - Steps of the wavelet transform-based multiscale line edge detection.

Figure 4.13 shows the detected line edge positions of the linewidth specimen by the wavelet transform-based multi-scale line edge detection. It shows that this kind of line edge detection is less affected by noise in the original image, and can extract the line edge position accurately.

4.5.4. Fitting of the Detected Line Edges

Fit is defined as an operation in which an ideal feature approaches a non-ideal feature. There are two kinds of datum lines to be fitted for the detected line edges [4.24]. One is the least-squares datum, the other the arithmetic average datum. The former is more accurate than the latter, but the latter is easy to use in some cases where the required accuracy is not high. In this thesis the least-squares method is employed to fit the datum line for the detected line edges, so that subsequent nanoroughness characterization can be conducted.

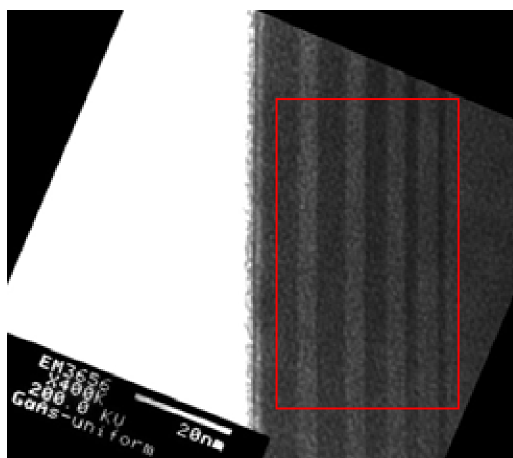

(a) Original HRTEM image of the nanolinewidth specimen.

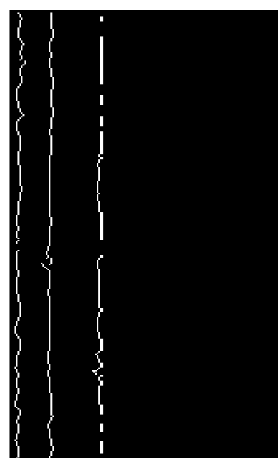

(b) Line edge profiles extracted from the red box in Figure 4-13(a).

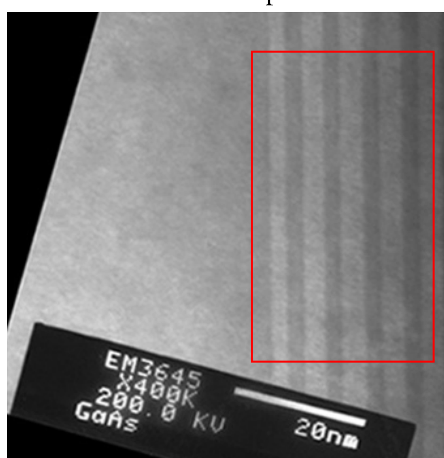

(c) Original HRTEM image of the nanopitch specimen.

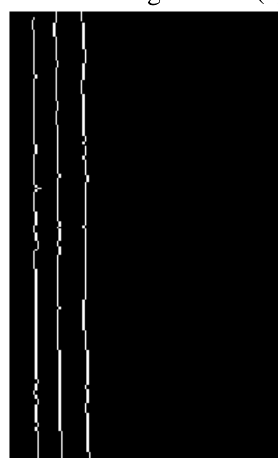

(d) Line edge profiles extracted from the red box in Figure 4-13(c).

Figure 4.13 - Wavelet transform-based multi-scale line edge detection for the nanolinewidth and nanopitch specimens.

4.5.5. Characterization of Line Edge Profiles

After determining the line edge profiles of the nanolinewidth/nanopitch specimens from an HRTEM image, the analysis and characterization of its nanoroughness follows. According to section 3.2.2 in Chapter 3, the following three descriptors are employed to characterize the LER/LWR of the line edges: RMS σ, HHCF and PSD.

4.5.5.1. RMS σ

According to the definition and relevant algorithms introduced in section 3.2.2.1 of Chapter 3, RMS σ of the LER/LWR of a line edge profile was calculated. Table 4.2 and Table 4.3 show the RMS σ values of LER/LWRs of the nanolinewidth and nanopitch specimens shown in Figure 4.13. The line edge roughness includes the right and left line edge roughnesses respectively.

Table 4.2 - Linewidth and RMS σ of LER/LWRs of the nanolinewidth specimen.

Nominal linewidth(nm)	σ_{LER} of left edge	σ_{LER} of right edge	σ_{LWR} of linewidth	Fabricated linewidth(nm)
2	0.15	0.17	0.20	2.18
4	0.26	0.18	0.31	3.73
6	0.19	0.18	0.24	5.61
8	0.24	0.22	0.26	7.84

Table 4.3 - Pitch and RMS σ of LER/LWR of the nanopitch specimen.

Nominal pitch(nm)	σ_{LER} of left edge	σ_{LER} of right edge	σ_{LWR} of linewidth	Fabricated pitch(nm)
5	0.197	0.19	0.22	4.29
5	0.22	0.24	0.32	4.65
5	0.20	0.19	0.31	4.92

4.5.5.2. Height-height Correlation Function(HHCF)

The HHFCs of all extracted line edges shown in Figure 4.13 (b) and Figure 4.13 (d) were calculated according to the definition and the algorithms of HHFC described in section 3.2.2.2 of Chapter 3. Figure 4.14 gives the HHCF of the left edge of the 4nm grating line shown in Figure 4.13 (b). Figure 4.15 shows the HHCF of the left edge of the first grating line shown in Figure 4.13 (d). The correlation length ξ of the line edges of the nanolinewidth and nanopitch specimens were calculated accordingly and shown in Table 4.4 and Table 4.5.

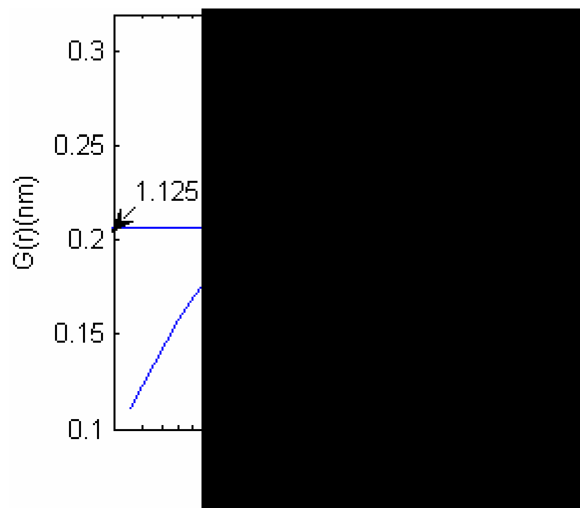

Figure 4.14 - The HHCF of a grating line whose nominal linewidth is 4nm shown in Figure 4.13(b).

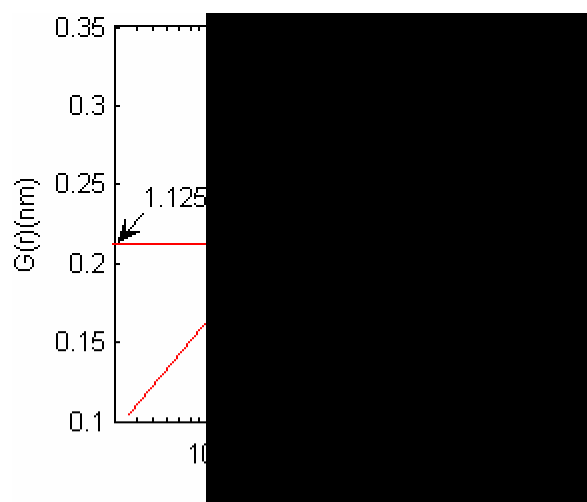

Figure 4.15 - The HHCF of the left edge of the first grating line shown in Figure 4.13(d).

Table 4.4 - Correlation length ξ of the line edges of the nanolinewidth specimen.

Norminal linewidth(nm)		2	4	6	8
Correlation length ξ (nm)	Left edge	1.44	1.51	1.18	1.63
	Right edge	1.62	1.48	2.04	1.20

Table 4.5 - Correlation length ξ of the line edges of the nanopitch specimen.

Nominal pitch (nm)		5	5	5
Correlation length ξ (nm)	Left edge	1.28	1.22	1.32
	Right edge	2.05	1.60	1.70

4.5.5.3. Power Spectral Density(PSD)

The PSDs of all extracted line edges shown in Figure 4.13 (b) and Figure 4.13 (d) were calculated according to the definition and the algorithms of PSD described in section 3.2.2.3 of Chapter 3,. Figure 4.16 gives the PSD of the left edge of the 4nm grating line shown in Figure 4.13 (b). Figure 4.17 shows the PSD of the left edge of the first grating line shown in Figure 4.13 (d).

Roughness exponent α of the line edges of the nanolinewidth and nanopitch specimens were derived from the PSD curves and are shown in Table 4.6 and Table 4.7.

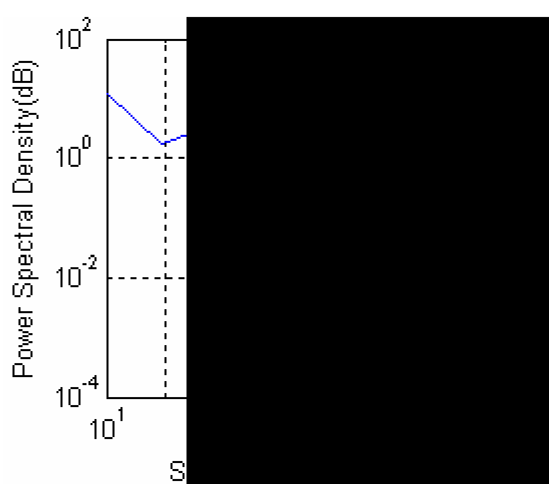

Figure 4.16 - PSD of the left line edge whose norminal linewidth is 4nm as shown in Figure 4.13(b).

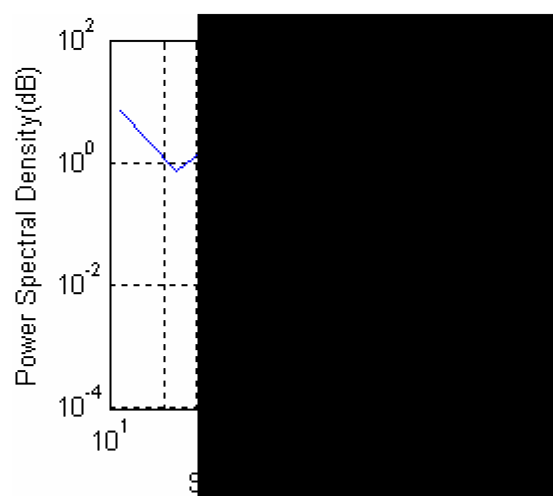

Figure 4.17 - PSD of the left line edge of the first grating line as shown in Figure 4.13(d).

Table 4.6 - Roughness exponent α of the line edges of the nanolinewidth specimen.

Nominal linewidth (nm)		2	4	6	8
Roughness exponent α	Left edge	0.27	0.47	0.32	0.20
	Right edge	0.32	0.29	0.40	0.07

Table 4.7 - Roughness exponent α of the line edges of the nanopitch specimen.

Nominal pitch (nm)		5	5	5
Roughness exponent α	Left edge	0.36	0.44	0.36
	Right edge	0.30	0.22	0.30

4.6. Nanoroughness-based Process Regulation for Nanolinewidth and Nanopitch Specimens

Table 4.2 shows the fabricated linewidthes and RMS σ of the LER/LWR of the nanolinewidth specimen. Table 4.3 shows the fabricated pitches and RMS σ of LER/LWR of the nanopitch specimen. LWRs of the grating lines of the nanolinewidth specimen are 0.20nm, 0.31nm, 0.24nm, and 0.26nm respectively. Its average is 0.25nm, and the maximum difference 0.11nm. LWRs of the grating lines of the nanopitch specimen are 0.22nm, 0.32nm, and 0.31nm respectively. Its average is 0.28nm, and the maximum difference 0.09nm. It can be concluded from the above quantitative analysis that the quality of line edges is high, and the uniformity of line edge profiles meets the corresponding requirements of nanolinewidth and nanopitch specimens. The linewidths of all the fabricated lines (except the line whose nominal

linewidth is 2nm) of the nanolinewidth and the nanopitch specimens are a little smaller than the relevant nominal sizes, this suggests that more epitaxy time is needed to deposit every AlGaAs layer to increase nominal linewidthes and nominal pitch of the nanolinewidth and nanopitch specimens respectively.

Table 4.4 demonstrates the roughness exponents of the line edges of the fabricated nanolinewidth specimens. Table 4.5 shows that of the fabricated nanopitch specimen. For the nanolinewidth specimen, the correlation lengths ξ of the left line edge are 1.44nm, 1.51nm, 1.18nm and 1.63nm respectively, and that of the right line edge are 1.62nm, 1.48nm, 2.04nm and 1.20nm. Their averages are 1.44nm and 1.34nm, and their maximum differences are 0.45nm and 0.85nm respectively. This demonstrates that in real space both the left and the right line edges have similar profiles, while the right line edges look a little rougher than the left ones and the average of the correlation lengths of the left line edges are a little larger than that of the right ones. This conclusion is also confirmed by the analysis of the roughness exponents shown in Table 4.6 and Table 4.7. For the roughness exponents of the left line edges of the nanolinewidth specimen, the average value is 0.32, and the maximum difference is 0.27. With regard to the roughness exponents of the right line edges of the nanolinewidth specimen, the average value is 0.27, and the maximum difference is 0.33. This shows that all the left line edges and the right line edges of the nanolinewidth specimen have almost the same frequency components, the right line edges are a little rougher than the left ones, and the consistency of all the left and right line edges is acceptable. The conclusion obtained from the analysis of the correlation

lengths agrees with that from the analysis of the roughness exponents. With regard to the nanopitch specimens, similar conclusions can be reached about the line edges.

All these show that the material selection and the MBE process can meet the requirements for the fabrication of nanolinewidth and nanopitch specimens.

4.7. Summary

In this chapter a method to observe the thicknesses of the deposited multilayers on a substrate as the norminal linewidth and norminal pitch of the nanolinewidth and the nanopitch specimens was introduced, and a fabrication process based on MBE was presented to fabricate these kinds of nanolinewidth and nanopitch specimens, whose nominal linewidthes are 2nm, 4nm, 6nm, 8nm respectively, and the nominal pitch is 5nm. Taking image contrast and mismatch ratio between the epitaxial material and the substrate material into consideration, GaAs and AlGaAs were selected for the fabrication of the nanolinewidth and nanopitch specimens. HRTEM was used to measure the grating lines of the fabricated nanopatterns. Image processing was employed to conduct noise-smoothing and extraction operations for these HRTEM images. Three descriptors of the LER/LWR of the line edges were used to characterize the quality of grating lines of the nanopatterns fabricated with the MBE technique. The result shows that the material selection and MBE process can meet the requirements for the fabrication of nanolinewidth and nanopitch specimens.

CHAPTER 5

FABRICATION AND NANOROUGHNESS CHARACTERIZATION OF A CAPACITOR WITH HfO_2 AS A HIGH k DIELECTRIC FILM

5.1. Introduction

This chapter presents a study to establish the relationship between the roughness as a result of nanofabrication and the performance of a metal-insulator-semiconductor (MIS) capacitor. The direct relationships between nanoroughness as a result of fabrication and the performance of an electric component provide a necessary reference for the conventional quality of fabrication[5.1]. The MIS capacitor is one of the most used components for establishing these relationships[5.2, 5.3]. It is also used in this research.

A prototype MIS capacitor with a hafnium oxide (HfO_2) film as the high k dielectric was fabricated, the surface and interface roughness were characterized, and its performance was measured. From analysis, the direct relationships between the

MIS capacitor performance and corresponding fabrication parameters were established, so that relevant fabrication process can be regulated and the MIS capacitor quality improved.

In the following sections, the design of the MIS capacitor is first introduced, including selection of HfO_2 as the high k dielectric film and Mo as the upper electrode, as well as the detailed MIS capacitor structure. It is followed by fabricating the MIS capacitors, including deposition and annealing processes for HfO_2 dielectric on a Si substrate. Then it proceeds to the performance measurement of the MIS capacitors, including the leakage current density and capacitance–voltage(C-V) property. This chapter continues with characterization of surface roughness of HfO_2 films with an AFM and interface roughness with an SEM. Finally the relationships between the MIS capacitor performance, corresponding annealing temperature and relevant roughness are briefly discussed to further regulate the relevant fabrication process.

5.2. Design of the MIS Capacitor With HfO_2 as a High k Dielectric

5.2.1. Background on a MIS capacitor

Usually silicon dioxide is employed as the dielectric material for an MIS capacitor adopted in semiconductor devices. With continuous development of semiconductor devices, the equivalent oxide thickness (EOT) of silicon dioxide is becoming so thin that its leakage current is too large, worsening the stability and reliability of relevant devices [5.4]. In order to improve the device performance it is imperative to introduce

new high k dielectrics to replace silicon dioxide. Most high k dielectrics have the following distinct characteristics, such as higher dielectric constant, larger band gap as well as better mechanical and thermal stabilities[5.5]. For example, in CMOS (complementary metallic oxide semiconductor) devices, the physical thickness of the gate dielectric increases significantly with the introduction of a high k dielectric[5.6]. Since the relationship between the gate leakage current caused by the quantum tunneling effect and the thickness of the gate dielectric is exponential, the increase of the gate dielectric thickness will significantly decrease the direct tunneling effect [5.7].

The EOT is expressed as[5.8]

$$EOT = \frac{\varepsilon_{ox} A}{C_{meas}} = \frac{\varepsilon \varepsilon_0 A}{C_{meas}} \qquad (5.1)$$

where ε_{ox} is the dielectric constant of SiO_2,

A is the capacitor area,

C_{meas} is the measured capacitance,

ε is the dielectric constant of high k gate dielectric,

ε_0 is the vacuum permittivity.

Eq. 5.1 shows that, with the unit gate capacitance kept constant, the physical thickness of the high k dielectric will become larger than that of silicon dioxide, significantly decreasing the gate leakage current.

5.2.2. Selection of HfO_2 as a High k Dielectric for the MIS Capacitor

Generally high k dielectric materials include nitrides, oxides and ferroelectric materials. The dielectric selection is mainly based on the comparisons between the

properties of dielectric materials, such as the dielectric constant, the band gap and the difference of its conduction band to that of the corresponding substrate, see Table 5.1[5.9].

Table 5.1 - Comparison of relevant properties for some high k dielectrics and silicon oxides[5.9].

Material	Dielectric constant (k)	Band gap E_g(eV)	The conduction band difference to Si △Ec（eV）	Crystal structure
SiO_2	3.9	8.9	3.2	amorphous
Si_3O_4	7	5.1	2	amorphous
Al_2O_3	9	8.7	2.8	amorphous
Y_2O_3	15	5.6	2.3	Cubic crystal
La_2O_3	30	4.3	2.3	Hexagonal crystal, cubic crystal
Ta_2O_3	26	4.5	1-1.5	Rhombic
TiO_2	80	3.5	1.2	Pyramidal crystal
HfO_2	25	5.7	1.5	Monoclinic, pyramidal, cubic
ZrO_2	25	7.8	1.4	Monoclinic, pyramidal, cubic

Table 5.1 shows that the energy gaps of Ta_2O_5 and TiO_2 are very small, hence the differences to the barrier of Si conduction band are small too, resulting in larger leakage current and demonstrating that Ta_2O_5 and TiO_2 are not the ideal substitutes as high k dielectric materials. With regard to HfO_2 and ZrO_2, their dielectric constants and energy gaps are larger, the differences to the barrier of Si conduction band are larger too, leading to smaller leakage current and their popularity as high k dielectrics in the microelectronics industry. With the introduction of high k gate

dielectric materials, such as HfO_2 and ZrO_2, into MOS devices, the leakage current density of their gate dielectric can decrease at least 4 orders of magnitude while their physical thickness is increasing (provided that their EOT s are the same)[5.9]. In this chapter, HfO_2 was selected as the high k dielectric for the MIS capacitor.

5.2.3. Design of the MIS Capacitor with HfO_2 as High k Dielectric

Figure 5.1 shows a diagram of the MIS capacitor with HfO_2 as the high k dielectric. Here the upper electrode Mo is of metal, the HfO_2 layer is the dielectric, and there is a $p-Si$ substrate plus lower Al electrode as the semiconductor for the MIS capacitor, which is named an $Mo/HfO_2/Si/Al$ structure. The area of the upper electrode is about 1mm^2, which will be fabricated by the lift-off technique[5.10].

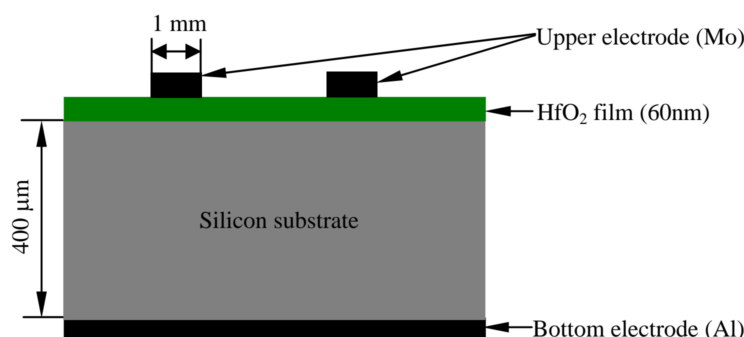

Figure 5.1- Diagram of the MIS capacitor with HfO_2 as high k dielectric.

5.3. Fabrication of the MIS Capacitor with HfO_2 as the High k Dielectric

A $p-Si(100)$ wafer with a resistivity of 5-10Ω·cm was selected as the substrate. Before depositing HfO_2 on the Si substrate, pollutants as well as oxides on the substrate were removed. The substrate was cleansed with isopropanol, propanol and

de-ionized water respectively. Then buffer oxide etch (BOE) was used to etch the natural oxides on Si substrate for 60 seconds, and de-ionized water was employed again to cleanse the substrate. Finally the substrate was dried with nitrogen gas.

For the fabrication processes of the MIS capacitors, HfO_2 films of high quality should be deposited on the cleaned substrates first, then annealed to improve the dielectric properties.

5.3.1. HfO_2 Deposition on a Si Substrate

There are several kinds of processes to deposit Hf -base high k dielectric films, such as chemical RF-(or DC-) magnetron sputtering, atomic layer deposition (ALD), vapor deposition (CVD), pulsed laser deposition (PLD), etc[5.11-5.13]. In this research, a UHV multifunction magnetron sputtering system shown in Figure 5.2 (Model: JGP560, CAS Shenyang Instrument Co., China) was employed to deposit a HfO_2 high k dielectric layer on the Si substrate.

For depositing the HfO_2 film, Hf with a purity of 99.99% was selected as the target material whose diameter is 100mm. Background vacuum of the vacuum chamber was set as $1.7\times10^{-4}\,Pa$ with a molecular pump. Three parameters should be tuned carefully in order to get high quality Hf film, such as the sputtering pressure, the substrate temperature and the sputtering power. The sputtering pressure was controlled with the mass fluxes of O_2 and Ar, the substrate temperature with a resistor heater and a FP93 temperature controller, and the sputtering power with a sputtering source whose power was 1kW and the frequency was 13.56MHz. The

sample table on which the substrate was placed rotated during deposition process to improve the film quality.

Figure 5.2- UHV multifunction magnetron sputtering system used to deposit the HfO_2 dielectric.

During the deposition process, the sputtering pressure was set as 0.25Pa, the mass flux of O_2 and Ar as 1.0 sccm (standard cubic centimeter per minute) and 11.84 sccm respectively, the substrate temperature as 300℃, and the power of target Hf as 150W. In these instances the sputtering rate of HfO_2 was 0.0217nm/s. So for the deposition of a 60nm HfO_2 film, the sputtering time should be 46 minutes.

One point that should be noted during above deposition process is that the mass fluxes of O_2 and Ar might be adjusted separately, but the mass flux ratio of O_2 to Ar should be kept constant, enabling the sputtering pressure to remain unchanged.

5.3.2. Annealing Process of the Deposited HfO_2 Films

A muffle furnace was employed to anneal deposited HfO_2 films under atmospheric pressure. The sample was placed in a quartz crucible and heated to a preset temperature, then cooled down along with the hearth of the quartz crucible to atmospheric temperature. For deposited HfO_2 whose nominal thickness is 60nm, annealing temperatures were preset as 700℃, 800℃, 850℃ and 900℃ respectively.

5.3.3. Fabricating the MIS Capacitor With HfO_2 as the Dielectric

Once HfO_2 films were deposited on Si substrates and annealed properly, the Mo electrodes with an area $1mm^2$ were fabricated by the lift-off technique. Then Al electrodes were deposited with the magnetron sputtering system on the other side of the Si substrate whose natural oxide had been etched away with BOE. Figure 5.3 shows the brief fabrication flow of the MIS capacitor ($Mo / HfO_2 / Si / Al$).

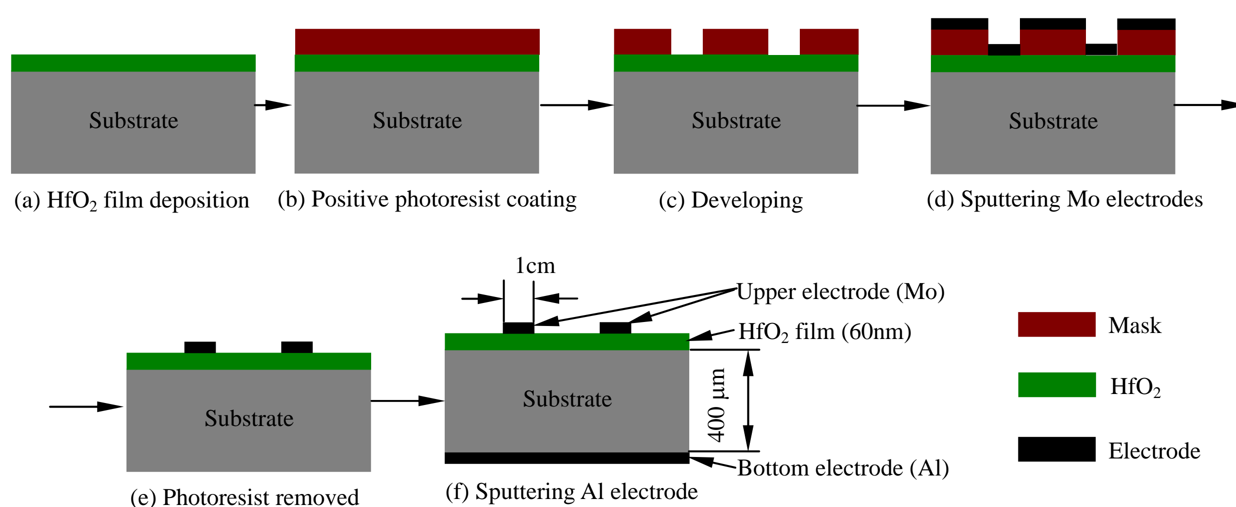

Figure 5.3- Fabrication flow of the electrodes of the MIS capacitor.

The detailed fabrication flow is summarized as follows: an HfO_2 film with nominal thickness of 60nm was deposited in the magnetron sputtering system. AZ4903 positive resist (Clariant Corporation, USA) was spun on the Si substrate on which the 60nm HfO_2 layer was deposited. The rotation speed was 300 revolutions/s for 30 seconds first, then 1000 revolutions/s for 60 seconds. Upon completion of the resist spinning, the substrate was pre-baked on a heat band whose temperature was set at 90 ℃ for 2 minutes. The pre-baked resist was exposed 10 seconds on the aligner (type: 350/NUV/DCCD, ABM Co., USA) and then developed for 1 minute. The substrate

was post-baked on the heat band again for 5 minutes. *Mo* film was deposited on the resist patterns in the sputtering system. The purity of the *Mo* target was 99.99%, the sputtering pressure 0.45Pa, the sputtering power 100W, and the deposited thickness of the *Mo* was set as 200nm. Resist patterns (as well as *Mo* patterns which were on the resist) were formed by acetone etching, and the patterns of the *Mo* electrodes were produced. The substrate was cleaned again, and the natural oxide produced during above annealing process on the reverse side of the substrate was etched away with BOE. An *Al* film was sputtered on the reverse side of the substrate in the sputtering system. The diameter of the *Al* target was 100mm and its purity 99.99%, the sputtering pressure was 0.45Pa in an *Ar* atmosphere and the sputtering power was 100W. The fabricated MIS capacitors are shown in Figure 5.4.

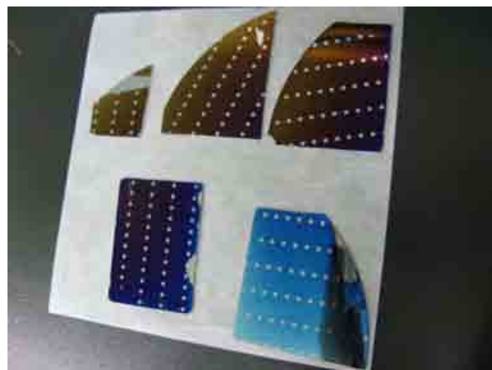

Figure 5.4. The fabricated MIS capacitors.

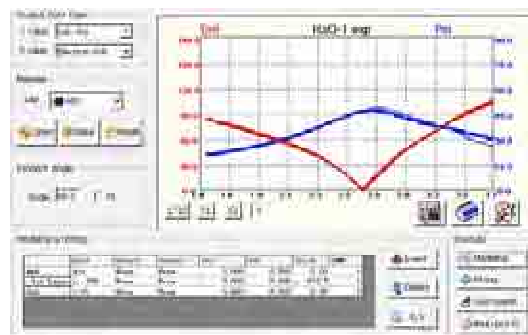

Figure 5.5 – Δ and Ψ curves of HfO_2 dielectric film.

5.4. Measurement and Characterization of the MIS Capacitor

The annealing temperature for the HfO_2 film is one of the main influential factors which impact on the leakage current, the *EOT* and the dielectric constant of the MIS capacitor. In the following sections, the effects of annealing temperature on the performance of MIS capacitor will be discussed in detail.

5.4.1. The Thickness Measurement of the HfO_2 High k Dielectric

Spectroscopic ellipsometry (SE) (SEME-1000, Nano-view, Republic of Korea) was used to measure the thickness of the deposited HfO_2 films. The range of the optical wavelength was 330~850nm, and its energy range was 1.5eV~3.7eV. Figure 5.5 demonstrates the full spectra for the amplitude Δ and the phase ψ of the reflected polarized light as a function of the wavelength from the SEME-1000 SE for the HfO_2 high k dielectric material, which were used to determine the thickness of the deposited dielectric layer. The Cauchy model was used in the system to deduce the thickness and optical constants of the deposited film[5.14]. Here the thickness obtained was 61.27nm, a little larger than the nominal thickness.

5.4.2. X-ray Diffraction (XRD) Analysis of the Annealed HfO_2 High k Dielectric

An X-ray diffractometer (D/MAX-2400, Rigaku Co., Japan) was employed to analyze the phase structures of the HfO_2 high k dielectric layers after different annealing processes. Copper $K\alpha$ radiation of wavelength is 0.154nm was used to obtain the diffraction pattern. Figure 5.6 shows XRD patterns of HfO_2 films as a function of the annealing temperature.

For all the HfO_2 samples before and after the annealing process, diffraction peaks corresponding to the (111) crystal plane appear at 28.26°, demonstrating that a slight crystallization of the HfO_2 films occurred during the deposition process. Two factors induce the crystallization process, one is the thickness of deposited HfO_2 film (crystallization will start when the thickness of the HfO_2 film is larger than a

threshold value), the other is the higher temperature of the Si substrate. For all allotropes of HfO_2 films, the monoclinic one is a stable phase at low temperature. So it can be concluded that part of the deposited HfO_2 film is crystallized into the monoclinic phase, not the other allotropes, such as tetragonal and orthogonal crystalline structures. With increasing annealing temperatures, the grain sizes also increased, causing surface fluctuation of the deposited HfO_2 films.

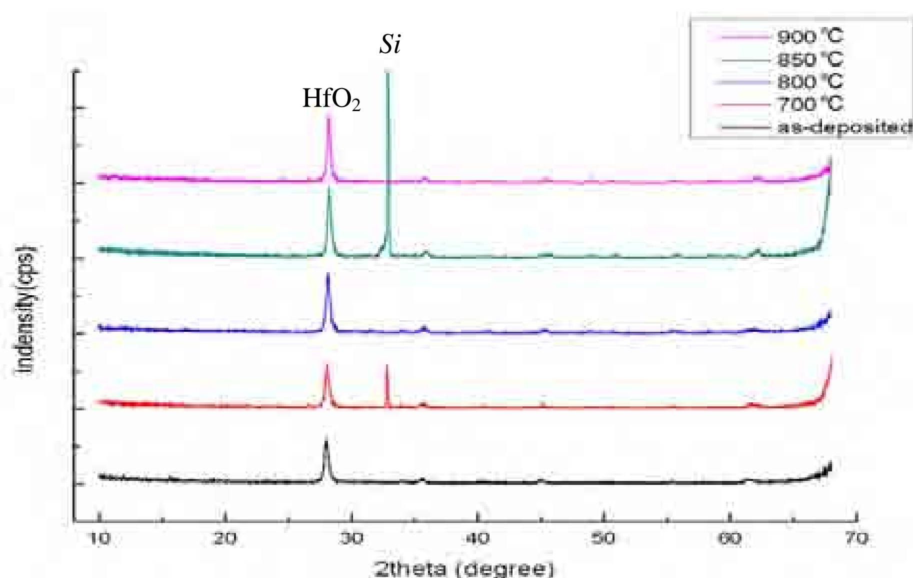

Figure 5.6 - XRD patterns of the deposited HfO_2 films.

For HfO_2 films annealed at 700℃ and 850℃, diffraction peaks corresponding to the (200) crystal plane occurred at 32.82°. But for the other samples the peaks did not appear. This means that the peaks were produced by the Si substrate, not the HfO_2 films. At 69.16° all samples showed strong diffraction peaks corresponding to the (400) crystal plane of the Si substrate.

5.4.3. The Leakage Current of the MIS Capacitor

A SCS4200 semiconductor parameter analyzer (Keithley SCS4200, Keithley Instruments Inc, USA) was employed to measure the leakage current densities of the

MIS capacitors with HfO_2 as dielectric, see Figure 5.7. Annealing temperatures of the deposited HfO_2 layers were 700℃, 800℃, 850℃ and 900℃ respectively.

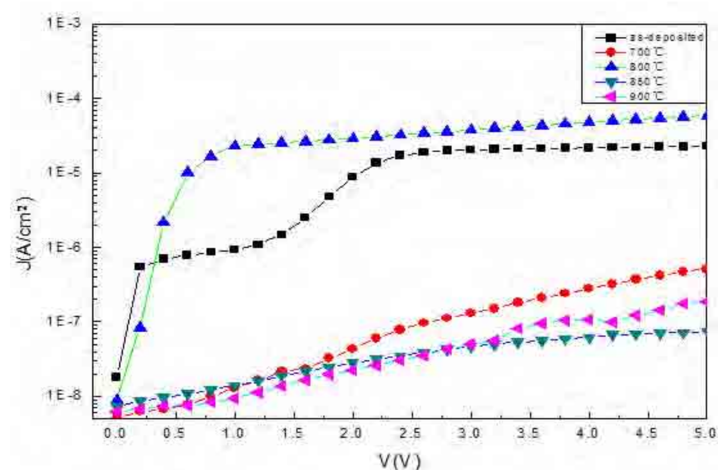

Figure 5.7 - Comparison of leakage current densities of HfO_2 layers.

From Figure 5.7 one can conclude that the leakage current densities of HfO_2 layers annealed at 800℃ and without annealing are larger than those of HfO_2 layers annealed at 700℃, 850℃ and 900℃. The leakage current densities with a voltage of 1V are $0.9\times10^{-6}A/cm^2$ and $2\times10^{-5}A/cm^2$ respectively. Its larger leakage current density suggested that partial crystallization might occur in the HfO_2 layer during the deposition process at 300 ℃. For the HfO_2 layer annealed at 800 ℃, crystallization of amorphous phases also might occur during the annealing process, increasing the leakage current density.

With regard to HfO_2 layers annealed at 700℃, partial crystallization occurred in the film as deposited decreased, effectively increasing insulation and decreasing the leakage current density. For HfO_2 layers annealed at 850℃ and 900℃, the size of crystalline grain increased and crystallization of amorphous phases weakened, decreasing the leakage current density.

5.4.4. The C-V Property of the MIS Capacitor

The C-V properties of the MIS capacitors were measured with a Keithley 590 CV Analyzer (Keithley 590CV, Keithley Instruments Inc, USA). The voltage was 50mV, and the frequency 100kHz, the range of the scanning gate voltage -3V~4V. Figure 5.8 shows C-V properties of the MIS capacitors with HfO_2 films annealed at different temperatures.

The C-V property of the MIS capacitor demonstrated its capacitances and the corresponding applied voltages, and was employed to characterize the dielectric properties of the HfO_2 layer. For a real MIS structure, the C-V property may deviate from that of an ideal MIS capacitor (whose C-V curve is a sigmoid one) because of the charges trapped at the interface and in the oxide layer, as well as the difference of the work functions.

C-V curves of the film which was not annealed (its deposition temperature was about 300℃) and the film which is annealed at 700℃ are nearly sigmoid ones. Using Eq. 5.1 EOT s of the films were obtained as $EOT_{300°C} = 31.38nm$, and $EOT_{700°C} = 24.65nm$, and their dielectric constants were 7.49 and 9.49 respectively. The C-V curve of the film annealed at 800℃ deviates from the ideal one very much and the dielectric constant is so small as to be almost negligible. The C-V curves of the films annealed at 850℃ and 900℃deviates from the sigmoid curve significantly and their dielectric constants can be regarded as being zero.

It is concluded that the dielectric performance was degraded when the annealing temperatures were larger than 700℃, that is, as the annealing temperature increased up to 700℃, the leakage current decreased continuously.

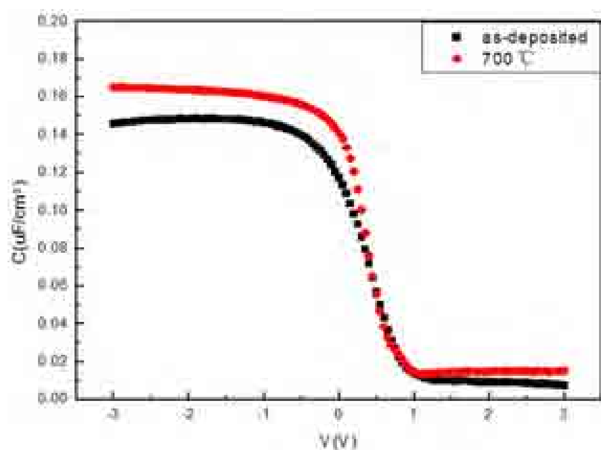

(a) Annealed @ 700℃.

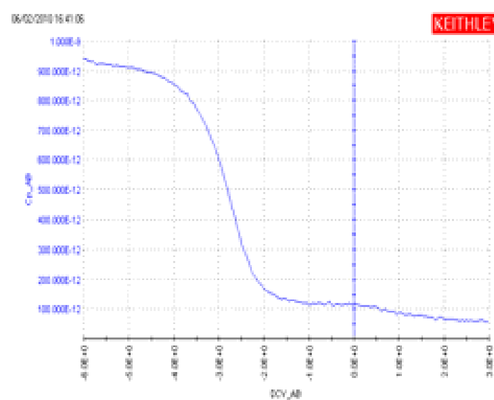

(b) Annealed @ 800℃.

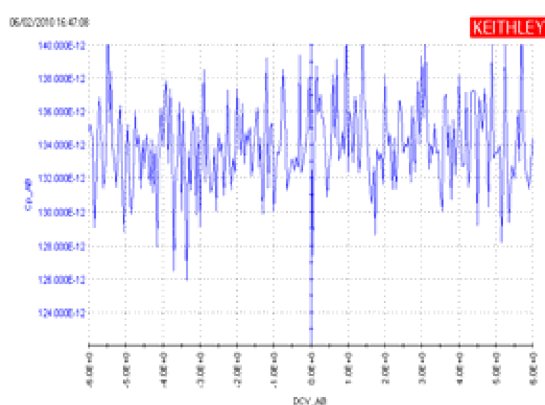

(c) Annealed @ 850℃.

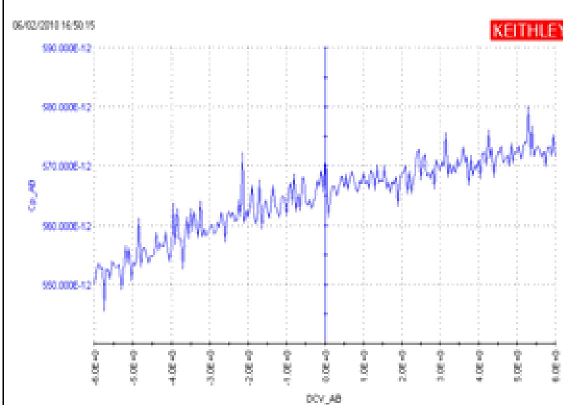

(d) Annealed @ 900℃.

Figure 5.8 - Comparison of C-V properties of HfO_2 films which did and did not undergo the annealing process.

5.5. Nanoroughness Metrology and Characterization of the MIS Capacitor

Surface roughness and interface roughness of the MIS capacitor were measured. Since surface roughness may change during follow-up fabrication processes, more attention was paid to the characterization of the interface roughness at the interfaces Mo/HfO_2 and HfO_2/Si. The surface roughness of every HfO_2 dielectric film was

measured directly with an AFM before depositing the Mo electrode film. For interface roughness of the Mo/HfO_2 and HfO_2/Si interfaces, SEM images of the interfaces were first obtained. Then the images were noise-smoothed and the line edge profiles were extracted according to algorithms introduced in Sections 4.5.2 and 4.5.3 of Chapter 4. Finally LER/LWR of the interfaces was characterized using to the relevant algorithms described in Section 3.2.2 of Chapter 3.

5.5.1. Surface Roughness of the Deposited HfO_2 Dielectric Films

Figure 5.9 shows AFM images of deposited HfO_2 films not annealed and annealed at different temperatures (Nanoscope III, Veeco Instruments Inc., USA).

Surface roughnesses Ra of HfO_2 films were 1.29nm (as deposited), 1.03nm (annealed at 700℃), 0.91nm (annealed at 800℃), 1.28nm (annealed at 850℃) and 0.64nm (annealed at 900℃), and the standard deviation was 0.27nm. The roughness of the HfO_2 film as deposited was high, indicating that the dielectric film quality needed to be improved by annealing. With increasing annealing temperatures, surface roughness first decreased, then started to increase at an annealing temperature 800℃.

For the films annealed at temperatures of 700℃ and 800℃, surface roughness decreases to 1.03nm and 0.91nm, showing the dielectric quality had improved. For dielectric films annealed at 850℃ and 900℃, surface roughness was smaller than that when deposited. Although the surfaces are smoother, crystallization occurred, degrading the quality HfO_2 dielectric significantly.

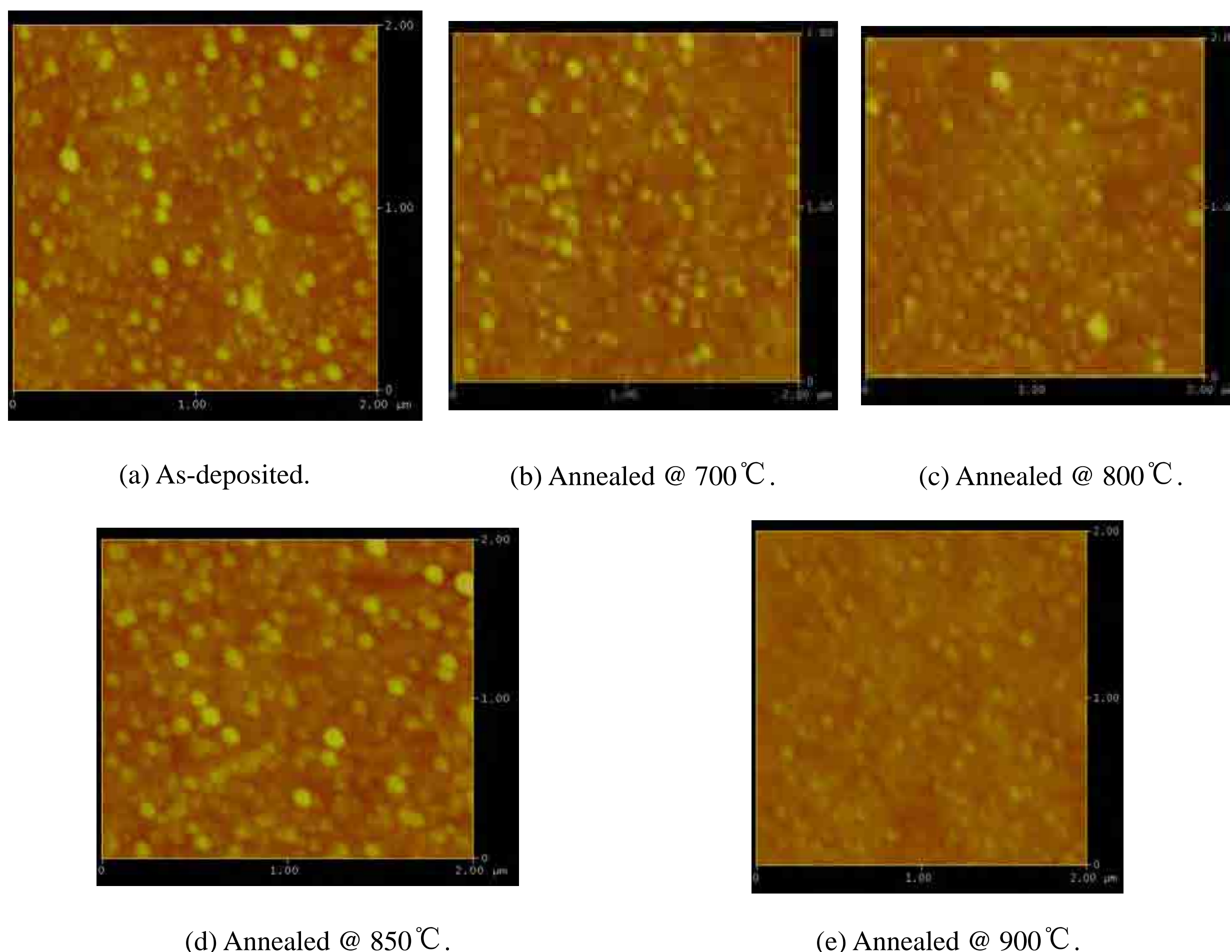

(a) As-deposited. (b) Annealed @ 700℃. (c) Annealed @ 800℃.

(d) Annealed @ 850℃. (e) Annealed @ 900℃.

Figure 5.9 – AFM images of HfO_2 films which were not annealed and annealed at different temperatures.

5.5.2. Interface Roughness at the Mo/HfO_2 and HfO_2/Si Interfaces

Figure 5.10 shows SEM (JSM-6700F, JEOL Ltd., Japan) images of Mo/HfO_2 and HfO_2/Si interfaces. The sample shown in Figure 5.10(a) did not undergo an annealing process, while samples shown in Figure 5.10(b)-(e) were annealed at 700℃, 800℃, 850℃ and 900℃ respectively. The images in Figure 5.10 correspond to the respective AFM images of the dielectric films shown in Figure 5.9. These two kinds of roughness should agree with each other and have similar effects on the MIS capacitor performance. Since cross-sections of the samples were not adjusted perpendicular to the electron beam of the SEM during the SEM measurement process,

the sample tilt culd be evaluated by comparing the thickness measured with the SEM to that measured with the SEME-1000 SE as mentioned in Section 5.4.1 of this chapter.

5.5.2.1. Filtering of the SEM Images

Compared with other filters mentioned in Section 4.5.2 of Chapter 4, a Gaussian filter was selected to smooth the SEM images. Figure 5.11 demonstrates the noise smoothed SEM images that correspond to the images shown in Figure 5.10.

5.5.2.2. Extraction of the Line Edge Profiles

The Canny operator was chosen to detect line edge profiles of filtered SEM images in Figure 5.11 according to the comparison of various extraction operators in Section 4.5.3 of Chapter 4. Extracted line edge profiles of the dielectric HfO_2 films and Mo films are shown in Figures 5.12 and 5.13 respectively.

5.5.2.3. Fitting of the Datum Lines

The detected data were analyzed by the least-squares method, as introduced in Section 4.5.4 of Chapter 4 in order to get datum lines of line edge profiles, and further to characterize corresponding LER/LWRs.

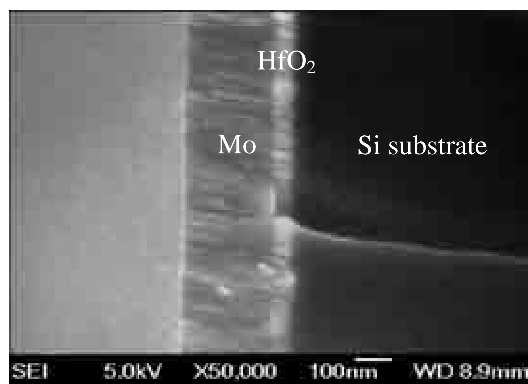

(a) As-deposited.

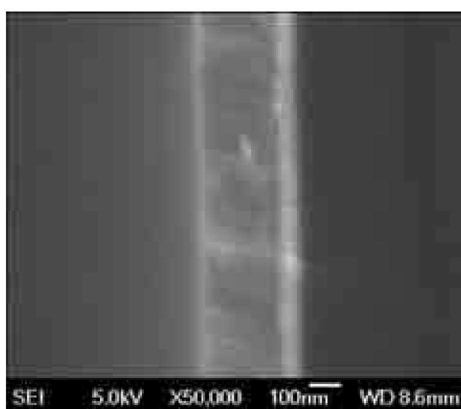

(b) Annealed @ 700℃.

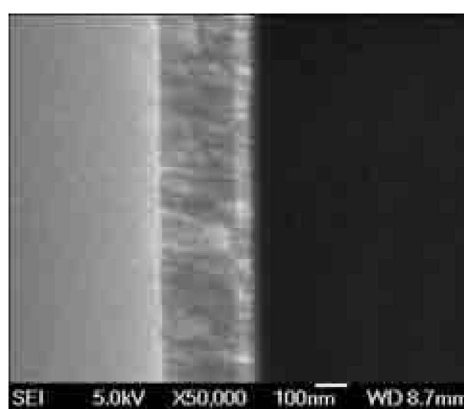

(c)Annealed @ 800℃.

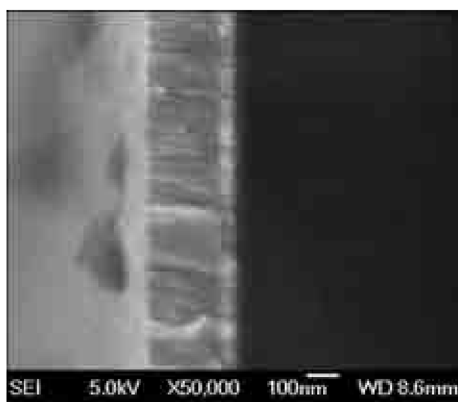

(d) Annealed @ 850℃.

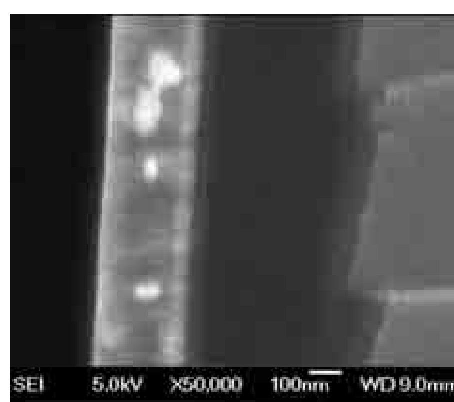

(e) Annealed @ 900℃.

Figure 5.10 - SEM aerial images of the Mo / HfO_2 and HfO_2 / Si interfaces.

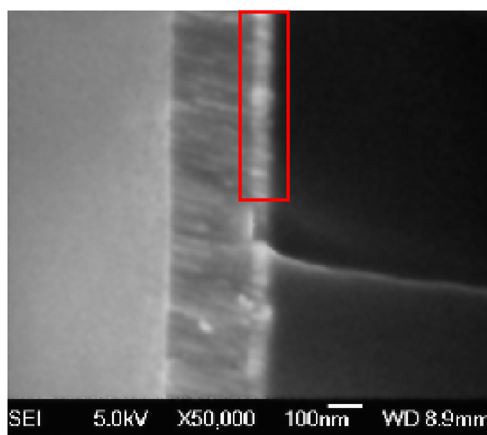

(a) As-deposited.

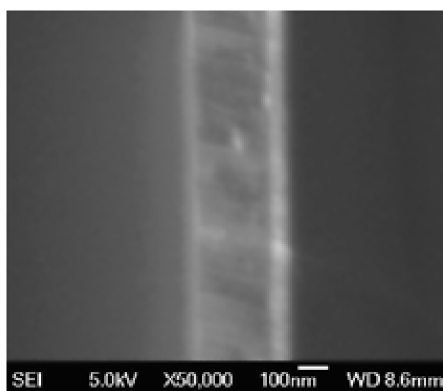

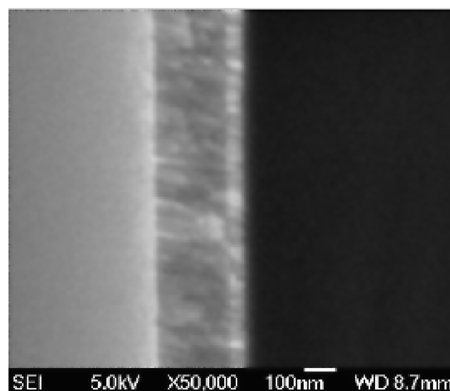

(b) Annealed @ 700℃.

(c)Annealed @ 800℃.

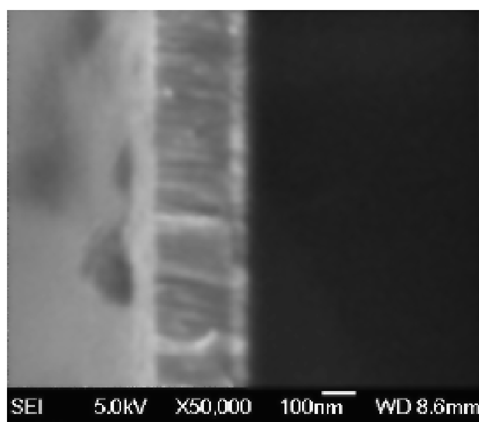

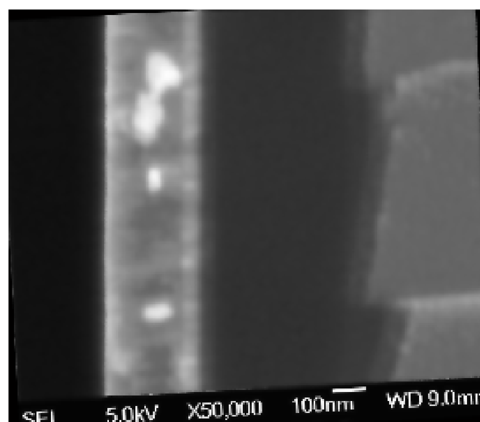

(d) Annealed @ 850℃.

(e) Annealed @ 900℃.

Figure 5.11 - The SEM images filtered with a Gaussian filter.

5.5.2.4. Characterization of Interface Roughness

As introduced in the relevant sections of Chapter 3, the following descriptors were employed to characterize the interface roughness of the MIS capacitor: RMS σ, HHCF and PSD of the line edge profiles.

- **RMS σ**

The descriptor and relevant algorithms introduced in Section 3.2.2.1 of Chapter 3 were employed to characterize LER/LWRs of the extracted line edge profiles demonstrated in Figures 5.12 and 5.13. Corresponding RMS σ_{LER} and σ_{LWR} are shown in Table 5.2.

- **HHCF**

As mentioned in Section 3.2.2.2 of Chapter 3, HHCF was employed to calculate correlation length ξ and to investigate the spatial characteristics of interface roughness of the Mo/HfO_2 and HfO_2/Si interfaces. Figures 5.14 and 5.15 show HHCF curves of line edge profiles of the deposited dielectric HfO_2 and Mo films respectively. Calculated correlation lengths ξ from HHCF curves are shown in Table 5.3.

- **PSD**

As explained in Section 3.2.2.3 in Chapter 3, the PSD was employed to calculate roughness exponents α and to investigate frequency properties of line edge profiles. Figures 5.16 and 5.17 show PSD curves of deposited dielectric HfO_2 and Mo films respectively. Calculated roughness exponents α from OSD curves are shown in Table 5.3.

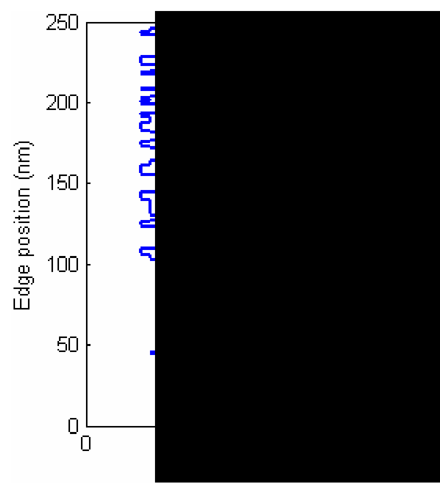

(a) As deposited (within the red box in Fig.5.15).

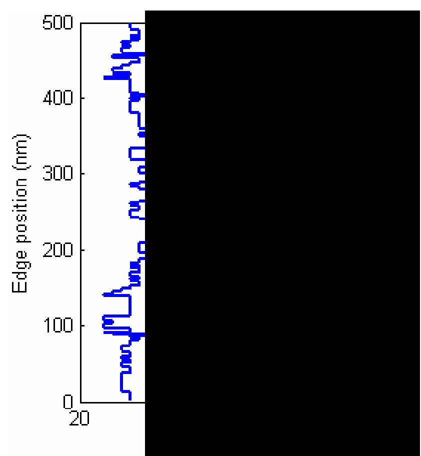

(b) Annealed at 700℃.

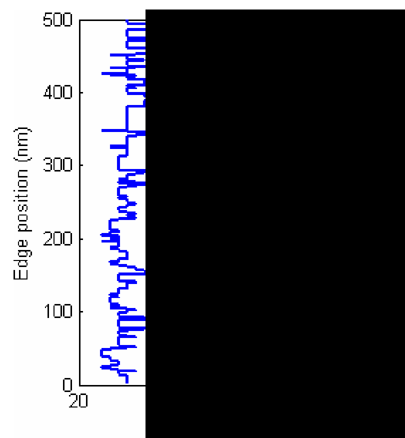

(c) Annealed at 800℃.

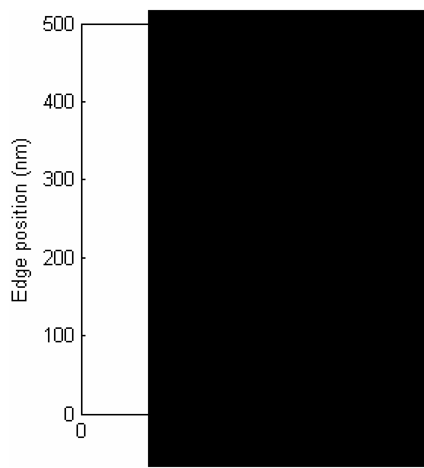

(d) Annealed at 850℃.

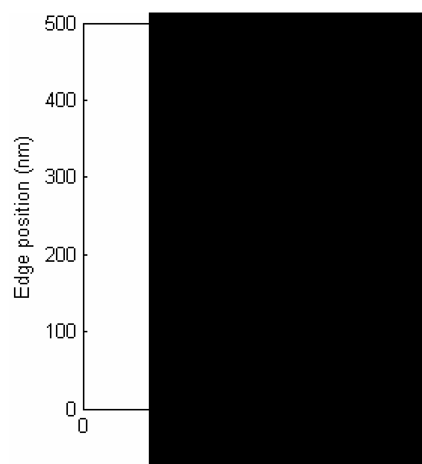

(e) Annealed at 900℃.

Figure 5.12 - Extracted HfO_2 line edge profiles

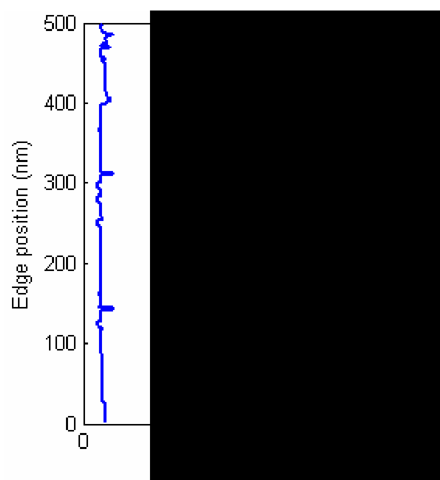

(a) As-deposited.

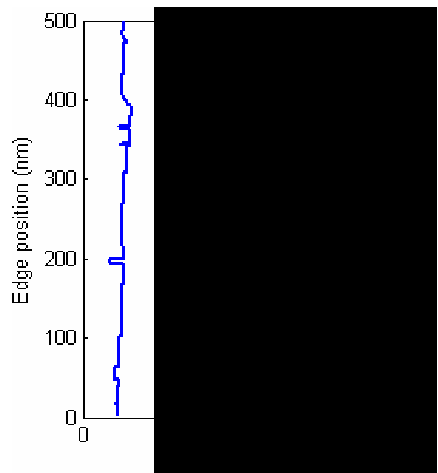

(b) Annealed at 700℃.

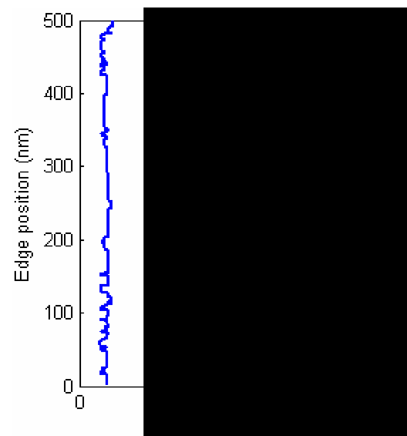

(c) Annealed at 800℃.

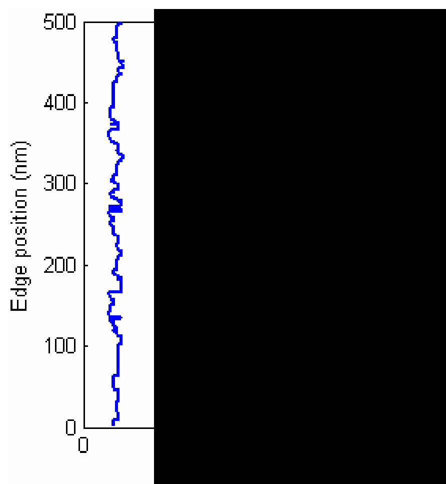

(d) Annealed at 850℃.

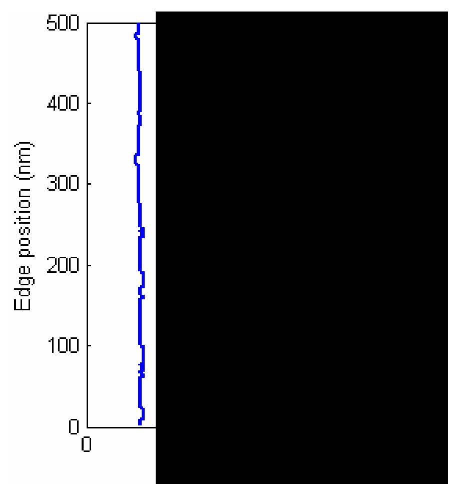

(e) Annealed at 900℃.

Figure 5.13 - Extracted Mo line edge profiles.

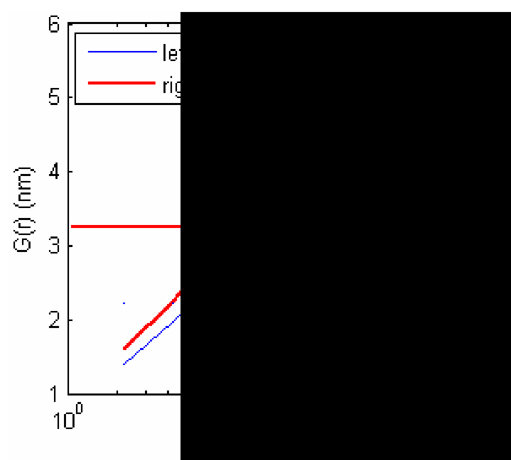

(a) As deposited (within the box marked in red in Fig.5.15).

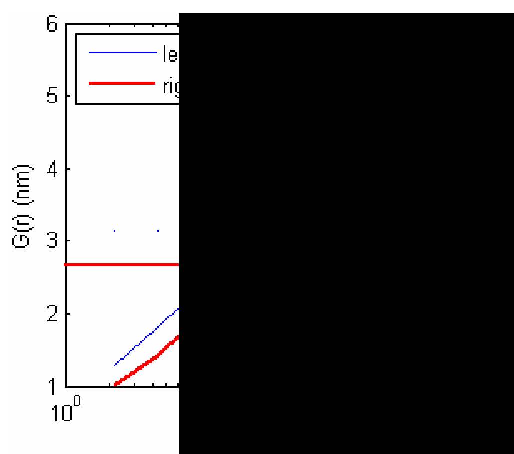

(b) Annealed at 700℃.

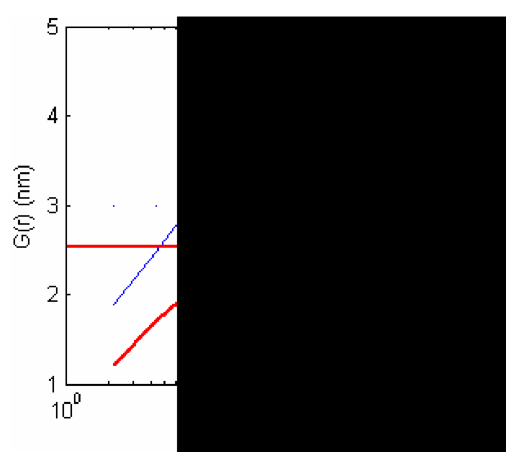

(c) Annealed at 800℃.

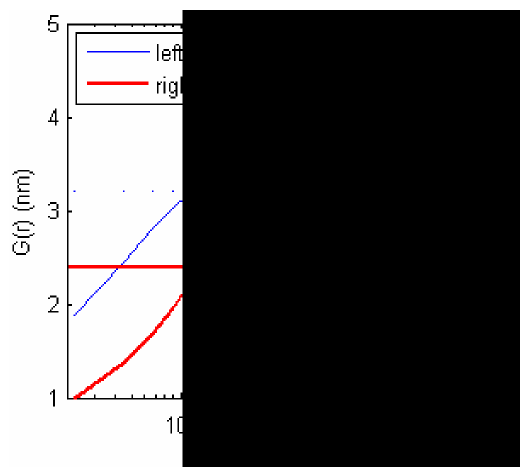

(d) Annealed at 850℃.

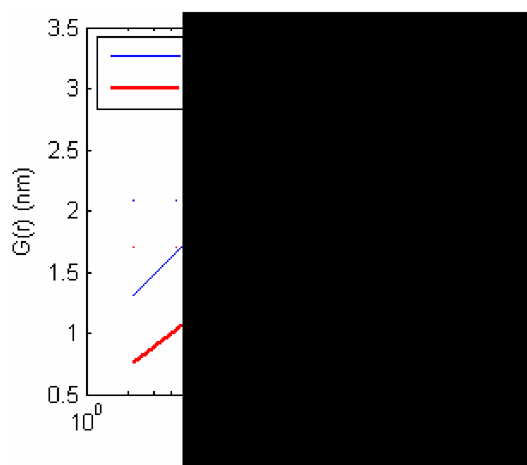

(e) Annealed at 900℃.

Figure 5.14 - HHCF curves of line edges profiles (dielectric HfO_2 films).

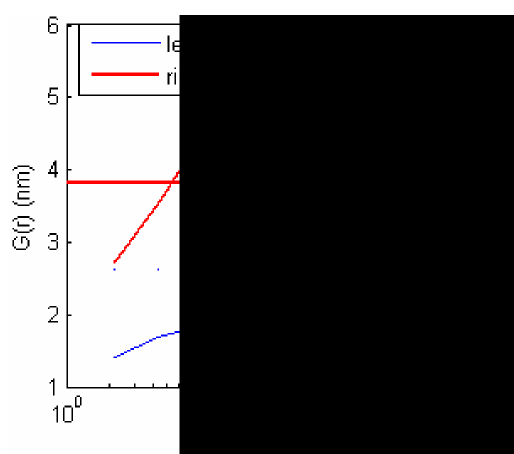

(a) As deposited (within the box marked in red in Fig.5.15).

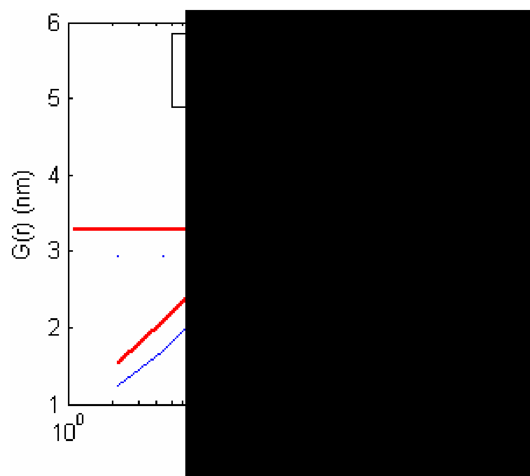

(b) Annealed at 700℃.

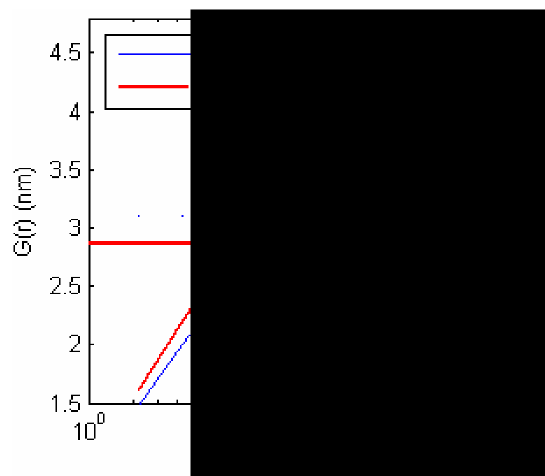

(c) Annealed at 800℃.

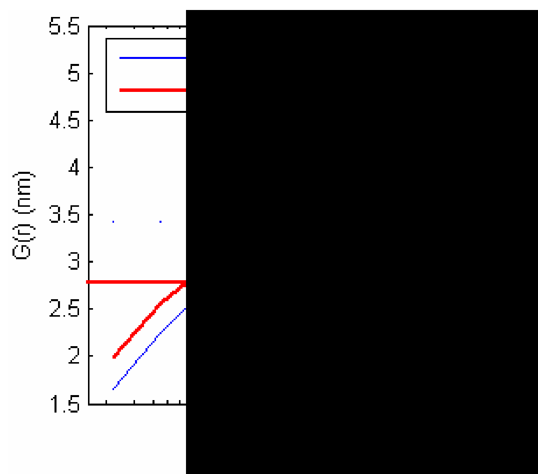

(d) Annealed at 850℃.

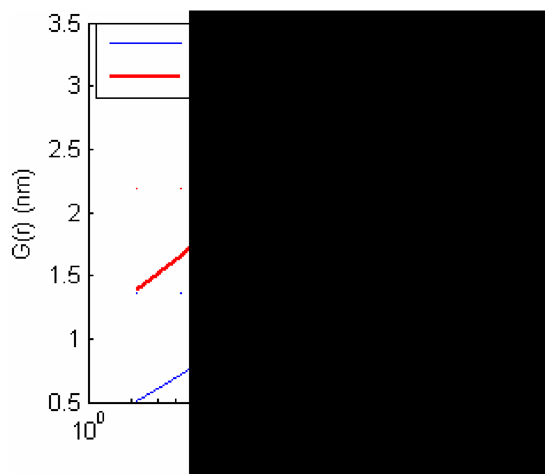

(e) Annealed at 900℃.

Figure 5.15 - HHCF curves of line edges profiles (Mo films).

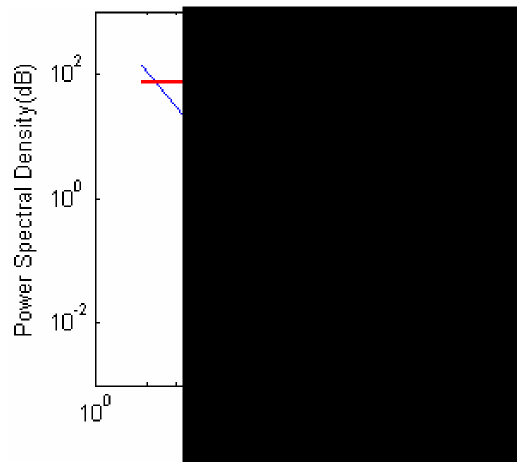

(a) As deposited (within the box marked in red in Fig.5.15).

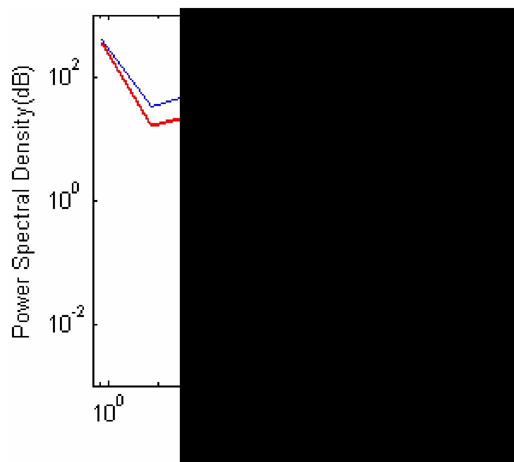

(b) Annealed at 700℃.

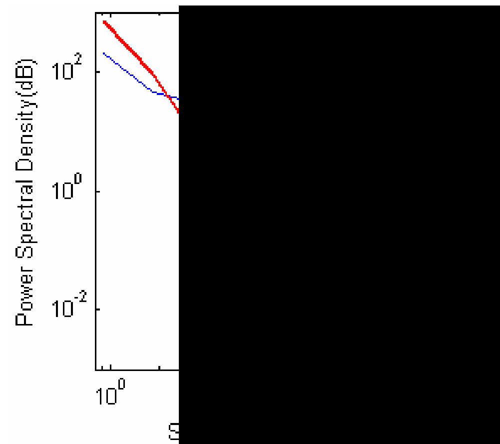

(c) Annealed at 800℃.

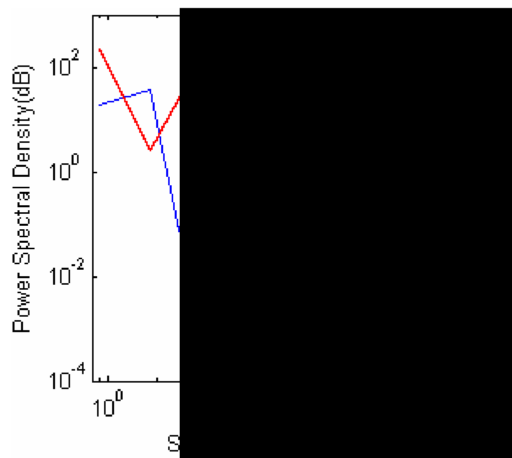

(d) Annealed at 850℃.

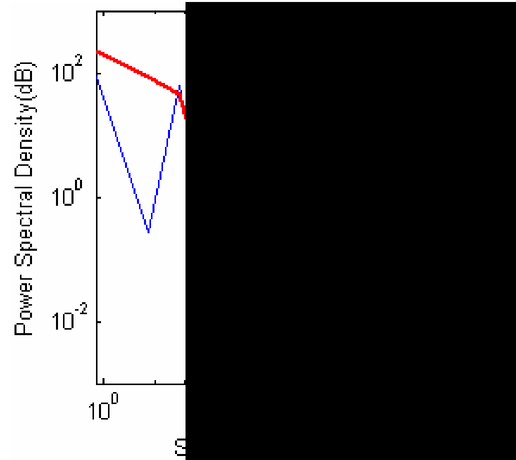

(e) Annealed at 900℃.

Figure 5.16 - PSD curves of line edges profiles (dielectric HfO_2 films).

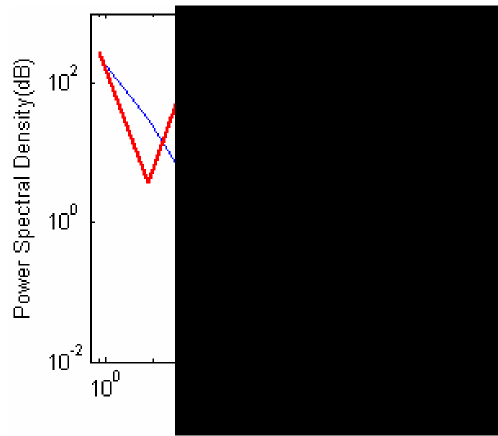

(a) As deposited (within the box marked in red in Fig.5.15).

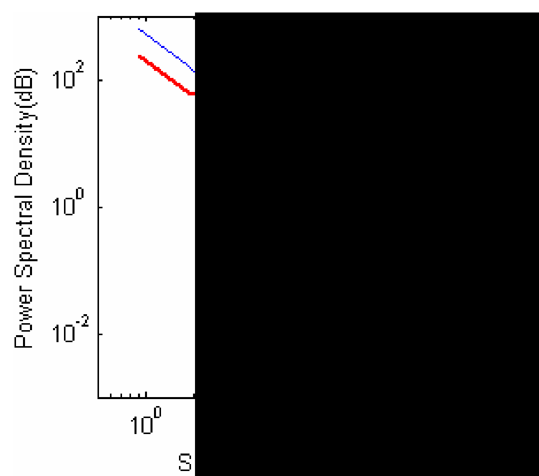

(b) Annealed at 700℃.

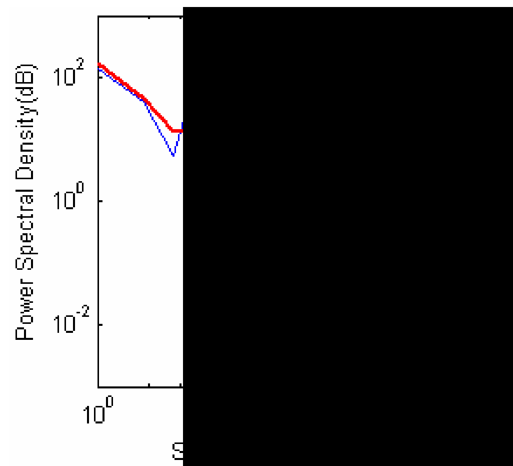

(c) Annealed at 800℃.

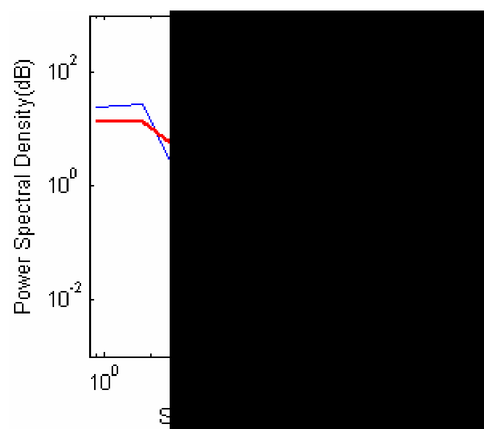

(d) Annealed at 850℃.

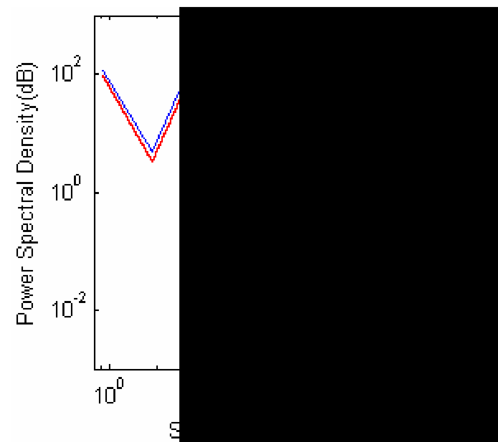

(e) Annealed at 900℃.

Figure 5.17 – PSD curves of line edges profiles (Mo films).

Table 5.2 – Thickness and LER/LWR of HfO_2 and Mo films annealed at different temperatures (unit: nm).

Annealing temperatures and materials		Thickness of the deposited films	Left σ_{LER}	Right σ_{LER}	σ_{LWR}
Annealing temperatures	Materials				
As-deposited	HfO_2	47.98	1.97	2.91	3.48
	Mo	239.42	2.32	3.38	4.49
700℃	HfO_2	52.90	2.80	2.39	3.13
	Mo	243.07	2.61	2.94	3.89
800℃	HfO_2	50.27	2.66	2.25	3.56
	Mo	239.69	2.76	2.55	3.39
850℃	HfO_2	44.48	2.86	2.12	3.43
	Mo	222.69	3.05	2.49	3.99
900℃	HfO_2	47.50	1.86	1.51	2.27
	Mo	218.65	1.21	1.94	2.94

Table 5.3 - Calculated correlation lengths ξ (unit: nm) and roughness exponents α of line edge profiles of dielectric HfO_2 and Mo films.

Annealing temperatures and materials		ξ_{Left}	ξ_{Right}	α_{Left}	α_{Right}
Annealing temperatures	Materials				
As-deposited	HfO_2	5.86	9.79	0.45	0.52
	Mo	46.84	5.46	0.25	0.79
700℃	HfO_2	25.57	24.05	0.35	0.31
	Mo	25.91	16.97	0.33	0.42
800℃	HfO_2	8.20	13.31	0.54	0.36
	Mo	20.90	17.58	0.37	0.37
850℃	HfO_2	11.71	13.72	0.48	0.33
	Mo	15.97	6.99	0.45	0.53
900℃	HfO_2	9.67	20.61	0.32	0.18
	Mo	36.62	11.71	0.37	0.32

5.6. Relationships Between the Performance of the MIS Capacitor, the Surface/Interface Roughness and the Parameters of the Fabrication Process

The calculated thicknesses of HfO_2 films as deposited and annealed at different temperatures is summarized in Table 5.2. The thickness average of the deposited HfO_2 films was found to be 48.63nm, and is significantly less than the nominal thickness of 60nm. There are two reasons which cause the thickness deviation: one is the sample tilt during the SEM characterization, the other is that the fabrication system should be calibrated finely to control the thicknesses of the deposited HfO_2 films by deposition rate and time. The sample tilt was evaluated by comparing the thickness of the HfO_2 film measured with the SEM (48.63nm) with that measured with the SEME-1000 SE (61.2nm); the resulting tilt was 37.39°.

Table 5.4 - Relationships of the annealing temperature, the surface roughness and the leakage current densities of the deposited HfO_2 dielectric films.

Annealing temperature(℃)	as deposited	700℃	800℃	850℃	900℃
Surface roughness Ra(nm)	1.29	1.03	0.91	1.28	0.64
Leakage current density at 1V(A/cm^2)	0.9×10^{-6}	1.3×10^{-8}	2×10^{-5}	1.3×10^{-8}	0.8×10^{-8}

Table 5.4 shows the relationships between the annealing temperatures, the surface roughness and the leakage current densities. , The surface roughness of the HfO_2 film decreased with increasing annealing temperature, meaning the phase structures of the films must have changed too. But the leakage current densities of the samples annealed at 700℃, 850℃ and 900℃ were smaller than that of the sample as

deposited, while the surface roughness of the samples annealed at 850℃ was larger than for the sample as deposited, meaning that the samples annealed at 700℃ and 900℃ were acceptable. Since the above mentioned surface roughnesses were all measured with the AFM, during the fabrication flow, they are subject to changes caused by the follow-up fabrication processes. The C-V property measurements and the interface roughness were introduced to select a favorable annealing temperature. Table 5.5 is selected from Table 5.2. From Table 5.5 it is concluded that the LWR of the HfO_2 sample annealed at 700℃ is significantly less than that of the sample as deposited, that is, annealing at 700℃ improves the sample quality. This is consistent with the leakage current densities of HfO_2 films shown in Figure 5.7 and the C-V property in Figure 5.8. Although the LWR of HfO_2 sample annealed at 900℃ is less than and agrees with the leakage current densities in Figure 5.7, its C-V property in Figure 5.8 is not good, meaning a breakdown might occur at a local position on the MIS capacitor. Taking the former conclusions into consideration, one can conclude that the preferred annealing temperature is 700℃.

Table 5.5 - LER/LWR (unit: nm) of HfO_2 films annealed at different temperatures.

Annealing temperatures	Left $\sigma_{LER}(Mo/HfO_2)$	Right $\sigma_{LER}(HfO_2/Si)$	σ_{LWR}
As-deposited	1.97	2.91	3.48
700℃	2.80	2.37	3.13
800℃	2.66	2.25	3.56
850℃	2.86	2.12	3.43
900℃	1.86	1.51	2.27

Table 5.5 also shows that the left LERs of annealed HfO_2 samples are all larger than the right ones, demonstrating that the HfO_2/Si interface is better than the Mo/HfO_2 interface thanks to the contribution of the surface quality of the Si substrate during the annealing process. This conclusion was supported by the calculated correlation lengths ξ and roughness exponents α of the line edge profiles of the dielectric HfO_2 films shown in Table 5.6.

Table 5.6 is part of Table 5.3. In Table 5.6 correlation lengths ξ of the right line edge profiles were all larger than those of the left line edge profiles, meaning there are less high frequency components in right line edge profiles than in left ones, and the right line edge profiles are smoother than the left ones. Also correlation lengths ξ of the samples annealed at 700℃ were larger than those of the other samples: as deposited and annealed at 800℃, 850℃ as well as 900℃. This shows that an annealing temperature 700℃ is more effective for improving the deposited HfO_2 film quality. Roughness exponents α of the samples also support this conclusion.

Table 5.6 - Correlation length ξ (unit: nm) and roughness exponent α of line edge profiles of HfO_2 films.

Annealing temperatures	ξ_{Left}	ξ_{Right}	α_{Left}	α_{Right}
As-deposited	5.86	9.79	0.45	0.52
700℃	25.57	24.05	0.35	0.31
800℃	8.20	13.31	0.54	0.36
850℃	11.71	13.72	0.48	0.33
900℃	9.67	20.61	0.32	0.18

5.7. Summary

In this chapter MIS capacitors with HfO_2 as the high k dielectric films of 60 nm nominal thickness and Mo with dimensions of 1x1 mm, as upper electrodes, were introduced and fabricated. Spectroscopic ellipsometry was used to measure the thickness of the deposited HfO_2 film (61.2nm) , which was employed to evaluate the tilt of the sample during the SEM measurement process (about 37.39°). XRD was used to characterize the phase structures of the deposited HfO_2 films. Then the leakage current density and the C-V property of the MIS capacitor were measured, demonstrating that the optimal annealing temperature was 700℃. Surface and interface roughness of the deposited HfO_2 films and the MIS capacitors were measured with an AFM and SEM respectively. Characterization of relevant roughness by RMS σ, correlation length ξ and roughness exponent α shows that 700℃ is the optimal annealing temperature, which can improve the quality of the deposited HfO_2 film and, hence, that of the MIS capacitor. The conclusions demonstrate that the direct relationships between the MIS capacitor performance and the roughness characteristics, as a result of fabrication, can be taken as a reference in regulating the corresponding fabrication process, hence improving the quality of the MIS capacitor. This approach can be introduced to the quality control of other nanodevices.

CHAPTER 6

UNCERTAINTY EVALUATION OF NANOROUGHNESS MEASUREMENTS

6.1. Introduction

In metrology, a measurement process without uncertainty evaluation is incomplete. The same applies to nanoroughness metrology. The new framework of uncertainty was introduced in the relevant chapters of the 2007-version Metrology of International Technology Roadmap for Semiconductors (ITRS), requiring a complete measurement expression including measured value plus a corresponding uncertainty[6.1]. In previous chapters nanoroughness measurement and its effects on the properties of specified nanostructures and nanodevices were discussed without considering the uncertainties in the raw data. However, raw data have measurement uncertainties that affect the measurement result of nanoroughness. This chapter presents an investigation of the uncertainty of nanoroughness SEM measurements, following the requirements of the related ISO Geometric Product Specification and Verification(GPS) [6.2,6.3] and the Guide to the Expression of Uncertainty in Measurement (GUM)[6.4].

The chapter begins with an introduction to the theoretical fundamentals of measurement uncertainty, followed by an uncertainty model of SEM-based nanoroughness measurement. It then continues with a discussion of uncertainty evaluation of SEM-based LER/LWR metrology, including identification of SEM uncertainty sources for nanoroughness measurement, evaluation of SEM measurement uncertainty, an evaluation model for standard measurement uncertainty, evaluation of standard measurement uncertainty and uncertainty evaluation for SEM image preprocessing. The chapter proceeds to uncertainty estimation for SEM image processing. The uncertainties introduced by sampling length, SEM image noise and a median line of least-squares fit are then investigated. Section 6 of the chapter gives a case study, showing the fabrication of a nanoscale grating structure and the evaluation of total uncertainty for LER measurement. The chapter finishes with a summary.

6.2. Theoretical Fundamentals of Measurement Uncertainty

Because the understanding and expression for uncertainty were much different and lacking in consistency, in 1980 a BIPM work group proposed the International Recommendation INC-1: Expression of Experimental Uncertainties[6.5]. In 1986 “Evaluation of measurement data — Guide to the expression of uncertainty in measurement” was proposed by ISO and other international organizations[6.6]. In 1993 the guide was issued by ISO and then widely implemented all over the world [6.4].

6.2.1. Definition of Measurement Uncertainty

According to GUM, the definition of uncertainty is a parameter, fitted with the result

of a measurement that characterizes the dispersion of the values that could reasonably be attributed to the measurand. The expression of a measurement result of a measurand Y is expressed as Eq. 6.1.

$$y \pm U \qquad (6.1)$$

Where y is the estimate of the measurand Y

U is the measurement uncertainty of the estimate y.

This expression includes an estimate and its scatter, meaning not a specified value but an interval within which the probable value falls.

6.2.2. Evaluation of Standard Uncertainty

The definition of a standard uncertainty is the uncertainty which is characterized with a standard deviation, denoted by u; the uncertainty in a given component is denoted by u_i. There are two kinds of evaluations of standard uncertainty: type A and type B evaluations[6.4].

6.2.2.1. Type A-Evaluation of Standard Uncertainty

Type A evaluation of standard uncertainty u is processed by a statistical method. The value of its uncertainty is equal to that of the standard deviation σ of a set of the observed values, that is

$$u = \sigma \qquad (6.2)$$

When the quantity of a measurand Y is determined by observed values X_1, X_2, …, X_N, the standard uncertainty u_y of the estimate y of the measurand Y is determined by the standard uncertainty u_{xi} of the estimate x_i of the measurand X_i. Hence the standard uncertainty u_{xi} of x_i should be evaluated first. The evaluation

process is described below: with other values of X_j ($j \neq i$) constant, when X_i is observed n times under equally accurate measurement condition. Then the standard deviation σ_i is derived from the n observations with Bessel's correction [6.7],

$$\sigma_i = \sqrt{\frac{\sum_{i=1}^{n} \upsilon_i^2}{n-1}} \qquad (6.3)$$

Where υ_i is the residual error of the ith observation.

Eventually the standard uncertainty u_{xi} of the estimate x_i will be determined as below: if the single measured value is used as the estimate x_i of the measurand X_i,

$$u_{xi} = \sigma_i \qquad (6.4)$$

if an average value is used as the estimate x_i of the measurand X_i,

$$u_{xi} = \sigma_i / \sqrt{n} \qquad (6.5)$$

6.2.2.2. Type B-Evaluation of Standard Uncertainty

Methods other than statistics are used for type B evaluation of a standard uncertainty. Type B evaluation plays an important role in evaluating specific uncertainties which cannot be evaluated by statistical methods, or can be but the cost is very high. That is why type B evaluation is now being widely used [6.8].

Type B evaluation of the standard uncertainty u_x of the estimate x of the measurand X is determined from a range of relevant information, such as old measurement data, experience and technical documents, general knowledge of relevant instrument or apparatus, data supplied by a verification certificate, instruction book and other reports, reference data in handbooks, etc. Some experience and an understanding of the principles involved are required in order to properly evaluate

type B uncertainty.

In order to evaluate type B uncertainty, the form of the distribution of measured values (for example, a normal distribution) must be assumed. Then the uncertainty is calculated as described below[6.4]:

a) If the estimate x is affected by various independent factors and their effects are approximate, the distribution can be supposed to be normal. The uncertainty is estimated from:

$$u_k = \frac{a}{k_p} \quad (6.6)$$

Where P is the probability level

a is the half width of the probability level P

k_p is the coverage factor

b) If an estimate x is determined from technical documents and the measurement uncertainty U_x is equal to k times the standard deviation, its standard uncertainty is determined from equation 6.7:

$$u_k = \frac{U_k}{k} \quad (6.7)$$

c) If the probability that an estimate x falls within an interval $(x-a, x+a)$ is 1 and the occurrence probability at any position within the range is same, the estimate x describes a uniform distribution. The standard uncertainty can be determined by equation 6.8:

$$u_k = \frac{a}{\sqrt{3}} \quad (6.8)$$

d) If an estimate x is affected by two independent factors which follow a uniform

distribution, the estimate x has a triangular distribution within an interval $(x-a, x+a)$. Its standard uncertainty is expressed as in equation 6.9:

$$u_k = \frac{a}{\sqrt{6}} \tag{6.9}$$

e) If an estimate x complies with arc-sine distribution within an interval $(x-a, x+a)$, the standard uncertainty is:

$$u_k = \frac{a}{\sqrt{2}} \tag{6.10}$$

6.2.3. Combination of Measurement Uncertainties

6.2.3.1. Combined Standard Uncertainty

If a measurement result is affected by various factors which produce corresponding uncertainty components, the standard uncertainty of a measurement result is expressed by a combined standard uncertainty u_c which represents a combination of the above mentioned uncertainty components. In order to calculate u_c the relationship between the measurement result and various affecting factors is firstly determined so that uncertainty components can be evaluated accurately. Then the combination of a standard uncertainty can be derived.

In an indirect measurement process, the estimate y of a measurand Y is calculated from other observed values $x_1, x_2, ..., x_N$ as in equation 6.11:

$$y = f(x_1, x_2, ..., x_N) \tag{6.11}$$

Suppose the measurement standard uncertainty of the observed value x_i is u_{xi}. Then the standard uncertainty component of the measurand y caused by x_i is:

$$u_i = \left|\frac{\partial f}{\partial x_i}\right| u_{xi} \tag{6.12}$$

But the uncertainty u_y of the measurement result y should be combined with all the uncertainty components; u_c denotes this kind of uncertainty and is given by.

$$u_c = \sqrt{\sum_{i=1}^{N}\left(\frac{\partial f}{\partial x_i}\right)^2 (u_{xi})^2 + 2\sum_{1\le i<j}^{N}\frac{\partial f}{\partial x_i}\frac{\partial f}{\partial x_j}\rho_{ij}u_{xi}u_{xj}} \tag{6.13}$$

Where ρ_{ij} is the correlation coefficient of every two direct measurands x_i and x_j.

6.2.3.2. Expanded Uncertainty

Only with the standard deviation can combined standard uncertainty describe measurement uncertainty and the probability that the measurement result $y \pm u_c$ includes the true value is 68% [6.9]. For circumstances requiring a high level of confidence, the expanded uncertainty is needed to describe measurement uncertainty. Expanded uncertainty, *U*, is equal to combined standard uncertainty u_c multiplied by the coverage factor k as shown in Eq. 6.14[6.4].

$$U = ku_c \tag{6.14}$$

If expanded uncertainty is regarded as measurement uncertainty, this measurement result is expressed as:

$$Y = y \pm U \tag{6.15}$$

The coverage factor k is determined by the threshold of the t-distribution $t_p(\nu)$

$$k = t_p(\nu) \tag{6.16}$$

Where ν is the degree of freedom of the combined standard u_c.

Usually the coverage factor k is selected from the range 2~3[6.9].

6.3. Uncertainty Propagation Model of SEM-based Nanoroughness Measurement

6.3.1. SEM-based Nanoroughness Measurement Process

Figure 6.1 shows a SEM-based nanoroughness measurement process. When SEM is employed to measure nanoroughness of nanostructures and nanodevices, not only the instruments but also the following nanoroughness evaluation operations will produce measurement uncertainties.

6.3.2. Preprocessing of SEM Images

According to the rules of operators and operations in ISO GPS [6.2, 6.10], the preprocessing of SEM images mainly includes the operations of extraction, filtering and fit, etc. These operations consist of a complete preprocess operators as shown in Figure 6.2.

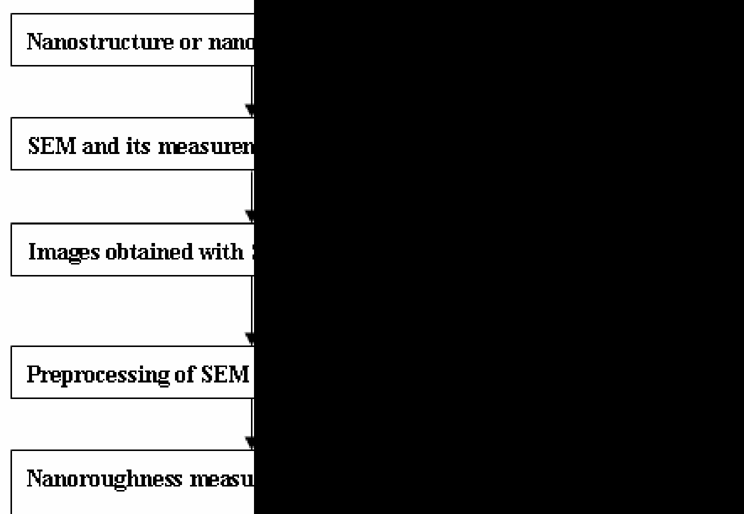

Figure 6.1-SEM-based nanoroughness measurement process.

6.3.2.1. Noise-smoothing

If SEM is used for nanoroughness metrology, noise will be introduced into images and should be eliminated for subsequent evaluation. But when the filtering operation is employed for noise-smoothing, a line edge position will be changed [6.11]. Figure

6.3 demonstrates the positional deviation of points along a line edge before and after filtering, which produces errors of line edge position or linewidth and consequently affects the line edge roughness and line width roughess(LER/LWR) evaluation.

6.3.2.2. Extraction Operation

Extraction is defined as an operation to obtain a limited set of points along nanograting lines according to specific rules.

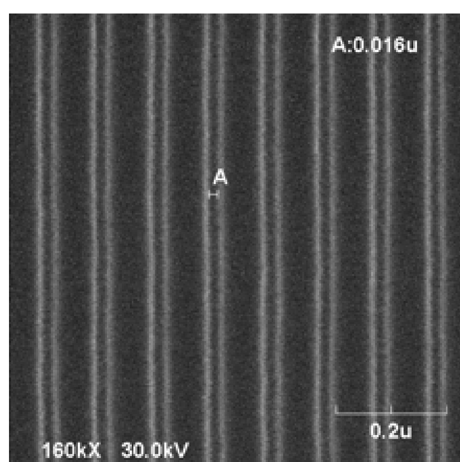

(a) SEM image from above.

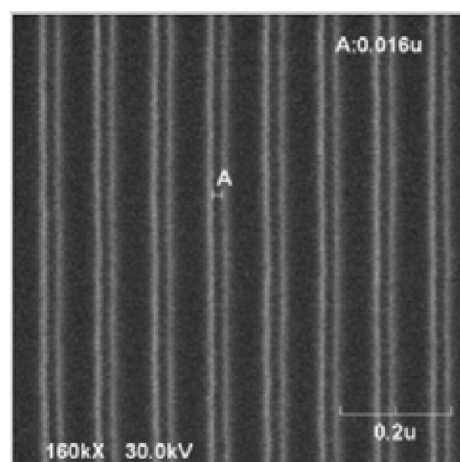

(b) After filtering by the Gaussian filter.

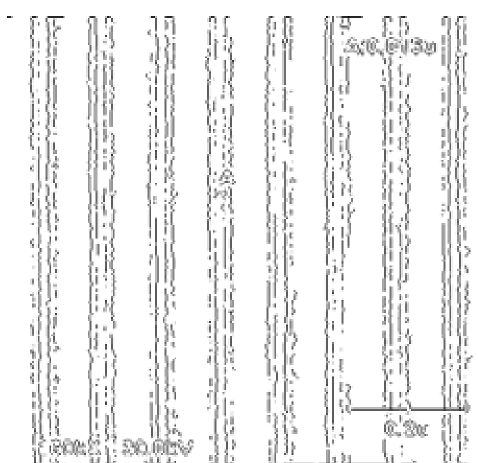

(c) After extraction by Canny edge detector.

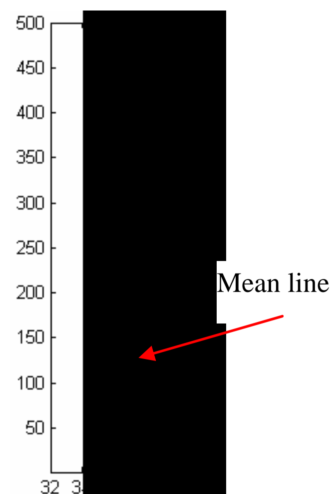

(d) After fitting by the least squares fit.

Figure 6.2-SEM image preprocessing for nanoroughness metrology.

In extraction operation, sampling length and sampling interval are two important

parameters which affect significantly LER/LWR measurement results. Figure 6-4 shows that LER/LWR will be different as sampling length and sampling interval change. It shows that sampling length and sampling interval are two major influences on nanoroughness metrology uncertainties. In the literature[6.12,6.13] it was concluded that a sampling interval less than 10 nm had less effect on the measurement precision of LER/LWR than other parameters, and so in this case could be neglected. Therefore, in this thesis, only the effect of sampling length on the extraction operation for nanoroughness measurements will be investigated.

6.3.2.3. Fit Operation

Figure 6-2 (d) shows a least-squares reference line which was fitted from an extracted line edge according to least-square criterion. The fitted least-square reference line is the approximate substitution of a real line edge profile, so fit criterion is another influential factor in the uncertainty of nanoroughness measurement.

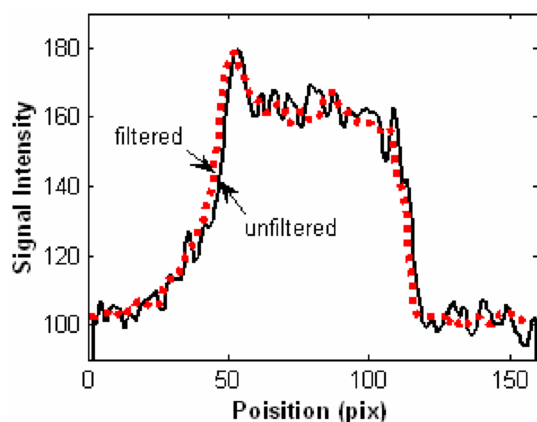

Figure 6.3-Filtration operation changes the profile and position of a line edge.

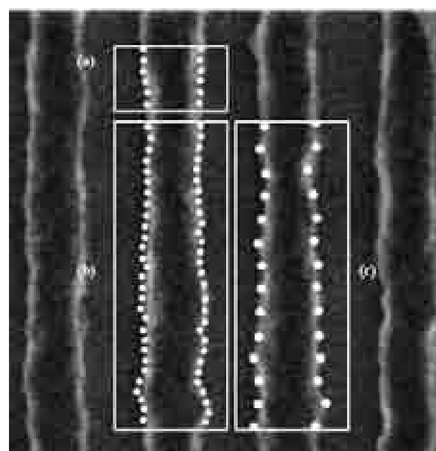

Figure 6.4-Effects of sampling length and sampling interval on values of LER/LWR [6.13].

6.3.3. Uncertainty Propagation Model of Nanoroughness Measurement

According to analysis above, the uncertainty propagation model of SEM-based nanoroughness measurement can be demonstrated in Figure 6-5. In ISO GPS[6.2], implementation uncertainty includes the uncertainties produced by the factors such as the measurement instrument, operating staff, environmental conditions etc., and is denoted by u_1 . This uncertainty will be superimposed on SEM images and propagates to subsequent operations via the extraction operation.

During SEM image preprocessing, extraction, filtering and fit are three key operations which affect nanoroughness measurement results significantly, and the corresponding uncertainties are regarded as method uncertainty.

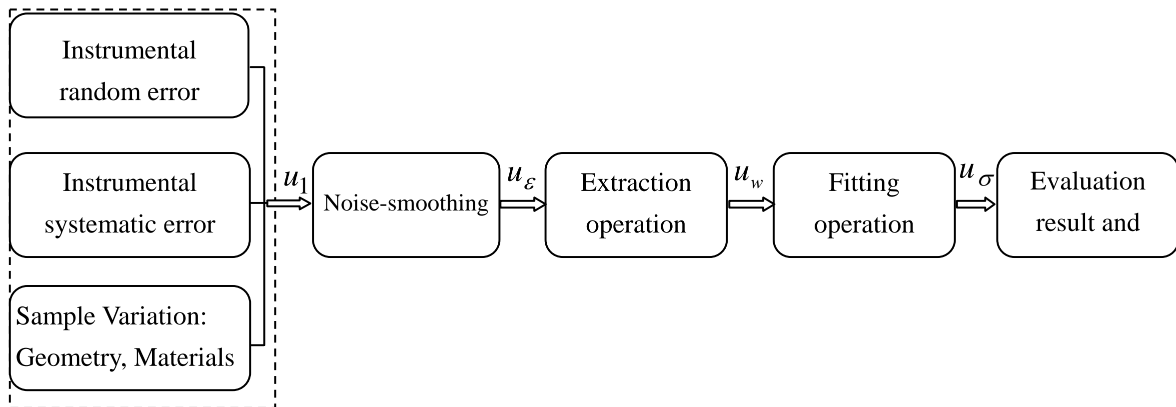

Figure 6.5-Uncertainty propagation model of SEM-based LER/LWR measurement.

Suppose every two uncertainty factors mentioned above are non-correlated, then according to the uncertainty combination equation presented in ISO GUM[6.4] the total uncertainty of SEM-based LER/LWR metrology can be derived from

$$u_c = \sqrt{u_1^2 + u_w^2 + u_\varepsilon^2 + u_\sigma^2} \tag{6.17}$$

Where u_w is the extraction operation

u_ε is the filtration operation

u_σ is the fit operation

6.4. Evaluation of Uncertainties Produced by SEM Instrument

SEM is one of the most popular instruments nowadays for nanoroughness measurement in the nanometrology community [6.14-6.16]. The SEM first focuses an electron beam whose cross-sectional radius is very small (5-7nm) and then scans a sample in a raster way, producing information which is related to the properties of the sample. The SEM collects and processes this information to form a magnified image of the surface. The characteristics of SEM are its speedy image formation (faster than scanning probe microscopy and a stylus profiler), high resolution (0.5nm) ; thus it is always employed to characterize LER/LWR. Because an SEM image is formed from the interaction of incident electrons and a sample material, there are several factors which contribute to uncertainties in the precision of nanoroughness measurements. These factors include the wave character of incident electrons, magnification, scanning speed and resolution, etc. In this chapter the uncertainty of nanoroughness measurement produced by SEM will be investigated and evaluated.

6.4.1. Identification of SEM-based Uncertainty Sources

When SEM is used for nanoroughness measurement, there are two kinds of uncertainty sources: one is from the measurement instrument (including measurement conditions), the other from the sample to be measured [6.17]. The following factors and relevant uncertainty are identified from the first kind of sources: SEM resolution and its related uncertainty, stability of SEM magnification and its uncertainty,

aberration of the SEM image and its uncertainty, image processing and its uncertainty, variation of SEM working distance and its uncertainty, and secondary electron image-forming principle and corresponding uncertainty. From the second kind of sources, the following factors and relevant uncertainties can be identified: the calibrator and its uncertainty, sample deformation and relevant uncertainty, sample surface tilt and the corresponding uncertainty. The following sections of this chapter are to investigate above mentioned uncertainties according to ISO GUM[6.4].

6.4.2. Analysis of SEM-based Uncertainty Sources

6.4.2.1. Uncertainty Produced by SEM Resolution

SEM resolution is determined by SEM performance and its condition after debugging [6.18]. Resolution means the smallest distance between two points which the SEM can resolve[6.13]. Within this distance is a blurry zone. An "aiming uncertainty" will be introduced by the blurry zone for subsequent image measurement[6.19]. In this chapter 'd' denotes SEM resolutio*n.*

6.4.2.2. Uncertainty Introduced by SEM Enlarged Image Measurement

This kind of uncertainty is related to magnification, resolution of the image and the measurement method[6.20]. Magnification which is not large enough will produce a larger uncertainty in the process of measurement. The range of SEM magnification is large (20X-200,000X) and so this kind of uncertainty can be eliminated by increasing the magnification. Usually a high precision instrument is needed for nanoroughness metrology. In this case, the uncertainty produced by the measurement method can be eliminated because of low precision. So it can be concluded that the uncertainty of

SEM image measurement is introduced mainly by the aiming process. Suppose M denotes image magnification, then image resolution will be Md and the largest deviation is half the blurry zone($\frac{1}{2}Md$). Further suppose the distribution is a Gaussain one, then the aiming uncertainty is derived as $\frac{1}{3}\times\frac{1}{2}Md=\frac{1}{6}Md$.

6.4.2.3. Uncertainty arising from Stability of SEM Magnification

SEM magnification is affected by the accelerating voltage of the electron beam and the current through the scanning coils [6.21]. If these factors vary, the magnification times change too. If the SEM magnification for the image of a calibrator is different from that of a sample, it will introduce a corresponding uncertainty. Nowadays SEM stability has improved greatly and the variation of magnification decreased dramatically[6.22]. As a result, the uncertainty caused by the stability of the SEM magnification may be kept so low that it is insignificant.

6.4.2.4. Uncertainty arising from Aberration of the SEM image

The aberration of an SEM image is defined as the difference between the form of the SEM image and that of the sample[6.22]. From the view point of SEM magnification, the aberration can be regarded as different magnifications in different regions of an image and in different directions. For example if the magnifications in the x and y direction are different, the central and edge zones of a SEM image will be different from the corresponding parts of a real sample.

In the modern SEM instrument the aberration of the image is very small [6.23]. So in this chapter we suppose that the operation process can eliminate the uncertainty caused by aberration of the SEM image.

6.4.2.5. Uncertainty caused by Secondary Electron Formation

The uncertainty produced by secondary electron image formation mainly depend on the sample to be measured. Section 2.6.1 in Chapter 2 described it in detail. Here β denotes the uncertainty caused by secondary electron image formation. It is noted that for nanoroughness metrology the uncertainty produced by secondary electron image formation should be eliminated as far as possible. If negative, it should be evaluated properly and combined into the total uncertainty of the nanoroughness measurement.

6.4.2.6. Uncertainty caused by the Variation of SEM Working Distance

According to the principles of SEM, the magnification is related to its working distance. If the working distance between a sample and a calibrator varies, the apparent magnification changes, producing uncertainty in the SEM working distance. In this thesis we suppose that relevant calibration process can find and eliminate this kind of uncertainty.

6.4.2.7. Uncertainty caused by the Calibrator

The calibrator, calibrating equipment and the method used all make a contribution to the uncertainty of calibration. The uncertainty value is issued by the accrediting body [6.24]. Here in this thesis we employ '*e*' to denote this kind of uncertainty.

6.4.2.8. Uncertainty caused by Sample Surface Tilt

When the SEM is employed to measure a sample, an electron beam is required to be perpendicular to the surface of the sample being measured. If the sample is not mounted properly, not being perpendicular to the electron beam, an uncertainty arising from the sample surface tilt occurs [6.25]. Here we suppose that precise

adjustment process can find and eliminate this kind of uncertainty.

6.4.2.9. Uncertainty caused by Sample Deformation

Different samples and various treatment processes can produce various sample deformations[6.25]. Here α denotes the uncertainty of a sample deformation.

6.4.3. Evaluation of SEM-based Uncertainties

SEM-based nanoroughness measurement is one aspect of nanoscale length metrology, and it is a comparative measurement method. The principle is as below: firstly obtain secondary electron images of a sample and a standard calibrator under the same conditions, then measure the corresponding length in the secondary electron images. With the length of the standard calibrator already given, the relevant length of the sample can be calculated using a formula:

$$L = h\frac{B}{A} \tag{6.18}$$

Where h is the corresponding length in a calibrator,

A is the average value of lengths in an enlarged image of a calibrator,

B is the average value of lengths in an enlarged image of the sample.

Differentiating both sides of the above equation leads to the result that:

$$\Delta L = \frac{B}{A}\Delta h + \frac{h}{A}\Delta B - \frac{hB}{A^2}\Delta A \tag{6.19}$$

Because an indication uncertainty of the measurement instrument is too small and negligible, the correlation terms of A and B are considered to be zero. So the standard uncertainty of the measured length can be calculated as follows

$$u(L) = \sqrt{\left(\frac{B}{A}\right)^2 \Delta h^2 + \left(\frac{h}{A}\right)^2 \Delta B^2 - \left(\frac{hB}{A}\right)^2 \Delta A^2} \tag{6.20}$$

6.4.3.1. Evaluation of Δh

Δh is the uncertainty produced by a standard calibrator, and is denoted as e.

6.4.3.2. Evaluation of ΔA

The measurement process for quantity A is as below: the first point in the image is marked and its coordinate value, a, determined. The second point in the image is then marked its coordinate value, b, determined. Then the distance S between points a and b will be obtained by

$$S = |a - b| \tag{6.21}$$

and therefore

$$\Delta S = \Delta a - \Delta b \tag{6.22}$$

Since correlation terms between a and b are equal to zero

$$\Delta S^2 = \Delta a^2 + \Delta b^2 \tag{6.23}$$

Section 6.4.2 has shown that the uncertainties caused by other influential factors all can be neglected except the aiming uncertainty in the blur zone which is $\frac{1}{6}Md$.

Therefore

$$\Delta a = \Delta b = \frac{1}{6}Md \tag{6.24}$$

$$\Delta S^2 = \frac{1}{18}M^2 d^2 \tag{6.25}$$

Provided that the average value of n measurement data is employed, then

$$\Delta A^2 = \frac{1}{n}\Delta S^2 = \frac{1}{18n}M^2 d^2 \tag{6.26}$$

6.4.3.3. Evaluation of ΔB

Evaluation of ΔB is the same as that for ΔA:

$$\Delta B^2 = \frac{1}{18n}M^2 d^2 \tag{6.27}$$

6.4.3.4. Calculation of the value for A

Provided that the calibrated value of a standard calibrator is h, and its standard uncertainty is e, then the measurement value of quantity h is given by $h \pm 3e$ [6.4]. After the image is magnified the value is $Mh \pm 3Me$. Taking aiming uncertainty $\frac{Md}{\sqrt{18n}}$ in the measurement process into consideration, then

$$A = M(h \pm 3e \pm 3\frac{d}{\sqrt{18n}}) \qquad (6.28)$$

For $h >> 3e$ and $h >> 3\frac{d}{\sqrt{18n}}$, then

$$A \approx Mh \qquad (6.29)$$

6.4.3.5. Calculation of the value of B

The calculation process for the value of B is the same as that for A, so $B \approx ML$.

6.4.3.6. Combined Standard Uncertainty of the Measurement Result

Substituting the expressions above for the corresponding terms in Eq. 6.20, gives the result

$$u(L) = \sqrt{\left(\frac{ML}{Mh}\right)^2 e^2 + \frac{(hMd)^2}{M^2h^2 18n} + \frac{(hMLMd)^2}{M^2h^2 18n}} = \sqrt{\frac{L^2}{h^2}(e^2 + \frac{d^2}{18n}) + \frac{d^2}{18n}} \qquad (6.30)$$

Provided that the uncertainty α produced by the sample deformation and the uncertainty β introduced by the principle of secondary electron image formation is not be neglected, the standard uncertainties of α and β can be estimated and combined into the standard uncertainty of the measured length as given in equation 6.31:

$$u(L) = \sqrt{\frac{L^2}{h^2}(e^2 + \frac{d^2}{18n}) + \frac{d^2}{18n} + \alpha^2 + \beta^2} \qquad (6.31)$$

6.5. Uncertainty Estimation for SEM Image Processing

6.5.1. Estimation of the Uncertainty caused by Sampling Length

According to Parseval's theorem, the area under the Power Spectrum Density (PSD) curve is the square of σ_{meas}, which is the measured value of LER/LWR[6.26]. Suppose the measurement length is infinite and the spatial resolution is perfect, then theoretically the PSD will include all the component frequencies within a range from 0 to infinity, and the area under the PSD curve is squared mean of LER/LWR[6.27]. But actually the value of LER/LWR is affected by the size of the sample, the resolution of the instrument employed and the measurement time, etc[6.28]. So the LER/LWR only includes frequencies within a limited range. On the basis of the Nyquist sampling theorem, a frequency range should be from $1/L$ (L is sampling length) to $1/2\Delta$ (Δ is sampling interval), so the square of the measured value σ_{meas} for LER/LWR is equal to the area under PSD curve in the frequency range from $1/L$ to $1/2\Delta$ [6.29].

Suppose that the SEM is used to measure LER/LWR and L_{box} is the size of measurement window, then the lowest sampling frequency is $1/L_{box}$, that is

$$2\pi f_{\min} = \frac{1}{L_{box}} \qquad (6.32)$$

Any other roughness whose frequencies are less than f_{min} will be neglected, so an error of measured LER/LWR value σ_{meas} compared with the real one σ_{true} is produced. The relationship between σ_{meas} and σ_{true} is given by equation 6.33:

$$\sigma_{meas}^2 = 2\int_{f_{\min}}^{\infty} PSD(f)df = \sigma_{true}^2\left[1-\frac{2}{\pi}\tan^{-1}\left(\frac{\xi}{L_{box}}\right)\right] \qquad (6.33)$$

Where f is the spatial frequency,

σ is the deviation of the RMS of LER/LWR,

ξ is the correlation length of LER/LWR.

Figure 6.6 is the diagrammatic representation of Eq. 6.33. Provided that the sampling length L_{box} is long enough, the value of $\sigma_{meas}/\sigma_{true}$ will approach 1. Actually the sampling length is limited, hence measured values of LER/LWR σ_{meas} are always less than σ_{true}.

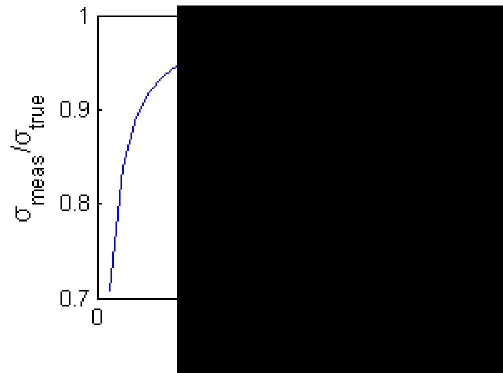

Figure 6.6-The relationship of measured and real values of LER/LWR for different sampling lengths.

Suppose $\Delta\sigma$ denotes a relative error caused by the sampling length, then

$$\Delta\sigma = \frac{\sigma_{true} - \sigma_{meas}}{\sigma_{true}} \times 100\% \qquad (6.34)$$

Table 6.1-Relative measurement error of LER/LWR with different sampling length

L_{box}/ξ	5	6	10	12	14	16	18	20	30	36	…
$\Delta\sigma(\%)$	6.49	5.40	3.22	2.68	2.29	2.0	1.78	1.60	1.06	0.888	…

According to Eq. 6.33 the relative error of LER/LWR with different sampling lengths can be calculated as shown below in Table 6.1. For example for the sampling length $L_{box} = 10\xi$, the relative error $\Delta\sigma$ of LER/LWR is 3.2%. For the sampling length

$L_{box} = 6\xi$, the relative error $\Delta\sigma$ of LER/LWR is 5.4%.

Suppose that the measurement errors caused by sampling length are normally distributed, then the uncertainty produced by the sampling length is given by[6.4]:

$$u_w = \Delta\sigma / \sqrt{3} \qquad (6.35)$$

6.5.2. Estimation of the Uncertainty caused by SEM Image Noise

In the circumstance that SEM is employed to measure nanoroughness, relevant algorithms are needed to obtain the locations of line edges or the value of specific linewidths. Since there is always noise in SEM images, errors are produced during the process of determining the locations of line edges or the values of specific linewidths. Here σ_{error} denotes the location error of a line edge caused by SEM image formation as shown in Figure 6.7[6.29]. In Figure 6.7 the true edge is represented by the thick winding line. One measured edge out of an infinite number of possibilities is marked by the slimmer winding line. The Gaussian curves overlaid on each linescan represent the distribution of measured edge locations. Then the following equation, Eq. 6.36, applies:

$$\sigma_{meas}^2 = \sigma_{true}^2 + \sigma_{error}^2 \qquad (6.36)$$

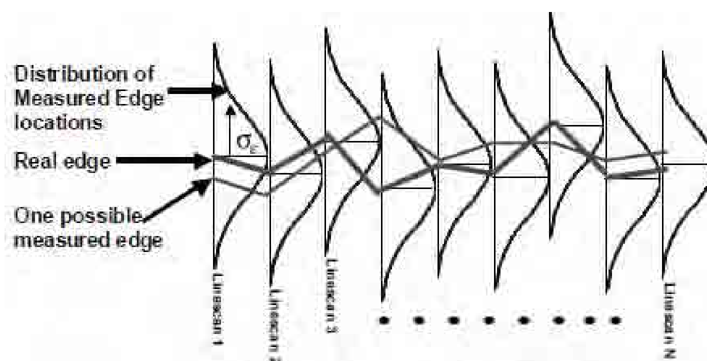

Figure 6.7- Schematic diagram of how noise effects the apparent measured position of a real line edge[6.29].

It is obvious from equation Eq. 6.36 that the noise in an SEM image will produce an error in the nanoroughness measurement. The value of this error is the same as the standard uncertainty introduced by SEM image noise. Suppose σ_ε denotes the repeatability error, then

$$\sigma_\varepsilon \cong \frac{\sigma_{error}}{\sqrt{2(N-1)}}\sqrt{1+\frac{\sigma_{true}^2}{\sigma_{error}^2+\sigma_{true}^2}} \tag{6.37}$$

Where σ_{true} and σ_{error} can be solved with the method presented by Atsuko Yamaguchi et al[6.30] given below:

$$\sigma_{meas}^2(S)=\sigma_{true}^2+\frac{\sigma_{error}^2(1)}{S}-\frac{P_0}{m-1}(2\Delta h)^{m-1}(S^{m-1}-1) \tag{6.38}$$

Where $\sigma_{error}(1)$ is the nanoroughness value from the image when S is equal to 1.

m is a power and usually its range is 2.0~2.3,

S is the mean for the numbers of the scanning lines in different images,

P_0 is a constant.

In order to simplify this calculation process, we suppose m is equal to 2 [6.30], and *F(S)* denotes $\sigma_{meas}^2(S)$. Then the above equation can be simplified to:

$$F(S)=a_1+\frac{a_2}{S}-a_3(S-1) \tag{6.39}$$

Where $a_1=\sigma_{true}^2$, $a_2=\sigma_{error}^2(1)$, and $a_3=2P_0\Delta h$.

Here σ_{true} and $\sigma_{error}(1)$ are parameters for fitting $F(S)$. The solving process is summarised as follows. Different average values $S(1,2,......,S_{\max})$ for the y-direction were set, and values of σ_{meas} for LER at different points along the line edge were calculated. Then the set of measurement data $(1,\sigma_{meas}^2(1))$, $(2,\sigma_{meas}^2(2))$,……, $(S_{\max},\sigma_{meas}^2(S_{\max}))$ was obtained. Function $y=F(S)$ was employed to fit a set of

measurement data, then regression analysis was used to get the values of parameters a_1 and a_2, that is, σ_{true} and $\sigma_{error}(1)$ respectively. SEM image noise produced a repeatability error for nanoroughness measurement, and the error was assumed to be normally distributed. Hence the uncertainty caused by SEM image noise was given by equation[6.4]:

$$u_{\varepsilon} = \frac{\sigma_{\varepsilon}}{3} \tag{6.40}$$

6.5.3. Estimation of the Uncertainty Produced by a Median Line of Least-Squares Fit

According to the definitions of LER and LWR in ITRS, RMS σ is employed as a parameter to characterize LER/LWR[6.1]. The definition of σ is given by equation 6.41:

$$\sigma_{LER} = \left[\frac{1}{N} \sum_{i=1}^{N} \left(z_i - a_i - b) \right)^2 \right]^{1/2} = \left(\frac{1}{N} \sum_{i=1}^{N} \delta_i^2 \right)^{1/2} \tag{6.41}$$

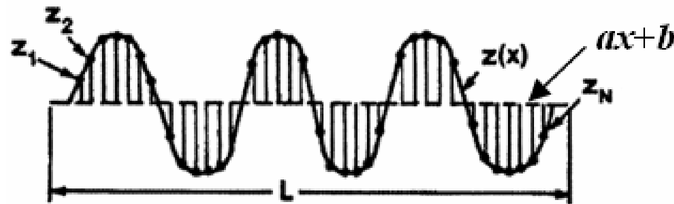

Figure 6.8- Schematic of median line fitted from a nanoroughness profile[6.31].

From Eq.6.41 it can be concluded that σ is the RMS of the distances from the profile of a line edge to its median line, as shown in Figure 6.8[6.31]. There are several methods to obtain the median line from a line edge profile, for example a least squares median line and an arithmetical median line, etc. Also different fit rules will affect measurement results for LER/LWR, producing a measurement uncertainty in

LER/LWR.

Suppose a least-squares median line is used to fit the line edge profile, and its fit equation is:

$$z = ax + b \qquad (6.42)$$

Where a and b are coefficients in the least squares equation.

The expressions for a and b are given in Eq.6.43 and Eq.6.44, respectively, as:

$$a = \frac{\sum_{i=1}^{n} x_i \sum_{i=1}^{n} z_i - n \sum_{i=1}^{n} x_i z_i}{\left(\sum_{i=1}^{n} x_i\right)^2 - n \sum_{i=1}^{n} x_i^2} \qquad (6.43)$$

$$b = \frac{\sum_{i=1}^{n} x_i \sum_{i=1}^{n} x_i z_i - \sum_{i=1}^{n} x_i^2 \sum_{i=1}^{n} z_i}{\left(\sum_{i=1}^{n} x_i\right)^2 - n \sum_{i=1}^{n} x_i^2} \qquad (6.44)$$

All raw measurement data z_i from an edge detection process for determining line edge include the uncertainty u_1 produced by the SEM. Suppose the uncertainty including in all raw measurement data are equal to each other, then according to the uncertainty propagation formula presented in GUM[6.4] the uncertainty expressions for *a, b,* and σ_{LER} can be deduced from the following:

$$u_a = u_1 \sqrt{\frac{1}{\sum_{i=1}^{N} (x_i - \bar{x})^2}} \qquad (6.45)$$

$$u_b = u_1 \sqrt{\frac{\sum_{i=1}^{n} x_i^{\,2}}{n \sum_{i=1}^{n} (x_i - \bar{x})^2}} \qquad (6.46)$$

$$u_{\sigma_{LER}}^{2}=\sum_{i=1}^{N}\left(\frac{\partial\sigma_{LER}}{\partial\delta_{i}}\right)^{2}u_{\delta(i)}^{2}=\sum_{i=1}^{N}\frac{\delta_{i}^{2}}{(\sigma_{LER})^{2}}u_{\delta i}^{2} \qquad (6.47)$$

where

$$u_{\delta i}^{2}=u_{zi}^{2}+u_{b}^{2}+u_{a}^{2}x_{i}^{2}+2u_{zi}u_{b}(-1)\rho(z_{i},b)+2u_{zi}u_{a}(-1)x_{i}\rho(z_{i},a)+2u_{a}u_{b}(-1)(-1)x_{i}\rho(a,b)$$

and $\rho(z_i,b),\rho(z_i,a),\rho(a,b)$ are the correlated factors between z_i , a and b respectively.

6.6. Case Study

6.6.1. Fabrication of a Nanoscale Grating Structure

A nanoscale grating structure was fabricated with an electron beam lithography system (CABL-9000C, Crestec Co., Japan) on ZEP520 resist (Zeon Co., Japan).

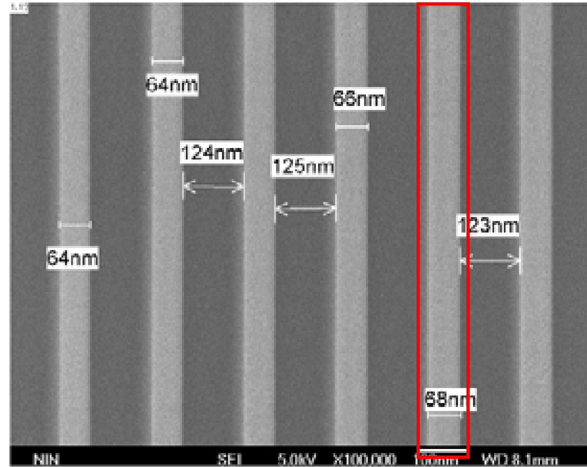

Figure 6.9- SEM image of the fabricated nanograting.

The nominal line width of nanoscale grating structure is 65 nm, and the nominal pitch was 125 nm. Upon the completion of the patterning fabrication, the grating structure was scanned by a field-emission scanning electron microscope (FESEM JSM-6700F, JEOL Ltd, Co., Japan) with an acceleration voltage of 5 kV. The image is shown in Figure 6.9. Its size is 1280×1024 pixel, and magnification is 10,000. There are 107

pixels in the scale bar which represents 100nm.

6.6.2. Evaluation of Uncertainties Produced by SEM

6.6.2.1 Measurement Condition

Images were obtained using a field-emission SEM (JSM-6700F, JEOL Ltd, Japan). The image in Figure 6.9 was obtained with an accelerating voltage of 5kV. The distance between two neighboring lines of the calibrator standard is 200nm, and its uncertainty is 3.4nm.The linewidth of the samples to be measured is 65nm, which is the average value of 25 measurement data.

6.6.2.2 Evaluation of Uncertainty Produced by SEM

It can be concluded from the measurement condition described above that for linewidth measurement the values of the parameters can be set to:

$L = 65nm, d = 1nm, h = 200nm, e = 3.4nm, n = 25$.

Substituting these values into Eq.6.31 gives an expression for the GPS implementation uncertainty of

$$\begin{aligned} u(L) &= \sqrt{\frac{L^2}{h^2}(e^2 + \frac{d^2}{18n}) + \frac{d^2}{18n}} \\ &= \sqrt{\frac{4225}{40000}(11.56 + \frac{1}{450}) + \frac{1}{450}} = 1.11nm \end{aligned} \tag{6.49}$$

As for the LER measurement of the grating line edges, the calculated value is 2nm. Substituting in the values for these parameters into Eq.6.31, gives an expression for the uncertainty of the LER measurement:

$$\begin{aligned} u(L) = u_1 &= \sqrt{\frac{L^2}{h^2}(e^2 + \frac{d^2}{18n}) + \frac{d^2}{18n}} \\ &= \sqrt{\frac{4}{40000}(11.56 + \frac{1}{450}) + \frac{1}{450}} = 0.06nm \end{aligned} \tag{6.50}$$

So, it can be concluded that for nanoroughness measurements, the uncertainty u_1 produced by the JSM-6700F SEM is 0.06nm.

6.6.3. Evaluation of Uncertainty Caused by SEM Image Preprocessing

6.6.3.1 Measurement Uncertainty u_w Produced by a Sampling Length

After the preprocessing of the SEM image shown in Figure 6.9, the line edge profile extracted from the line edge marked by the red box is shown in Figure 6.10.

Figure 6.11 shows the height correlation function $G(r)$ that was employed to analyze the LER uncertainty of the left edge of the grating structure according to the algorithms introduced in Section 3.2.2.2 of Chapter 3. It is concluded that the correlation length ξ is 25 nm and the sampling length L_{box} is 900 nm. Then

$$\frac{L_{box}}{\xi} = 36nm.$$

From Table 6.1 it can be seen that the measurement error produced by this sampling length is $\sigma_w = 0.00888nm$. So the measurement uncertainty produced by the sampling length is $u_w = \frac{0.00888}{\sqrt{3}} = 0.00513nm$.

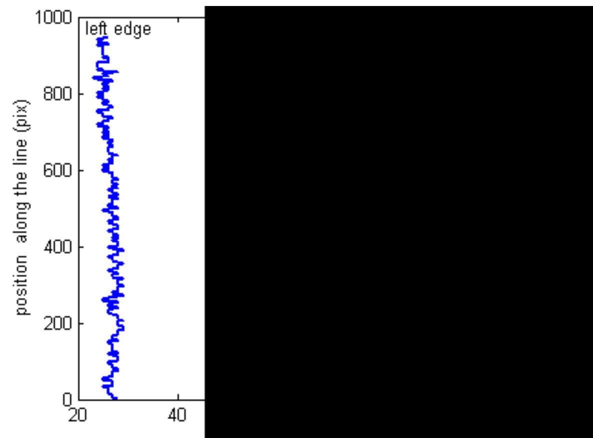

Figure 6.10- Diagram of the line edge profile extracted from the line edges marked in the red box in Figure 6.9

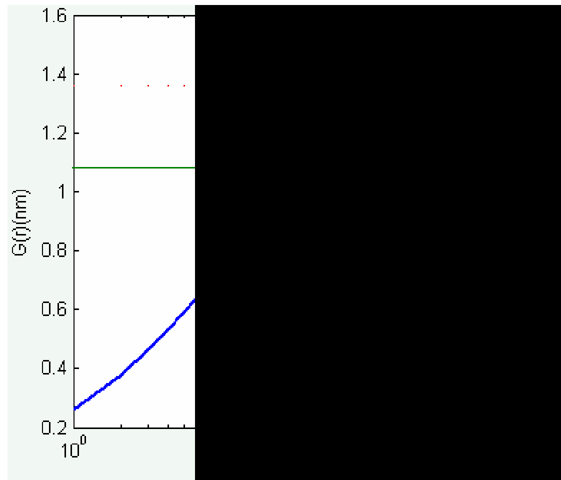

Figure 6.11- Schematic of height correlation function of left line edge marked in red box in Figure 6.9.

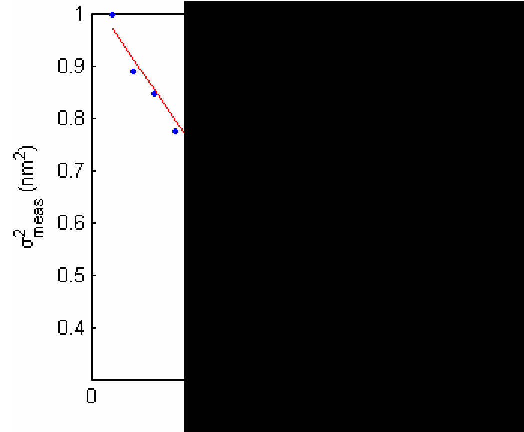

Figure 6.12- Diagram of the relationship between nanoroughness and S.

6.6.3.2 Measurement Uncertainty u_ε Produced by SEM Image Noise

Figure 6.12 shows measured nanoroughness values for the left line edge with different S values. Eq.6. 39 was employed to fit the measured data, and the σ_{true} and $\sigma_{error}(1)$ were derived as below: σ_{true}=1.025nm, $\sigma_{error}(1)$=0.28nm.

Further, from Eq.6.37, the uncertainty caused by SEM image noise was determined as follows: $\sigma_\varepsilon = 0.025nm$.

6.6.3.3 Measurement Uncertainty u_σ Produced by the Least-Squares Fitted Median Line

All 950 raw data points from the extracted line profile of the left grating line shown in Figure 6.10 include SEM uncertainty u_1. Suppose that the uncertainty distribution in every measurement point is normally distributed. According to Eq.6.50, u_1 is given by $u_1 = 0.06nm$.

Substituting these values into Eq.6.45 and Eq.6.46, u_a and u_b are given by:

$u_a = 0.043nm$, $u_b = 0.0016nm$

Further substitution of these values into Eq.6.47 gives $u_\sigma = 0.113nm$.

6.6.4. Evaluation of Total Uncertainty for LER Measurement

From the above results, the values for the following parameters are obtained.

$u_1 = 0.06nm$, $u_\sigma = 0.113nm$, $u_\varepsilon = 0.025nm$, $u_W = 0.0051nm$

Substituting these values into Eq.17. gives a total standard uncertainty for LER measurement of:

$$u_c = \sqrt{u_1^2 + u_w^2 + u_\varepsilon^2 + u_\sigma^2} = \sqrt{0.06^2 + 0.025^2 + 0.0051^2 + 0.113^2} = 0.13nm$$

Provided that the coverage factor k is 3, and the confidence level is set as 99%, the expanded uncertainty is as below:

$$u_g = ku_c = 3 \times 0.13 = 0.39nm$$

6.7. Summary

In this chapter, an overview of the theory for measuring uncertainty has been introduced, including the estimation of standard uncertainty and combination of measurement uncertainties. The uncertainty propagation model of SEM-based nanoroughness measurement has been discussed. Operations such as noise-smoothing, extraction and fit have been examined. Uncertainty components introduced by SEM image noise filtration, sampling length selection and fit operation have been calculated.

Uncertainty evaluation for SEM-based LER/LWR metrology has been discussed in detail. SEM uncertainty sources have been identified and evaluation of SEM measurement uncertainty components has been conducted. An evaluation model of

SEM-based standard measurement uncertainty has been presented. Evaluation of standard measurement uncertainty has been investigated in detail.

Uncertainty estimation for SEM image processing has been conducted, including uncertainties caused by the sampling length, SEM image noise and a median line of least-squares fitting. A case study has been presented to demonstrate the uncertainty evaluation process described in this chapter: a nanoscale grating structure with a pitch as 125nm and linewidth as 65nm was fabricated by EBL process and the LER of the grating structure was characterized by SEM as 2.0nm; the total uncertainty of the LER measurement was then evaluated as 0.13nm, and its expanded uncertainty 0.39nm with the coverage factor k as 3.

CHAPTER 7

SUMMARY AND CONCLUSIONS

7.1. Summary

This thesis presents research work on fabrication and nanoroughness characterization of nanolinewidth and nanopitch specimens as well as MIS capacitors with HfO_2 as high k dielectrc films.

Characterization and simulations of self-affine curves and 3-D random surfaces were conducted. For the characterization of self-affine curves, descriptors such as RMS σ, HHCF and PSD were identified, from which three widely-used parameters were deduced, including RMS σ, correlation length ξ and roughness exponent α (Section 3.2.2). PSD was employed to simulate the effect of parameters σ, ξ and α on the LER/LWR properties of the self-affine curves, and the effect of the above mentioned three parameters and CD on the CD variation was also simulated (Section 3.2.3). With regard to the characterization of 3D surfaces, descriptors such as RMS S_q, skewness S_{sk}, kurtosis S_{ku}, autocovariance and ACFs, PSD as well as HHCF

were identified (Section 3.3.1). The effects of the characteristic parameters on the properties of 3-D random rough surfaces were investigated and visualized, and special attention was paid to Gaussian, non-Gaussian, complicated and fractal rough surfaces. For the simulations of Gaussian random surfaces, exponential and cosine-exponential ACFs were used, and the effect of specific ACF on the properties of the rough surfaces was visualized (Section 3.3.2.1). With regard to the simulation of complicated random rough surfaces, the ACFs were constructed with a periodic (cosine) and a random (exponential) function; the surfaces and corresponding ACFs were simulated (Section 3.3.2.2). For non-Gaussian random surfaces, the effects of skewness, kurtosis, and correlation length on the properties of the surface were investigated and visualized (Section 3.3.2.3). For the simulation of self-affine random rough surfaces, the correlation function and HHCF were deduced from the corresponding PSDs and were employed to visualized the effects of characteristic parameters on the properties of the surfaces (Section 3.3.2.4). Relevant conclusions were used frequently in the subsequent investigations of this thesis.

A proposal regarding the thicknesses of the deposited films represented as nominal linewidths and pitch was put forward; nanolinewidth and nanopitch specimens were fabricated and nanoroughness-based quality control of the specimens was implemented. The MBE process was introduced and $GaAs$ substrates were selected on which $AlGaAs$ and $GaAs$ films were deposited alternately to fabricate nanolinewidth and nanopitch specimens with nominal linewidths and nominal pitch all less than 10nm (Sections 4.3.3 and 4.3.4). The thicknesses of the deposited $GaAs$

are regarded as the nominal linewidthes (2nm, 4nm, 6nm and 8nm, respectively) and the nominal pitch (5nm) (Section 4.3.2). HRTEM images were employed to characterize relevant LER/LWR and to evaluate the fabrication quality, including the noise-smoothing of the HRTEM images, the line edge extraction, and the charatcerization of LER/LWRs at the interfaces $AlGaAs/GaAs$ (Section 4.5). The wavelet transform-based multiscale line edge detector was employed to increase the accuracy of the line edge extraction(Section 4.5.3). LER/LWRs of the extracted line edge profiles were characterized with roughness parameters RMS σ, correlation length ξ and roughness exponent α (Section 4.5.5). Relevant nanoroughness characterization was used to evaluate the material selection and the fabrication process, and some process parameters were regulated in order to increase the specimen quality.

Based on relevant nanoroughness characterization, the effect of annealing temperatures for a 60nm HfO_2 film on the performance of a MIS capacitor with HfO_2 as high k dielectric was investigated, and specific fabrication parameters were regulated. Five kinds of the MIS capacitors were fabricated with HfO_2 films as deposited and annealed at 700℃, 800℃, 850℃ and 900℃ respectively (Sections 5.3.1 and 5.3.2). The thickness and the phase structures of the deposited HfO_2 films were measured by spectroscopic ellipsometry and an X-ray diffraction (Sections 5.4.1 and 5.4.2). The leakage currents and C-V properties of the MIS capacitors were tested with a semiconductor parameter analyzer and a CV analyzer respectively (Sections 5.4.3 and 5.4.4). The characterizations of surface roughness of the deposited HfO_2

films and interface roughness at the interfaces Mo/HfO_2 and HfO_2/Si were conducted by AFM and SEM (Sections 5.5.1 and 5.5.2). SEM images of the interfaces Mo/HfO_2 and HfO_2/Si were noise-smoothed, the line edges were extracted, and the interface roughness was characterized with roughness parameters RMS σ, correlation length ξ and roughness exponent α (Section 5.5.2). The nanoroughness characterization and relevant electrical measurement results concluded that the optimal annealing temperature for the deposited HfO_2 films was 700℃, while the fabrication process could be regulated according to corresponding deduced roughness parameters (Section 5.6).

The uncertainty propagation model of SEM-based LER/LWR measurement was put forward to quantitatively evaluate measurement uncertainties according to relevant ISO GPS standards (Section 6.3.3). The nanoscale grating structure on a ZEP520 resist was fabricated, and the SEM image was obtained and the LER/LWR of the grating pattern was characterized. SEM-based implementation uncertainty and method uncertainty were investigated accordingly. The implementation uncertainty was mainly caused by the random and systematic errors of the SEM instrument as well as the sample variation (Section 6.4). The method uncertainty was produced by the SEM image preprocessing operations on which the emphases were placed in this thesis, such as the noise-smoothing of the SEM images, the extraction of line edges of interest, and the fit of the extracted line edges (Section 6.5). For SEM-based implementation uncertainty and implementation uncertainty, the influential factors were identified and their uncertainties were quantitatively estimated. The case study

employed the above mentioned propagation model and demonstrated the detailed quantitative evaluation process for the SEM-based LER/LWR measurement uncertainty, which was an absolutely necessary part of a LER/LWR measurement result, as exemplified by the investigations in this thesis (Section 6.6).

7.2. Conclusions

The conclusions obtained from this research project are summarised below.

Compared with experimental investigations, simulations of the effects of the characteristic parameters on the properties of self-affine curves and various random rough surfaces are flexible, low cost and highly efficient. Simulations of self-affine curves showed that the parameters σ, ξ and α impacted significantly on the LER/LWR properties of the self-affine curves as well as on the CD variation. The visualizations of random rough surfaces demonstrated that ACFs could describe the Gaussian and complicated rough surfaces, while skewness, kurtosis, and correlation length impacted on the properties of non-Gaussian rough surfaces significantly. For self-affine random rough surfaces, the correlation function and HHCF could be deduced from the PSDs, hence characterizing the surface properties.

The MBE-based process along with the selection of *AlGaAs* and *GaAs* are capable of fabricating desired nanolinewidth and nanopitch specimens with nominal linewidths of 2nm, 4nm, 6nm and 8nm, and nominal pitch aofs 5nm. Based on HRTEM images of the specimens, parameters σ, ξ and α of relevant LER/LWR showed that in real space and frequency domains the quality of line edges met the requirements for the specimens, and showed that specific process parameters should

be regulated carefully to further improve the line edge quality. The fabricated linewidthes and pitch deduced from HRTEM images were a little less than the corresponding nominal linewidthes and nominal pitch respectively, leading to the conclusion that either the epitaxial rate or epitaxial time should be increased during MBE process.

The annealing temperature for the deposited HfO_2 film is an important process parameter for the properties of the MIS capacitor. SEM image-based nanoroughness characterization along with electrical measurement results for the MIS capacitor properties showed that 700℃ was an optimal annealing temperature to improve the quality of the deposited HfO_2 film. Parameters σ, ξ and α of relevant LER/LWR demonstrated the detailed effect of the process parameters on the quality of line edges and, hence, the properties of the MIS capacitors. This thickness of the deposited HfO_2 film obtained by the spectroscopic ellipsometry was compared with that obtained by SEM image-based charatcerization, and the sample tilt during SEM measurement was calculated (here the sample tilt was 37.39°), enabling the corresponding uncertainty of SEM to be estimated.

Corresponding uncertainty is an indispensable part of a nanoroughness measurement result, and should be evaluated according to specific requirements of relevant ISO GPS standards and GUM. The uncertainty propagation model of the SEM-based nanoroughness measurement was presented; the method and implementation uncertainties were both evaluated. For the SEM-based nanoroughness measurement of a grating nanostructure, the implementation uncertainty caused by the SEM was

0.06nm, the uncertainties produced by the sampling length, the SEM image noise and the fitted median line of the least-square method were 0.00513nm, 0.025nm, and 0.113nm, respectively. The total standard uncertainty was 0.13nm while its expanded uncertainty with the coverage factor $k = 3$ was 0.39nm.

7.3. Future Work

SEM/TEM image-based metrology of LER/LWR for nanolinewidth and nanopitch specimens as well as the MIS capacitor with HfO_2 as high k dielectric has been carried out. However the algorithms and characteristic parameters obtained from this thesis cannot be applied directly to the metrology of sidewall roughness, which is another important specification for nanostructures and nanodevices and impacts their performances accordingly[7.1]. For example, the sidewall roughness of the contacts with a high aspect ratio of more than 15 will cause electromigration in a metal connection[7.2], and in a waveguide will improve its radiation loss, hence decreasing the sensitivity of its resonator and the extinction factor of its modulator[7.3]. Since AFM is a potential candidate to measure above mentioned sidewall roughness, it is helpful to investigate new AFM-based algorithms for the sidewall roughness metrology.

A nanoscale multi-stepheight specimen is another kind of calibrator for specific instrument and measurand transferability and traceability; it is important to propose new techniques to fabricate a multi-stepheight specimen with nominal stepheight less than 10nm. Figure 7.1 shows that an MBE-based technique along with a wet or dry selective etching can fabricate the above mentioned multi-stepheight specimen. This

method is different from the one proposed by Dixson et al[7.4] at NIST to fabricate the silicon single atom step specimen, and also different from the one put forward by Hoffmann et al[7.5] at PTB to fabricate the single silicon dioxide stepheight specimen. Once such multi-stepheight specimen is fabricated, the relevant nanoroughness should be characterized to obtain the final fabrication accuracy and regulate the fabrication process.

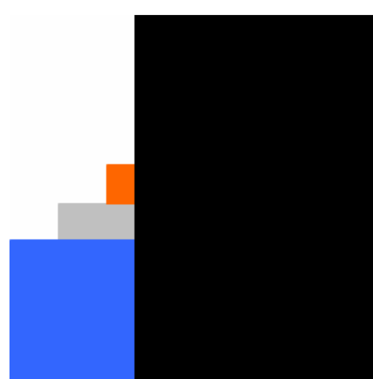

Figure 7.1- Diagram of a nanoscale multi-stepheight specimen.

The topography of a microsphere impacts significantly on its adsorption on a specific substrate, and carbon nanotubes or silicon nanowires are frequently deposited on the surface of a nanosphere in order to modify its topography, hence changing its adsorption ability on a specific surface[7.6]. Therefore how to characterize the surface nanoroughness of these nanospheres is a prerequisite to investigate its adsorption mechanism on a specific substrate.

Uncertainty estimation for SEM-based nanoroughness measurement has been investigated. SEM, TEM and AFM are also the widely-used instruments to characterize relevant roughness of specific nanostructures and nanodevices. Consequently in terms of the relevant standards of ISO GPS, mentioned in this thesis,

the implementation uncertainty and method uncertainty of TEM and AFM should be quantitatively evaluated and reported, so that the accuracy of corresponding nanoroughness metrology could be improved.

LIST OF REFERENCES

[1.1] Yamaguchia A., Ichinoseb K., Shimamotob S., Fukudaa H., Tsuchiyaa R., Ohnishia K., Kawadac H., Iizumic T. *Metrology of LER: influence of line-edge roughness (LER) on transistor performance*. Metrology, Inspection, and Process Control for Microlithography XVIII, Proceedings of SPIE, 2004, **5375**: p. 468-476

[1.2] Palasantzas G., Hosson De J.Th.M. *The effect of mound roughness on the electrical capacitance of a thin insulating film*. Solid State Communications. 2001. **118**(4): p.203-206.

[1.3] Lee M.H., Chen K.F., Lai C.C., et al. *The Roughness-Enhanced Light Emission from Metal-Oxide-Silicon Light-Emitting Diodes Using Very High Vacuum Prebake*. The Japan Society of Applied Physics. 2002, **41**: p.L 326–L 328.

[1.4] Yang S. C. *Effects of surface roughness and interface wettability on nanoscale flow in a nanochannel*. Microfluid Nanofluid. 2006, **2**: p.501–511.

[1.5] Deligianni D.D., Katsala N., Ladas S., et al. *Effect of surface roughness of the titanium alloy Ti-6Al-4V on human bone marrow cell response and on protein adsorption*. Biomaterials. 2001, **22**: p. 1241-1251.

[1.6] Benard Q., Fois M., Grise M. *Roughness and fibre reinforcement effect onto wettability of composite surfaces*. Applied Surface Science. 2007, **253**: p.4753–4758.

[1.7] Gogolides E., Constantoudis V., Patsis G.P., Tserepi A. *A review of line edge roughness and surface nanotexture resulting from patterning processes*. Microelectronic Engineering. 2006, **83**: p1067-1072.

[1.8] Son J.Y., Maeng W.J., Kim W.H., et al. *Interface roughness effect between gate oxide and metal gate on dielectric property*. Thin Solid Films. 2009, **517**: p.3892–3895.

[1.9] Nelson C., Palmateer S.C., Forte A.R., Lyszczarz T.M. *Comparison of metrology methods for quantifying the line edge roughness of patterned features*. Journal Vacuum Science and Technology. 1999, B17(**6**): p.2488-2498.

[1.10] Rijpersa B., Findersa J., Suzukib H., et al. *Use of 3D Metrology for Process Control*. Metrology, Inspection, and Process Control for Microlithography XXIII, Proceedings of SPIE. 2009, **7272**: p.727235-1-11.

[2.1] Gogolides E., Constantoudis V., Patsis G. P., et al. *A review of line edge roughness and surface nanotexture resulting from patterning processes*. Microelectronic Engineering. 2006, **83(4-9)**: p.1067-1072.

[2.2] Birkedal D., Lyssenko V. G., Pantke K.-H., et al. *Nanoroughness Localization of Excitons in Gaas Multiple-Quantum Wells Studied by Transient 4-Wave-Mixing*. Physical Review B. 1995, **51(12)**: p.7977-7980.

[2.3] Narayan P. and Hancock B. C. *The relationship between the particle properties, mechanical behavior, and surface roughness of some pharmaceutical excipient compacts*. Materials Science and Engineering A. 2003, **355(1-2)**: p.24-36.

[2.4] Bigerelle M., Gautier A., Iost A. *Roughness characteristic length scales of micro-machined surface: A multi-scale modelling*. Sensors and Actuators B. 2007, **126**: p.126-137.

[2.5] Swerts J., Temst K., Vandamme N., et al. *Interplay between surface roughness and magnetic properties in Ag/Fe bilayers*. Journal of Magnetism and Magnetic Materials. 2002, **240(1-3)**: p.380-382.

[2.6] Sun M. X., Zhang C. P., Qi S. W., et al. *Effect of surface roughness on the determination of tissue optical properties*. Optik. 2010, **121(4):** p.373-377.

[2.7] Taylor J. B., Carrano A. L., Kandlikar S. G. Characterization of the effect of surface roughness and texture on fluid flow-past, present, and future. International Journal of Thermal Science. 2006, **45**: p.962-968.

[2.8] Kajikawa Y. *Roughness evolution during chemical vapor deposition*. Materials Chemistry and Physics. 2008, **112(2)**: p.311-318.

[2.9] Donovan M. J. and Smyth H. D. C. *Influence of size and surface roughness of large lactose carrier particles in dry powder inhaler formulations*. International Journal of Pharmaceutics. 2010, **402(1-2)**: p.1-9.

[2.10] Khan S. P., Auner G. G., Newaz G. M. *Influence of nanoscale surface roughness on neural cell attachment on silicon*. Nanomedicine: Nanotechnology, Biology, and Medicine. 2005, **1**: p.125-129.

[2.11] Orji N.G., Vorburger T.V., Fu J., et al. *Line edge roughness metrology using atomic force microscopes*. Measurement Science and Technology. 2005, **16**: p.2147-2154.

[2.12] Reynolds G.W., Taylora J.W. *Factors contributing to sidewall roughness in a positive-tone, chemically amplified resist exposed by x-ray lithography*.

Journal Vacuum Science and Technology B. 1999, **17(2)**: p.334-344.

[2.13] Boher P., Petit J., Leroux T., et al. *Optical Fourier transform scatterometry for LER and LWR metrology*. Metrology, Inspection, and Process Control for Microlithography XIX. 2005, **5752**: p.192-203.

[2.14] *The International Technology Roadmap for Semiconductors(ITRS), 2007 Edition.* http://www.itrs.net/reports.html.

[2.15] Foucher J., Pargon E., Martin M., et al. The CD Metrology Perspectives and Future Trends. Lithography Asia 2008, Proceedings of SPIE. 2008, **7140**: p.71400F-1- 71400F-13.

[2.16] Babin S., Borisov S., Lvanchikov A., et al. *Calibration of CD-SEM: moving from relative to absolute measurements*. Metrology, Inspection, and Process Control for Microlithography Xxii, Proceedings of SPIE. 2008, **6922(1-2)**: p.69222-1-69222-8.

[2.17] Abe H., Hamaguchi A., Yamazaki Y., et al. *Evaluation of CD-SEM measurement uncertainty using secondary electron simulation with charging effect*. Metrology, Inspection, and Process Control for Microlithography XXI, Proceedings of SPIE. 2007, **6518**: p.6518L-1-6518L-10.

[2.18] Tanaka M., Meessen J., Shishido C., et al. *CD bias reduction in CD-SEM linewidth measurements for advanced lithography*. Metrology, Inspection, and Process Control for Microlithography Xxii, Proceedings of SPIE. 2008, **6922(1-2)**: p.69221T-1-69221T-11.

[2.19] Oh S. H., Cho S. U., Kim C. S., et al. *Fabrication of nickel stamp with improved sidewall roughness for optical devices*. Microelectronic Engineering. 2011, in Press.

[2.20] Constantoudis V., Kokkoris G., Xydi P., et al. *Modeling of line edge roughness transfer during plasma etching*. Microelectronic Engineering. 2009, **86(4-6)**: p.968-970.

[2.21] Murugesan-Kuppuswamy V. K., Constantoudis V., Gogolides E. *Contact Edge Roughness: Characterization and modeling*. Microelectronic Engineering, 2011, in Press.

[2.22] Palasantzas G., Zhao Y. P., De Hosson J.Th.M., et al. *Roughness effects on magnetic properties of thin films*. Physica B. 2000, **283(1-3)**: p.199-202.

[2.23] Toledano M., Osorio E., Aguilera F.S., et al. *Bond strength and nanoroughness assessment on human pretreated cementum surfaces*. Journal of dentistry. 2010, **38**: p.678–685.

[2.24] Liu Y. Y., Yang S. Y., Wei G. X., et al. Electrical and optical properties dependence on evolution of roughness and thickness of Ga: *ZnO films on rough quartz substrates*. Surface & Coatings Technology. 2011, **205(11)**:

p.3530-3534.

[2.25] Microsystems Technology Standardisation Roadmap 2001, IST-2001-37683, by National Physical Laboratory, Institut fur Mikrotechnik Mainz GmbH and Rutherford Appleton Laboratory.

[2.26] Li Q. X., Li Y. H., Wang B. X., et al.). *Experimental study on the measurement of micro structures*. Optical Engineering. 2004, **43(11)**: p.2736-2741.

[2.27] McClelland J. J., Anderson W. R., Bradley C. C., et al.). *Accuracy of nanoscale pitch standards fabricated by laser-focused atomic deposition*. Journal of Research of the National Institute of Standards and Technology. 2003, **108(2)**: p.99-113.

[2.28] Jing W. X., Jiang Z. D., Zhu M. Z., et al. *Fabrication of nano-scale reference materials with scanning probe microscopy (SPM)-based lithography*. 2006 1st IEEE International Conference on Nano/Micro Engineered and Molecular Systems. 2006, **1-3**: p.1194-1197.

[2.29] Avouris P., Martel R., Hertel T., et al. *AFM-tip-induced and current-induced local oxidation of silicon and metals*. Applied Physics A. 1998, 66: p.S659-S667.

[2.30] Snow E.S., Campbell P.M. *AFM Fabrication of Sub-10nm Metal-Oxide Devices with in Situ Control of Electrical Properties*. Science. 1995, **270**: p.1639-1643.

[2.31] Fang T. H., Weng C. I., Chang J. G., et al. *Machining characterization of the nano-lithography process using atomic force microscopy*. Nanotechnology. 2000, **11(3)**: p.181-187.

[2.32] Fang T. H., Weng C. I., Chang J. G., et al. *Molecular dynamics simulation of nano-lithography process using atomic force microscopy*. Surface Science. 2002, **501(1-2)**: p.138-147.

[2.33] Orji N. G. and Dixson R. G. *Higher order tip effects in traceable CD-AFM-based linewidth measurements*. Measurement Science & Technology. 2007, **18(2)**: p.448-455.

[2.34] Tortonese M., Lorusso G., Blanquies R., et al. *Sub-50 nm isolated line and trench width artifacts for CD metrology*. Metrology, Inspection, and Process Control for Microlithography Xviii, Proceedings of SPIE. 2004, **5375**: p.647-656.

[2.35] Zhao F. X., Jiang Z. D., Jing W. X., et al. *Fabrication and characterization of sub-45 nm multiple linewidth samples*. Measurement Science & Technology. 2007, **18(6):** p.1689-1693.

[2.36] Zaborowski M., Szmigiel D., Gotszalk T., et al). *Nano-line width control*

and standards using Lateral Pattern Definition technique. Microelectronic Engineering. 2006, **83(4-9)**: p.1555-1558.

[2.37] Arthur J. R. *Molecular beam epitaxy*. Surface Science. 2002, **500**: p.189-217.

[2.38] Jiang Z. D., Wang H. R., Fei B. *Research into the application of fractal geometry in characterising machined surfaces*. International Journal of Machine Tools & Manufacture. 2001, **41(13-14)**: p.2179-2185.

[2.39] Zhao Y. P., Wang G. C., Lu T. M. *Characterization of amorphous and crystalline rough surface: Principles and applications*. 2001, New York: Academic Press.

[2.40] Wu J. J. *Simulation of rough surfaces with FFT*. Tribology International. 2000, **33**: p.47-58.

[2.41] Shinozuka M., Jan C.M. *Digital simulation of random process and its application*. Journal of Sound and Vibration, 1972, **25(1)**:p.111-128

[2.42] Patir N. *A numerical procedure for random generation of rough surfaces*. Wear, 1978, **47(2)**: p.263-277.

[2.43] Watson W., Spedding TA. *The time series modelling of non-Gaussian engineering processes*. Wear, 1982, **83(2)**: p.215-231.

[2.44] Jiang Z. D. and Zhao Z. X. *The Autoregressive Spectrum Analysis in the Application to the Measurement of Roundness Error*. Acta Metrologica Sinaca. 1984, **5(4)**: p.312-317

[2.45] You S.J., Ehmann K.F. *Computer synthesis of three-dimension surfaces*. Wear, 1991, **145(1)**: p.29-42.

[2.46] Hu Y.Z., Tonder K. *Simulation of 3-D random rough surface by 2-D digital filter and Fourier analysis*. International Journal of Machine Tools and Manufacture, 1992, **32(1-2)**: p.83-90.

[2.47] Ganti S., Bhushan B. *General fractal analysis and its applications to engineering surfaces*. Wear, 1995, **180(1-2)**: p.17-34.

[2.48] Wu J. J. *Simulation of non-Gaussian surfaces with FFT*. Tribology International. 2004, **37(4)**: p.339-346.

[2.49] Patrikar R. M., Dong C. Y., Zhuang W. J. *Modelling interconnects with surface roughness*. Microelectronics Journal. 2002, **33(11)**: p.929-934.

[2.50] Patrikar R. A. *Modeling and simulation of surface roughness*. Applied Surface Science. 2004, **228(1-4)**: p.213-220.

[2.51] Wold H. A study in the analysis of stationary time series. 2nd edition. 1958, Almquist and Wiksell, Uppsala, Stockholm, Sweden.

[2.52] Chen H., Hu Y. Z., Wang H., et al. *Computer Simulation of Roughness Surfaces*. Lubrication Engineering. 2006, **10**: p.52-55 59.

[2.53] *The International Technology Roadmap for Semiconductors(ITRS), 2001 Edition.* http://www.itrs.net/reports.html.

[2.54] *The International Technology Roadmap for Semiconductors(ITRS), 2003 Edition*. http://www.itrs.net/reports.html.

[2.55] Stucchi M., Bamal M., Maex K. *Impact of line-edge roughness on resistance and capacitance of scaled interconnects*. Microelectronic Engineering. 2007, **84(11)**: p.2733-2737.

[2.56] He G., Fang Q., Li G. H., et al. *Structural and optical properties of nitrogen-incorporated HfO_2 gate dielectrics deposited by reactive sputtering*. Applied Surface Science. 2007, **253**: p.8483-8488.

[2.57] Huang L. Y., Li A. D., Zhang W. Q., et al. *Fabrication and characterization of La-doped HfO2 gate dielectrics by metal-organic chemical vapor deposition*. Applied Surface Science. 2010, **256(8)**: p.2496-2499.

[2.58] Balasubramanian M., Bera L. K., Mathew S., et al. *Wet etching characteristics and surface morphology evaluation of MOCVD grown HfO_2 film*. Thin Solid Films. 2004, **462-463**: p.101-105.

[2.59] Mitchell D. R. G., Aidla A., Aarik J. *Transmission electron microscopy studies of HfO2 thin films grown by chloride-based atomic layer deposition*. Applied Surface Science. 2006, **253(2)**: p.606-617.

[2.60] Son J. Y., Maeng W. J., Kim W. H., et al. *Interface roughness effect between gate oxide and metal gate on dielectric property*. Thin Solid Films. 2009, **517(14)**: p.3892-3895.

[2.61] Tokas R. B., Sahoo N. K., Thakur S., et al. *A comparative morphological study of electron beam co-deposited binary optical thin films of HfO_2:SiO_2 and ZrO_2:SiO_2*. Current Applied Physics. 2008, **8(5)**: p.589-602.

[2.62] Yamaguchi A., Ichinose K., Shimamoto S., et al. *Metrology of LER: influence of line-edge roughness (LER) on transistor performance*. Metrology, Inspection, and Process Control for Microlithography Xviii, Proceedings of SPIE. 2004, **5375**: p.468-476.

[2.63] Lee M. H., Chen K. F., Lai C. C., et al. *The roughness-enhanced light emission from metal-oxide-silicon light-emitting diodes using very high vacuum prebake*. Japanese Journal of Applied Physics Part 2-Letters. 2002, **41(3B)**: p.L326-L328.

[2.64] Muller, B., Riedel M., De Paul S. M., et al. *Impact of nanometer-scale roughness on contact-angle hysteresis and globulin adsorption*. Journal of Vacuum Science & Technology B. 2001, **19(5)**: p.1715-1720.

[2.65] Padial-Molina M., Galindo-Moreno P., Fernández-Barbero J. E., et al. *Role of wettability and nanoroughness on interactions between osteoblast and modified silicon surfaces*. Acta Biomaterialia. 2011, **7(2)**: p.771-778.

[2.66] Wang J. X., Ma L. M., Jiang X. Q., et al. *A Framework for Uncertainty Evaluation of GPS Standard-chain*. Proceedings of ASPE Summer Topical Meeting on Uncertainty Analysis in Measurement and Design. Pennsylvania, USA. 2004: p.146 ~ 151.

[2.67] ISO, IEC, BIPM, OIML, IFCC, IUPAC, IUPAP. *Guide to the Expression of Uncertainty in Measurement (GUM)*. 1993, International Organization for Standardization, Geneva, Swiss.

[2.68] ISO 14253-2-2011. *Geometrical Product Specifications (GPS)-Inspection by measurement of workpieces and measuring equipment-Part 2:Guide to the extimation of uncertainty in GPS measurement,incalibration of measuring equipment and in product verification*. 2011, International Organization for Standardization, Geneva, Swiss.

[2.69] Kramer U., Navarra A., Fleischer G., et al. *Physical matching of CD-SEM: noise analysis and verification in FAB environment*. Metrology, Inspection, and Process Control for Microlithography Xxii, Proceedings of SPIE. 2008, **6922(1-2)**: p.69221R-1-69221R-11.

[2.70] Onozuka T., Ojima Y., Meessen J., et al. *Estimation of pattern shape based on CD-SEM image by using MPPC method*. Metrology, Inspection, and Process Control for Microlithography XX, Proceedings of SPIE. 2006, **6152**: p.61521D-1-61521D-9.

[2.71] Villarrubia J. S., Vladar A. E., Lowney J. R., et al. *Scanning electron microscope analog of scatterometry*. Metrology, Inspection, and Process Control for Microlithography Xvi, Proceedings of SPIE. 2002, **4689**: p.304-312.

[2.72] Villarrubia J. S., Vladar A. E., Postek M. T. *Scanning electron microscope dimensional metrology using a model-based library*. Surface and Interface Analysis. 2005, **37(11)**: p.951-958.

[2.73] Frase C. G., Buhr E., Dirscherl K. *CD characterization of nanostructures in SEM metrology*. Measurement Science & Technology. 2007, **18(2)**: p.510-519.

[2.74] Villarrubia J.S., Vladar A.E., Postek M.T. *A simulation study of repeatability and bias in the CD-SEM*. Proceedings of SPIE. 2003, **5038**: p.138–149.

[2.75] Marion A. *An Introduction to Image Processing*. 1991, London: Chapman and Hall.

[2.76] Matalsa L., Benjamin R., Kitney R. *An edge detection technique using the fact model and parameterized relation labeling*. Pattern Analysis and

Medical Intelligence, IEEE Transaction. 1997,**19**: p.328-341.

[2.77] Aydin T., Yemez Y., Anarim E., et al. *Multidirectional and multiscale edge detection via M-band wavelet transform*. IEEE Transactions on Image Processing. 1996, **5(9)**: p.1370-1377.

[2.78] Yamaguchi A., Steffen R., Yamamoto J., et al. *Single-shot method for bias-free LER/LWR evaluation with little damage*. Microelectronic Engineering. 2007, **84(5-8)**: p.1779-1782.

[3.1] Majumdar A, Bhushan B. *Fractalmodel of elasticp lastic contact between rough surfaces.* ASME Joural of Tribology. 1991, 113 (**1**): p.1～11.

[3.2] Constantoudis V., George P. P., Leunissen L. H. A., et al. *Toward a complete description of line width roughness: a comparison of different methods for vertical and spatial LER and LWR analysis and CD variation*. Proc. of SPIE, 2004, **5375**: p 967-977.

[3.3] Majumdar A., Bhushan B. *Role of fractal geometry in roughness characterization and contact mechanics of surfaces*. ASME, Joural of Tribology, 1990, 112 (**2**) : p. 205～216.

[3.4] Majumdar A. Tien C. L. *Fractal characterization and simulation of rough surfaces*. Wear. 1990, 136(**2**): p.13-327.

[3.5] Zhao Y. P., Wang G. C., Lu T. M. *Experimental methods in the physical sciences. Characterization of amorphous and crystalline rough surface: Principles and applications.* USA: Academic press. 2002, **37**: p.17-23.

[3.6] Hasegawa M., Liu J. C., Okuda K., et al. *Calculation of the fractal dimensions of machined surface profiles*. Wear. 1996, **192**: p. 40-45

[3.7] Asenov A., Kaya S. and Brown A. R. *Intrinsic parameter fluctuations in decananometer MOSFETs introduced by gate line edge roughness*. IEEE Trans. Electron Device. 2003, 50(**5**): p.1254-1260.

[3.8] Constantoudis V., G. P. Patsis, L. H. A. Leunissen, et al. *Line edge roughness and critical dimension variation: Fractal characterization and comparison using model functions*. J. Vac. Sci. Technol. B ,2004, 22(**4**): p. 1974-1981.

[3.9] J.J. Wu. *Simulation of rough surfaces with FFT*. Tribology International, 2000, **33**: p. 47-58.

[3.10] Peklenik J. *New Developments in Surface Characterization and Measurements by Means of Random Process Analysis*. Proceeding of the Institute of Mechanical Engineer., 1967-1968, **182**: p.108-126.

[3.11] Whitehouse D. J., Archard J. F. *The Properties of Random Surfaces of Significance in Their Contact*. Proceedings Royal Society. London. 1970, 316 (**A**): p.97-121.

[3.12] Uchidate M., Shimizu T., Iwabuchi A., et al. *Generation of reference data of 3D surface texture using the non-causal 2D AR model*. Wear, 2004, **257**: p. 1288–1295.

[3.13] Uchidate M., Yanagi K., Yoshida I. et al. *Generation of 3D random topography datasets with periodic boundaries for surface metrology algorithms and measurement standards.* Wear, In press.

[3.14] Robert E. W. *Quantile estimators of Johnson curve parameters*. Biometrika, 1980, 67 (**3**): p.725-728.

[3.15] Hu Y.Z., Tonder K. *Simulation of 3-D random rough surface by 2-D digital filter and fourier analysis*. International Journal of Machine Tools Manufacturing, 1992, 32(**1/2**): p.83–90.

[3.16] Peng W., Bhushan B. *Modelling of surfaces with a bimodal roughness distribution*. Proceedings of the Institution of Mechanical Engineers, Part J: Journal of Engineering, 2000, 214 (**5**): p. 459-470.

[3.17] Wu J.J. *Simulation of non-Gaussian surfaces with FFT* . Tribology International, 2004, **37**: p.339-346.

[3.18] Goff J.A. and Jordan T.H. *Stochastic modeling of sea floor morphology:inversion of sea beam data for second-order statistics*. Journal of Geophysical Research. 1988, **93**: p.13589-13608.

[4.1] *Microsystems Technology Standardisation Roadmap*, IST-2001-37683, by National Physical Laboratory, Institut fur Mikrotechnik Mainz GmbH and Rutherford Appleton Laboratory.

[4.2] *The International Technology Roadmap for Semiconductors(ITRS), 2009 Edition.* http://www.itrs.net/reports.html.

[4.3] Titov A., Malinovsky I., C. Massone A. *Nanometrology Regime in Length Measurements of Material Artefacts with Nominal Lengths up to 100 mm*. Proceedings, XVII IMEKO World Congress, 2003, p.1864-1869.

[4.4] Coleman J. J. *Metalorganic Chemical Vapor Deposition for Optoelectronic Devices*. Proceedings, the IEEE. 1997, **85**(**11**): p.1715-1729.

[4.5] Belkink A., Song W., McDonough G. and Scholl R. *Biased Dual Magnetron Sputter Deposition of Alumina*. Proceedings, 45th Annual Technical Conference, 2002, p.184-189.

[4.6] Beica T., Frunza S., Zgura I., Frunza L., Cotarlan C., Negrila C., Vlaicu A. M., Zaharia C. N. *Nanostructured Gold Layers. I. Deposition by Vacuum Evaporation at Small Angles of Incidence*. Journal of Optoelectronics and Advanced Materials, 2010, **12**(**2**): p.347-353.

[4.7] Sampath A. V., Bhattacharyya A., Singh R., Eddy C. R., Lamarre P., Stacey W.

F., Morris R. S., Moustakas T. D. *Growth and Fabrication of High Reverse Breakdown Heterojunction n-Gan:p-6H-SiC Diodes*. Material Research Society Symposium Proceedings, 2003, **743**: p.L6.34.1-L6.34.6.

[4.8] Arthur J. R. *Molecular Beam Epitaxy*. Surface Science, 2002, **500**: p.189-217.

[4.9] Foxon C.T., Joyce B.A. *Growth and Characteristics of Semiconductors*. 1990, Adam Hilger/IOP, Bristol, UK.

[4.10] Nakamura M., Fujioka H., Ona K., Takeuchi M., Mitsui T., Oshima M. *Molecular Dynamics Simulation of III-V Compound Semiconductor Growth with MBE*. Journal of Crystal Growth, 2009, **209**: p.232-236.

[4.11] Luque A., Hegedus S. *Handbook of Photovoltaic Science and Engineering*. 2003, John Wiley & Sons, New York, USA.

[4.12] Herbig M., King A., Reischig P., et al. *3-D growth of a short fatigue crack within a polycrystalline microstructure studied using combined diffraction and phase-contrast X-ray tomography*. Acta Materialia. 2011, 59(**2**): p590-601.

[4.13] Jong A.F.D., Coene W., Dyck D.V. *Image processing of HRTEM images with non-periodic features*. Ultramicroscopy. 1989, 27(**1**): p53-65.

[4.14] Nakamori S., García-Ligero M.J., Hermoso-Carazo A., et al. *Filtering of images corrupted by multiplicative and white plus coloured additive noises using covariance information*. Mathematical and Computer Modelling. 2008, 47(**3-4**): p298-311.

[4.15] He G.P., Kraus K. *A method to design filters for image smoothing*. Pattern Recognition Letters. 1992, 13(**7**): p509-515.

[4.16] Patsis G. P., Constantoudis V., Tserepi A., Gogolides E., Grozev G. *Quantification of line-edge roughness of photoresists. I. A comparison between off-line and on-line analysis of top-down scanning electron microscopy images*. J. Vac. Sci. Technol. B 2003, 21(**3**): p1008-1018.

[4.17] Philip R. B., Jeffery R. P., Kenneth W. T., and Thomas P. K. *Semiconductor sidewall shape estimation.* Journal of Electronic Imaging, 2004, 13(**3**): 474–485.

[4.18] Rafael C. G., Richard E.W. *Digital image processing .(second edition).* 2002, Prentice Hall, Upper Saddle River, New Jersey, USA.

[4.19] Naif A., Mohamed K., Jernigan E. Detail preserving impulsive noise removal. Signal Processing: Image Communication. 2004, 19(**10**): p993-1003.

[4.20] Zhu D., Razaz M., Fisher M.. *An adaptive algorithm for image restoration using combined penalty functions*. Pattern Recognition Letters. 2006, 27(**12**): p1336-1341.

[4.21] Yoshihiro M., Koji N. and Hiromu F. *Line edge roughness measurement of*

nanostructures in SEM metrology by using statistically matched wavelet. Proc. of SPIE, 2007, **6763**: 67630F-1~67630F-9.

[4.22] Mallat S. G. *A wavelet tour of signal processing.* 1998, Academic press, California, USA.

[4.23] Keinert F. *Wavelets and multiwavelets*. 2004, A CRC Press Company, New York, USA.

[4.24] Thomas T. R. *Rough surfaces(Second Edition).* Imperial College Press, London, 1999.

[5.1] Gogolides E., Constantoudis V., Patsis G.P., Tserepi A. *A review of line edge roughness and surface nanotexture resulting from patterning processes*. Microelectronic Engineering. 2006, **83**: p1067-1072.

[5.2] Albina A., Taberna P.L., Cambronne J.P., Simon P., Flahaut E. and Lebey T. *Impact of the surface roughness on the electrical capacitance*. Microelectronic Journal. 2006. **37**(8): p.752-758.

[5.3] Palasantzas G., Hosson De J.Th.M. *The effect of mound roughness on the electrical capacitance of a thin insulating film*. Solid State Communications. 2001. **118**(4): p.203-206.

[5.4] Son J.Y., Maeng W.J., Kim Woo-Hee, Shin Y.H., Kim Hyungjun. *Interface roughness effect between gate oxide and metal gate on dielectric property*. Thin Solid Films. 2009. **517**: p. 3892-3895.

[5.5] Taur Y., Buchanan A.D., Chen W., Frank D.J., Ismail K.E., Lo S.H. Sai-halasz G.A., Viswanathan R.G., Wann H.J.C., Wind S.J., Wong H.S. *CMOS scaling into the nanometer regime*. Proceedings of IEEE. 1997. **85**(4): p. 486-504.

[5.6] Aygun G.., Yildiz I. *Interfacial and structural properties of sputtered* HfO_2 *layers*. Journal of Applied Physics. 2009. **106**(1): p.014312-1/7.

[5.7] Wu H., Zhao Y. White M.H. *Quantum mechanical modeling of MOSFET gate leakage for high-k gate dielectrics*. Solid State Electronics. 2006. **50**: p.1164-1169.

[5.8] Krasnikov Y.G., Zaitsev N.A., Matyushkin I.V. *On the issure of an equivalent oxide thickness evaluation in nanoscale MISFETs*. Russian Microelectronics. 2011. **40**(1): p.25-30.

[5.9] Wallace R.M., Wilk G.D. *Materials issues for high-* κ *gate dielectric selection and integration [electronic resource]*. Springer: Springer series in advanced microelectronics. 2005. Vol. 16, Part Ⅲ: p.253-286.

[5.10] Park B.Y., Zaouk R., Madou M.J. *Microfluidic techniques-Methods in molecular biology [electronic resource]*. Springer: 2006. Vol. 321, Part Ⅰ (Fabrication of microelectrodes using the lift-off technique): p.23-26.

[5.11] He G., Fang Q., Li G.H., Zhang J.P., Zhang L.D. *Structural and optical properties of nitrogen-incorporated HfO2 gate dielectrics deposited by reactive sputtering*. Applied Surface Science. 2007, **253**: p.8483–8488..

[5.12] Mitchell D.R.G., Aidla A., Aarik J. *Transmission electron microscopy studies of HfO2 thin films grown by chloride-based atomic layer deposition*. Applied Surface Science. 2006, **253**: p.606–617.

[5.13] Kumagai A., Zhang H., Ishibashi K. *Deposition of metal oxide thin films (HfO2 and RuO2) by oxygen radical-assisted MOCVD*. Vacuum. 2004, **74**: p.461–465.

[5.14] Synowicki R.A. *Spectroscopic ellipsometry characterization of indium tin oxide film microstructure and optical constants*. Thin Solid Films. 1998, **313-314**: p394-397.

[6.1] *The International Technology Roadmap for Semiconductors(ITRS), 2007 Edition.* http://www.itrs.net/reports.html.

[6.2] ISO/TS 17450-2. *Geometrical Product Specifications(GPS)-General concepts-Part 2: Operators and uncertainties.* 2005, International Organization for Standardization, Geneva, Swiss.

[6.3] ISO/TS14253-2:1999. *Geometrical product specification (GPS) - Inspection by measurement of workpieces and measuring equipment-Part 2: Guide to the estimation of uncertainty in GPS measurement, in calibration of measuring equipment and in product verification*. 1999, International Organization for Standardization, Geneva, Swiss.

[6.4] ISO, IEC, BIPM, OIML, IFCC, IUPAC, IUPAP. *Guide to the Expression of Uncertainty in Measurement (GUM)* . 1993, International Organization for Standardization, Geneva, Swiss.

[6.5] Giacomo P. *Metrologia*. 1981, **17**: p.73 -74.

[6.6] Giacomo P. *Metrologia*. 1987, **24**: p.49-50.

[6.7] ISO 3534-1:1993. *Statistics — Vocabulary and symbols — Part 1: Probability and general statistical terms.* 1993, International Organization for Standardization, Geneva, Swiss.

[6.8] Chunovkina A. G. *Measurement error, measurement uncertainty, and measurand uncertainty.* Measurement techniques. 2000, 43(**7**): p 581-586.

[6.9] ISO 13528:2005, *Statistical methods for use in proficiency testing by interlaboratory comparisons*. 2005, International Organization for Standardization, Geneva, Swiss.

[6.10] JCGM 100:2008, *GUM 1995 with minor corrections-Evaluation of measurement data — Guide to the expression of uncertainty in measurement.*

BIMP, 2008.

[6.11] Yamaguchi A. and Yamamoto J. *Influence of image processing on Line-Edge Roughness in CD-SEM measurement***.** Proc. of SPIE. 2008, **6922**, **692221:** p 692221-1~692221-8.

[6.12] Yamaguchi A., Tsuchiya R., Fukuda H., Komuro O., Kawada, H. and Iizumi T. *Characterization of Line-Edge Roughness in Resist Patterns and Estimation of its Effect on Device Performance.* Proc. of SPIE. 2003, **5038**: p 689-698.

[6.13] Yamaguchi A., Nakagaki R., Kawada H. *CD-SEM Technologies for 65-nm Process Node*. Hitachi Review. 2005, 54(**1**): p.15~21.

[6.14] Nelson C. M.，Susan C. Palmateer，Ted Lyszczarz. *Metrology Methods for the Quantification of Edge-Roughness*. Proc of SPIE. 1998, **3332**:19-29.

[6.15] Nelson C., Palmateer S. C., Forte A. R. and Lyszczarz T. M.. *Comparison of metrology methods for quantifying the line edge roughness of patterned features*. Journal Vacuum Science and Technology, B. 1999, 17(**6**): p 2488-2498.

[6.16] Kim H. W., Lee J.Y., Shin J., Woo S. G., Cho H. K. and Moon J. T. *Experimental investigation of the impact of LWR on sub-100-nm device performance.* IEEE Transactions electron devices. 2004, 51(**12**): p 1984-1988.

[6.17] Bunday B., Rijpers B., Banke B., Archie C., Peterson I. B., Ukraintsev V., Thomas H., Asano M. I*mpact of Sampling on Uncertainty: Semiconductor Dimensional Metrology Applications.* Proc. of SPIE. 2008 **6922**: p. 69220X-1-69220X-22.

[6.18] Frase C. G., Haßler-Grohne W., Dai G., Bosse H., Novikov Y. A. and Rakov A. V. *SEM linewidth measurements of anisotropically etched silicon structures smaller than 0.1 μm*. Measurement Science Technology. 2007, **18**: p.439–447.

[6.19] Abe H., Hamaguchi A. and Yamazaki Y., *Evaluation of CD-SEM Measurement Uncertainty using Secondary Electron Simulation with Charging Effect SEM*. Proc. of SPIE. 2007, **6518**: 65180L-1-65180L-10.

[6.20] Bunday B. D., Allgair J., Adan O., Tam A., Latinski S. and Eytan G. *Small feature accuracy challenge for CD-SEM metrology physical model solution*. Proc. of SPIE. 2006, **6152**: p.61520S-1-61520S-8.

[6.21] Schroder D. K., *Semiconductor material and device characterization*. Third edition. IEEE press. 2006: p.629-639.

[6.22] Yanez M.J. and Barbosa S.E., *Changes in particle area measurements due to SEM accelerating voltage and magnification.* Microscopy Research and Technique. 2003, 61(**5**)**:** p. 463–468.

[6.23] Banke B., Archie C., Sendelbach M., Robert J., Slinkman J., Kaszuba P.,

Kontra R., DeVries M. and Solecky E. *Reducing measurement uncertainty drives the use of multiple technologies for supporting metrology*. Proc. of SPIE. 2004, **5375**: p.133-150.

[6.24] Tortonese M., Guan Y., Prochazka J. *NIST-Traceable Calibration of CD-SEM Magnification Using a 100 nm Pitch Standard*. Proc. of SPIE. 2003, **5038:** p.711-718.

[6.25] Yeong-U. K. Ko Y.U., Eom T. B, Kim K. H. and Kim S W., *Linewidth measurement of wafers using SEM and its uncertainty evaluation*. Proc. of SPIE. 1996, **2725**: p.159-168.

[6.26] Villarrubia J. S. *Issues in Line Edge and Linewidth Roughness Metrology*. AIP Conference Proceedings. 2005, **788**: p.386-393.

[6.27] Winrow B. *A Study of Rough Amplitude Quantization by Means of Nyquist Sampling Theory*. IRE transactions on circuit theory. 1956: p 266-276.

[6.28] Villarrubia J. S. and Bunday B. D., *Unbiased Estimation of Linewidth Roughness*. Proc. of SPIE. 2005, **5752**: p 480-488.

[6.29] Bunday B. D., Bishop M. and Cormack D. M., *Determination of Optimal Parameters for CD-SEM Measurement of Line Edge Roughness*. Proc.of SPIE. 2004, **5375**: p 515-533.

[6.30] Yamaguchi A., Robert S., Kawada H., Iizumic T. and Sugimoto A. *From speculation to specification: A discussion on how to define the tolerance of LER/LWR and its measurement methodology.* Proc. of SPIE. 2006, **6152**: p 6152401-08.

[6.31] Thomas T R. *Rough surface. New York*. Longman Press. 1982: p105-109.

[7.1] Strasser P., Robin F., Carlstrom C.F., Wuest R., Kappeler R. and Jackel H. *Sidewall roughness measurement inside photonic crystal holes by atomic force microscopy*. Nanotechnology, 2007,**18**: p. 405703.

[7.2] Sun J., Kondo K., Toshihiro Y., et al. *High-aspect-ratio copper via filling used for three-dimensional chip stacking*. Journal of The Electrochemical Society, 2003, **150**: p.G355-G359.

[7.3] Pania S.K., Wonga C.C., Sudharsanamb K., Limb V. *Direct measurement of sidewall roughness of polymeric optical waveguides*. Applied Surface Science, 2005, **239**: p.445–450.

[7.4] Dixson, R. G.; Orji, N. G.; Fu, J.; Tsai, V.; Williams, E. D.; Kacker, R.; Vorburger, T. V.; Edwards, H. L.; Cook, D.; West, P. E.; Nyffenegger, R. *Silicon single atom steps as AFM height standards*. Proceedings of SPIE, Metrology, Inspection, and Process Control for Microlithography XV, 2001, **4344**: p.157-168.

[7.5] Hoffmann K.P., Ahbe T., Herrmann K., Hasche K., Pohlenz F., Sun J. *Development and calibration of standards for the coating thickness in the range of micrometer and nanometer*. Surface and Coatings Technology, 2003, **169 –170**: p.732–734.

[7.6] Fischer K., Aleman B.J., Tao S.L., et al. *Biomimetic Nanowire Coatings for Next Generation Adhesive Drug Delivery Systems*. Nano Letters, 2009, 9(**2**): p.716-720.